

Copyright
by
Chi-Jui Chung
2018

**The Dissertation Committee for Chi-Jui Chung Certifies that this is the approved
version of the following dissertation:**

**Integrated Photonic Devices for Electromagnetic Wave Sensing, Optical
True Time Delay, and Trace Gas Sensing**

Committee:

Ray T. Chen, Supervisor

Mikhail Belkin

Donglei Fan

Paul S. Ho

Hu Tao

**Integrated Photonic Devices for Electromagnetic Wave Sensing, Optical
True Time Delay, and Trace Gas Sensing**

by

Chi-Jui Chung

Dissertation

Presented to the Faculty of the Graduate School of

The University of Texas at Austin

in Partial Fulfillment

of the Requirements

for the Degree of

Doctor of Philosophy

The University of Texas at Austin

August 2018

Dedication

This dissertation is dedicated to my family.

Acknowledgements

I would like to express my sincere gratitude to many people who gave me support and encouragement during the last four years of my Ph.D. journey. Firstly, I would like to thank my advisor, Dr. Ray T. Chen, for his invaluable patience, guidance, and support. Many thanks also go to Dr. Mikhail Belkin, Dr. Donglei Fan, Dr. Paul S. Ho, and Dr. Hu Tao for their time and feedback on the dissertation.

I am grateful to Dr. Xiaochuan Xu for providing continuous support during the entire doctoral program and insightful advice toward the research projects. I would also like to thank my colleagues in Omega Optics Inc. and Optical Interconnect Group: Dr. Swapnajit Chakravarty, Dr. Harish Subbaraman, Dr. Hamed Dalir; Yi Zou, Xingyu Zhang, Chun-Ju Yang, Zeyu Pan, Hai Yan, Zheng Wang, Rui Wang, Farzad Mokhtari-Koushyar, Ali Rostamian, Zoufeng Ying, Elham Heidari, Kyoungmin Yoo, and other group members for their assistance and advice. I also appreciate the help from other graduate students and staff at the Microelectronics Research Center.

The work in this dissertation is a collaborative effort. I would like to acknowledge Dr. Jingdong Luo from the University of Washington and Dr. Qiwen Zhan from the University of Dayton for their direct support.

Finally, my profound gratitude goes to my family for everlasting love and encouragement. I especially thank my wife Yu-Wei and my daughter Ke-Ching from the very bottom of my heart. This dissertation could not have been accomplished without their companion and trust.

Abstract

Integrated Photonic Devices for Electromagnetic Wave Sensing, Optical True Time Delay, and Trace Gas Sensing

Chi-Jui Chung, Ph.D.

The University of Texas at Austin, 2018

Supervisor: Ray T. Chen

Investigations on how informative signals interact with optical light wave propagating in integrated photonic devices have been emerging research topics for various sensing and high-speed communication applications. These have become attractive research fields since integrated photonic devices offer unparalleled advantages such as high sensitivity, high-density integration, low power consumption, and great electromagnetic interference immunity. Among all available material platforms for integrated photonic devices, silicon is one of the ideal materials since silicon has excellent optical waveguides properties such as high transparency and high refractive index in optical communication wavelengths. These properties enable low loss and compact on-chip silicon photonic devices. Also, silicon photonic devices benefit from mature silicon-based semiconductor nanofabrication facilities; therefore, they can be fabricated with low cost. On the other hand, silicon photonic devices built on typical silicon dioxide-based silicon-on-insulator wafers can't be operated beyond the wavelength of 3.5 μm due to high intrinsic mid-infrared absorption of silicon dioxide. Indium phosphide becomes an alternative candidate due to low optical loss. In addition,

indium phosphide-based quantum cascade lasers provide narrowband tunable continuous-wave room-temperature emission in the entire mid-infrared spectral range from 3-11 μm which makes monolithically integrated devices possible. Wide varieties of photonics devices on both silicon and indium phosphide platforms have been demonstrated so far such as high-speed modulators, low loss waveguides, couplers, optical phased arrays, and sensors. In this dissertation, silicon integrated photonic devices for electromagnetic wave sensing and optical true time delay lines, as well as indium phosphide-based integrated photonic devices for trace gas sensing, are presented. This dissertation shows that integrated photonic devices are promising for high-performance sensing and novel communication applications.

Table of Contents

Table of Contents	viii
List of Tables	xi
List of Figures	xii
Chapter 1: Introduction	1
1.1 Silicon-Based Integrated Microwave Photonic Devices	1
1.2 Indium Phosphide (InP) Integrated Photonic Devices for Trace Gas Sensing	2
1.3 Dissertation Organization	3
Chapter 2: Silicon-Based Hybrid Integrated Photonic Chip for Ku band Electromagnetic Wave Sensing	5
2.1 Introduction.....	5
2.2 Device Design.....	10
2.2.1 EO polymer infiltrated 1D SPCW phase shifter.....	10
2.2.2 Bowtie antenna and ion implantation design for 14.1GHz operation..	12
2.2.3 Inverse taper coupler design	14
2.3 1D SPCW-Based EM Wave Sensor Device Fabrication.....	18
2.4 Device Characterization.....	21
2.4.1 Transmission spectra measurement and group index calculation.....	21
2.4.2 Antenna frequency response measurement.....	24
2.4.3 EM wave sensing measurements	25
2.5 Conclusion	29

Chapter 3: On-Chip Photonic Electromagnetic Wave Sensor Featuring Silicon-Polymer Hybrid Subwavelength Grating Waveguide and Bowtie Antenna.....	31
3.1 Introduction.....	31
3.2 Device Design.....	35
3.2.1 EO polymer infiltrated SWG waveguide.....	35
3.2.2 Thin bowtie antenna design with high field enhancement	36
3.3 SWG Waveguide-Based EM Wave Sensor Device Fabrication	37
3.4 Device Characterization.....	39
3.5 Conclusion	43
Chapter 4: Fishbone-Structured One-Dimensional Photonic Crystal Waveguide Integrated Photonic Chip for Ultra-Compact Optical True-Time Delays	44
4.1 Introduction.....	44
4.2 FS 1D PCW Device Design.....	46
4.3 Device Fabrication and Characterization.....	49
4.3.1 FS 1D PCW fabrication and characterization.....	49
4.3.2 Delay lines propagation loss and delay measurement	52
4.4 Conclusion	56
Chapter 5: Indium Phosphide-Based Polarization Rotator-Splitter and Fully Suspended Holey Photonic Crystal Waveguide for Mid-Infrared Photonic Trace Gas Sensing.....	57
5.1 Introduction.....	57
5.2 Optical Losses in InGaAs-InP Waveguides.....	59
5.3 Single-Step Etched InGaAs-InP PRS Design	61
5.4 InGaAs-InP PRS Fabrication and Characterization.....	64
5.5 Fully Suspended Holey PCW in InGaAs-InP System for Ammonia Gas Sensing.....	66

5.6 Conclusion	71
Chapter 6: Conclusions and Recommendations for Future Work	73
6.1 Conclusions.....	73
6.2 Recommendations for Future Work	75
Appendix.....	80
Bibliography	87
Vita.....	100

List of Tables

Table 2.1: The end-fire coupling measurement results of the fabricated waveguides.....	18
Table 6.1: The RF properties of the packaging housing materials.	77

List of Figures

Figure 1.1: Optical properties of different semiconductor materials for mid-IR photonics silicon-on-insulator (SOI), silicon-on-sapphire (SOS), Ge-on-Si, GaAs, InP. (a) Optical power loss in SiO₂, sapphire, and high-resistance silicon versus mid-IR wavelength. Optical losses in silicon are multiplied 10× for clarity. (b) Refractive index and optical loss in Ge, GaAs, and Si in mid-IR.....3

Figure 2.1: (a) Schematic of the proposed sensor based on bowtie antenna coupled MZI structure. Light coupled from inverse taper coupler is split into two arms: one is EO polymer infiltrated 1D SPCW, and the other is strip waveguide with teeth. The phase is modulated at the arm of 1D SPCW arm and subsequently causes the output optical intensity variation when the light of the two arms interfere. (b) Schematic plot of the slow light enhanced EO polymer infiltrated 1D SPCW, which consists of a slot and two sections of teeth connected to bulk silicon.9

Figure 2.2: (a) Photonic band diagram and (b) group index versus wavelength of 1D SPCW using plane wave expansion method, inset is the optical modal profile.11

Figure 2.3: (a) Schematic of the step taper section connecting silicon strip waveguide to regular slot waveguide (b) Simulated transmission spectra with (show in red) and without the step taper (show in black).12

Figure 2.4: (a) Side view and (b) top view of the bowtie antenna with extension bars and ion implantation distribution (c) side view and (d) top view of simulated electric field distribution over the antenna gap region feeding with 14.1 GHz.14

Figure 2.5: Schematic drawing and the designed parameters of the inverse taper coupler.....	15
Figure 2.6: Optimized photolithography results of the SU-8 pattern.	16
Figure 2.7: Alignment results of the SU-8 layer and the silicon layer.	17
Figure 2.8: The measurement setup schematic for the inverse taper couplers.	17
Figure 2.9: Complete fabrication process: (a)1 st implanted bare sample with Pt alignment marks, (b)2 nd implantation and anneal, (c)waveguide patterning and etching, (d)antenna region etching, (e)gold seed layer deposition, electroplating, and seed layer removal, (f)SU-8 inverse taper overlaid patterning, (g) EO polymer coating and curing.	20
Figure 2.10: SEM images of fabricated device: (a)top view of MZI structure with antenna (colored with orange), (b)tilted cross-section view of the MZI with antenna (colored with orange), (c)top view of 1D SPCW region with 5 sets of step taper, (d) tilted cross-section view of 1D SPCW.	21
Figure 2.11: Measured transmission spectrum of 300 μm long EO polymer infiltrated 1D SPCW.....	22
Figure 2.12: Measured transmission spectrum of EO polymer infiltrated MZI structure and the calculated group indices of the 1D SPCW as a function of wavelength.....	24
Figure 2.13: Measured and simulated S11 parameter from in K_u band.....	25
Figure 2.14: (a) Schematic of EM wave sensing testing setup. Green path: optical signal; Red path: electrical signal. (b) Horn antenna as transmitting antenna at far field distance with respect to the device. (c) the zoom-in image of the device and two coupling lensed fiber.....	26

Figure 2.15: MSA reading at 14.1GHz from high-speed PD when the input signal of the horn antenna is 6.7dBm.	27
Figure 2.16. Measured sensing signal reading from MSA versus different microwave input signal power.....	29
Figure 3.1: Schematic of the proposed EM wave sensor based on a bowtie antenna coupled MZI structure. MZI structure is composed of an EO polymer infiltrated SWG waveguide and a silicon strip waveguide. The wireless microwave signal is collected and concentrated in the antenna gap for EO modulation on the SWG arm. Grating couplers are adapted for efficient light coupling.....	35
Figure 3.2: Schematic of the EO polymer infiltrated SWG waveguide. It consists of spatially periodical silicon pillars with a subwavelength period.	36
Figure 3.3: Schematic of the thin gold bowtie antenna with extension bars standing on the buried oxide layer of the SOI wafer.....	37
Figure 3.4: Fabrication steps of the SWG waveguide-based sensor device: (a) optical waveguides and grating couplers patterning and etching, (b) antenna region etching, (c) gold thin bowtie antenna patterning.	38
Figure 3.5: SEM images of fabricated device: (a) grating couplers, (b) bowtie antenna and MZI structure in the antenna gap. One arm is a silicon SWG waveguide and another is a silicon strip waveguide. (c) SWG waveguide and taper region connecting to strip waveguide, (d) SWG waveguide.....	39
Figure 3.6: Measured transmission spectrum of the SWG waveguide-based EM wave sensor device.....	40

Figure 3.7: (a) Optical sideband testing setups for microwave detection, (b)(c) Measured optical response of the device with sidebands at modulating frequencies from 15-20 GHz.	41
Figure 3.8: (a) Limit of detection testing setups for EM wave sensing, (b) Measured limit of detection of the SWG sensor device at 14-17 GHz.	43
Figure 4.1: (a) Schematic of the proposed FS 1D PCW structure. (b) Band diagram of the FS 1D PCW. (c-h) Ez distributions of the modes in band 0-3. (i) Group indices of the bands.	47
Figure 4.2: (a) Group index and dispersion of band 2 when $a=400$ nm, $W_b=188$ nm, $L_a=1000$ nm, and $W_a=400$ nm. Black: Group index. Red: Dispersion. (b) Simulated transmission curve Black: Without step taper. Red: With step taper.	48
Figure 4.3: (a) SEM image of FS 1D PCW with step taper (b) Subwavelength grating coupler.	50
Figure 4.4: (a) Transmission spectrum testing 500 μm long FS 1D PCW. (b) Measured MZI transmission spectrum and derived group index of a 500 μm long FS 1D PCW.	52
Figure 4.5: (a) Optical microscope images of the four-channel device (b) FS 1D PCW loss spectrum derived from the cut-back method from waveguides with different FS 1D PCW length. Inset is the measured transmission versus propagation length plot.	53

Figure 4.6: (a) Wavelength continuously tunable time delay measurement setup for FS 1D PCW TTD lines. TLS: Tunable laser source; GC: Grating couplers, and Phase-frequency curves for (b) Channel-2 (1 mm FS 1D PCW with 2 mm silicon strip waveguide) (c) Channel-3 (2 mm FS 1D PCW with 1 mm silicon strip waveguide) (d) Channel-4 (3 mm FS 1D PCW). From top to bottom, each color line represents the measurements at $\lambda=1567$ nm (black), 1570 nm (red), 1573 nm (green), 1576 nm (blue), and 1579 nm (magenta) respectively.	55
Figure 5.1: (a) The layout of the propagation loss testing waveguides with bending radii of R, (b) tilted SEM image of fabricated InGaAs-InP waveguide.	60
Figure 5.2: Loss versus propagation length difference plot for (a) TM polarized input, and (b) TE polarized input. Loss data exclude waveguides with sharp bends and the linear fitting (shown in red) for TM polarized input, and (b) TE polarized input.	61
Figure 5.3: (a) Schematic diagram of the single-step etched PRS working at $6.15 \mu\text{m}$ in InGaAs-InP platform, (b) cross-section schematic and the epitaxy layer structures of the PRS, (c) the effective index versus InGaAs-InP waveguide width plot, (d)(e) modal distribution of converted TE_{10} , and (f)(g) modal distribution of unconverted TM_{00}	63
Figure 5.4: (a) Schematic plot for testing setup, (b) real testing setup, and (c)(d) the images indicates the relative position between fiber and the testing photonic chip from side view and top view cameras respectively.	65
Figure 5.5: (a) Optical microscope images of the fabricated PRS, and (b) Transmission of the two output arms for four devices with identical parameters.	66

Figure 5.6: (a) Schematic diagram of InGaAs fully suspended holey PCW, (b) simulated photonic band diagram of InGaAs fully suspended holey PCW by 3D PWE. Different devices are made with various lattice constants “a” to probe the guided mode (shown in red) using a single wavelength external source at $\lambda=6.15 \mu\text{m}$ for optical characterization, and (c) measured optical transmission versus different lattice constant.....68

Figure 5.7: Schematic of fabrication steps of InGaAs holey PCW including ICP RIE (a) oxide etching mask growth, (b) transfer of e-beam lithography pattern to oxide mask by RIE, (c) to InGaAs/InP layers, and (d) HCl: DI water= (3:1) dip for a free-standing membrane structure.69

Figure 5.8: (a) Top view and (b) cross-section SEM images of holey PCW in after InGaAs-InP dry etching. Features are etched $\sim 3.1 \mu\text{m}$ deep. Broadening of holes upon reaching InP is not of concern since the InP is wet etched away during undercut sacrificial removal, (c) cross-section SEM image after sacrificial undercut wet etch showing suspended membrane SPCW in InGaAs with $\sim 26 \mu\text{m}$ deep undercut, (d) magnified cross-section showing no sagging or bending even after cleaving.....70

Figure 5.9: (a) Schematic diagram of the ammonia sensing setup, (b) transmitted optical intensity of a 1 mm long holey PCW with $a=1600\text{nm}$ in the presence and absence of 5ppm ammonia.....71

Figure 6.1: Prototype of package EM wave sensor. After best coupling condition achieved on a testing stage, the optical fibers are glued. The relative position between fibers and chip is then fixed.....77

Figure 6.2: (a) the exploded view of the complete package. (b) The machined
MACOR base and Teflon lid with real EM wave sensor chip; The
polished angled fiber is in the glass slide trench.....78

Figure 6.3: Schematic of coupling light with grating couplers and polished angled
fiber.....78

Chapter 1: Introduction

1.1 SILICON-BASED INTEGRATED MICROWAVE PHOTONIC DEVICES

Processing and transmission of microwave signals by photonic systems have long attracted great research interests since their conventional electrical counterparts are facing problems such as RC delay, high transmission loss, strong electromagnetic interference (EMI), and high power consumption [1]. Microwave photonic devices offer significant advantages for both the communications community and the sensing industry in terms of data rate, dynamic range, immunity to EMI, and requirements of cost, size, weight, and power consumption (C-SWaP). Several crucial applications of microwave photonics include true-time delay lines [2], antenna radio frequency (RF) beamforming [3], RF filter [4], electro-optics (EO) modulator [5], as well as electromagnetic field sensing [6].

Among the available photonic integration platforms, silicon photonics is particularly attractive because of advantages such as low-cost manufacturing and on-chip integration with electronics. These advantages result from the compatibility of silicon photonic devices and the complementary metal-oxide-semiconductor (CMOS) fabrication techniques which are widely used in the semiconductor industry. Silicon also provides high transparency and high refractive index in optical communication wavelengths [7], which enables low loss and compact size of on-chip optical devices. Furthermore, slow enhanced photonic crystal devices can be built on a silicon wafer where the group velocity of light slows down and enhances the light-matter interactions significantly [8]. Widespread research has resulted in plenty interesting silicon-based photonic devices, including high-speed modulators [9], low loss waveguides [10], photodetectors [11], optical phased arrays [12], sensors [13], etc. In Chapter 2 to Chapter 4 of this dissertation, novel silicon-based photonic devices are demonstrated for electromagnetic (EM) wave

sensing and optical true-time delay applications. These devices are designed to address high loss and low light-matter interactions in the existing devices.

1.2 INDIUM PHOSPHIDE (INP) INTEGRATED PHOTONIC DEVICES FOR TRACE GAS SENSING

Mid-infrared (Mid-IR) trace-gas sensing is a rapidly developing field and can be applied in wide range of applications such as detection of explosives and hazardous chemicals, breath analysis for medical diagnostics, and control of industrial processes and emissions. Currently, most mid-IR trace gas sensing systems are developed based on bulky gas cells and discrete optical components on cavity ring-down spectroscopy (CRDS) [14], tunable diode laser absorption spectroscopy (TDLAS) [15], Fourier transform infrared spectroscopy (FTIR) [16], or photo-acoustic spectroscopy (PAS) methods [17].

Mid-infrared (Mid-IR) absorption spectroscopy based on integrated photonic devices have shown great promise on trace-gas sensing [18]. It eliminates the needs of bulky gas cells and free-space optical components; therefore, has substantial advantages such as lightweight, alignment-free, and high sensitivity sensing over conventional off-chip methods [15, 19]. In addition, slow light enhanced photonic crystal waveguides built on integrated photonic circuits can slow down the speed of light and increase effective light-analyte interaction length. Therefore, the higher detection sensitivity for the targeted gas analyte can be realized.

A need exists to cover wide monitor range of mid-IR wavelengths from 3-14 μm for detecting various analytes such as chemical warfare simulants, greenhouse gases, and exhaust emissions. Among all waveguide configurations with core materials such as silicon (Si), germanium (Ge), gallium arsenide (GaAs), and InP, only GaAs-aluminum

gallium arsenide (AlGaAs) waveguides and Indium gallium arsenide (InGaAs)-InP waveguides offer a well-established lattice-matched, very low defect density platform for low loss optical circuits in the 3-15 μm wavelength range as shown in Figure 1.1 [20]. In addition, the InGaAs-InP platform allows monolithic epitaxial growth of high-quality quantum cascade lasers (QCLs) and quantum cascade detectors (QCDs) and eliminates expensive and low yield wafer/chip bonding processes in any other system, including GaAs-AlGaAs. Therefore, the choice of InP enables the possibility of a monolithically integrated trace gas sensing system which is robust to vibrations and physical stress. In Chapter 5, low loss InP-based photonic devices are investigated for trace gas sensing applications.

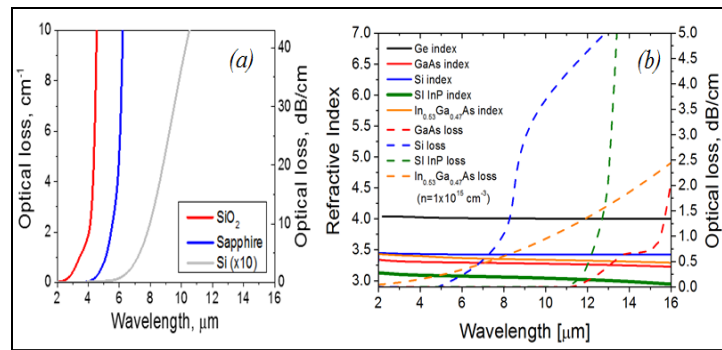


Figure 1.1: Optical properties of different semiconductor materials for mid-IR photonics silicon-on-insulator (SOI), silicon-on-sapphire (SOS), Ge-on-Si, GaAs, InP. (a) Optical power loss in SiO_2 , sapphire, and high-resistance silicon versus mid-IR wavelength. Optical losses in silicon are multiplied $10\times$ for clarity, (b) Refractive index and optical loss in Ge, GaAs, and Si in mid-IR.

1.3 DISSERTATION ORGANIZATION

This dissertation is organized as follows:

Chapter 2-3 cover two types of on-chip silicon photonic EM wave sensor for highly sensitive EM wave detection at K_u band (12-18GHz). In Chapter 2, an EM wave sensor with slow light enhanced one-dimensional (1D) photonic crystal waveguide

(PCW) infiltrated by EO polymer is described. In Chapter 3, an EM wave sensor with sub-wavelength grating structure infiltrated by EO polymer is described. These two sensors are based on EO modulation and therefore has several important advantages over conventional electrical RF sensors including high sensitivity, compact size, and strong immunity to electromagnetic interference (EMI).

In Chapter 4, a four-channel optical true-time delay module features slow light enhanced 1D photonic crystal waveguide is proposed and experimentally demonstrated. A large time delay can be achieved in a compact footprint with squint-free property in wide RF frequency range. The proposed optical true-time delay module can be used in a wide range of RF systems to widen the RF bandwidth.

In Chapter 5, the waveguide losses are characterized, and a polarization rotator-splitter is discussed in low index contrast InGaAs-InP material system. In addition, a fully suspended holey PCW for ammonia sensing is demonstrated. These devices show potential for monolithic integration of quantum cascade lasers and detectors with holey PCW trace gas sensors in the molecular fingerprint window at mid-IR wavelength range.

Finally, a summary of the research efforts and proposed future directions will be discussed in Chapter 6.

Chapter 2: Silicon-Based Hybrid Integrated Photonic Chip for Ku band Electromagnetic Wave Sensing

In this chapter, we experimentally demonstrate a highly sensitive on-chip photonic electromagnetic wave sensor operating at 14.1 GHz with a 3 dB bandwidth of 4.84 GHz. The demonstrated electromagnetic sensor has several important advantages over conventional electrical electromagnetic sensors including high sensitivity, compact in size and strong immunity to electromagnetic interference (EMI). The sensor is comprised of a bowtie antenna and an asymmetric Mach-Zehnder interferometer (MZI). One arm of the MZI is an electro-optic (EO) polymer infiltrated one-dimensional (1D) slotted photonic crystal waveguide (SPCW), and the other arm is a strip waveguide with teeth of a subwavelength pitch. Bowtie antennas are designed and optimized to effectively collect 14.1 GHz microwave signal and applies it across the SPCW. The phase of the light guided in the SPCW therefore changes, and so does the amplitude of the output end of the MZI. The sensor is only $4.6 \text{ mm} \times 4.8 \text{ mm}$ in size and has a low insertion loss of $\sim 10 \text{ dB}$. Experimental results show the limit of detection at 14.1 GHz is 4.31 mW/m^2 , which is corresponding to a minimum detectable electric field of 1.8 V/m .¹

2.1 INTRODUCTION

On-chip photonic electromagnetic (EM) wave sensors have been attracting considerable attention in recent years [6, 21-23]. This photonic sensing approach detects microwave signals via photons and thus eliminates the need of discrete electronics components for high-speed signal transmission, amplification, and power conditioning,

¹ Portions of this chapter have been published in C.-J. Chung, X. Xu, Z. Pan, F. Mokhtari-Koushyar, R. Wang, H. Yan, H. Subbaraman, and Ray T. Chen, "Silicon-Based Hybrid Integrated Photonic Chip for Ku band Electromagnetic Wave Sensing," *Journal of Lightwave Technology*, vol. 36, pp. 1568-1575, 2018.

C.-J. Chung designed and fabricated the device, performed the experiments, analyzed the data, and wrote the manuscript.

which are commonly used in conventional electrical microwave sensors [24, 25]. Therefore, photonic EM wave sensors have eminent advantages over the traditional electrical counterparts in terms of immunity to electromagnetic interference (EMI), high-speed operation, power consumption, and footprint [23, 26]. These advantages make high sensitivity and accurate on-chip EM sensors a promising approach for high-performance wireless communication [21, 27, 28] and sensing applications [6, 22, 29].

One crucial element in a high performance on-chip photonic EM wave sensor is an efficient electro-optic (EO) phase shifter, in which the enhanced electrical field provided by antennas modulates the refractive index of the active material with EO effect and subsequently changes the phase of light guided in the phase shifter. Silicon is an ideal photonic device platform as mentioned in Chapter 1. However, bulk silicon is a material where second-order nonlinearity doesn't exist because of the centrosymmetry of its crystalline structure. Therefore, light can't be efficiently and linearly modulated using only bulk silicon. Electro-optic (EO) polymers consisting of a polymeric matrix doped with organic nonlinear chromophores have enabled large EO coefficient, wide radio frequency (RF) bandwidth, and low loss active photonic devices. In addition, EO polymer can be spin-coated on silicon passive device making high-performance EO modulation possible on silicon/EO polymer hybrid devices.

Various phase shifter designs have been proposed such as plasmonic/EO polymer hybrid structure [23], EO polymer waveguides [6, 21], lithium niobate waveguides [27], and silicon/EO polymer hybrid structure [30, 31]. Among these structures, the plasmonic/EO polymer hybrid structure shows the smallest footprint and is intrinsically capable of operating at high frequency due to the small resistance. However, the high propagation loss (>1 dB/ μm) of plasmonic waveguide [32] and the high insertion loss of the mode converter limit the performance due to the trade-off between interaction length

and optical loss. Moreover, the stringent fabrication alignment (<50 nm) between metal and waveguide makes it difficult to implement. The pure EO polymer and lithium niobate waveguides are not compatible with standard complementary metal-oxide-semiconductor (CMOS) fabrication process. In addition, both materials have lower refractive indices compared to silicon, resulting in a large footprint. EO polymer infiltrated silicon slot waveguides, which combine the advantages of the high refractive index of silicon and large EO effect in EO polymer, have also been studied intensively [33, 34]. When equipped with slow light structures, the effective in-device r_{33} in slow light slot waveguide can be greatly enhanced, making it a promising candidate for high-performance EM wave sensors.

Slow light two-dimensional (2D) photonic crystal silicon/polymer hybrid phase shift structure has high optical propagation loss [35] and is frail to fabrication errors [36]. One-dimensional (1D) slot photonic crystal waveguide (SPCW) has been reported with lower optical propagation loss when compared with 2D SPCWs, due to less etched surface area overlapped with optical mode while maintaining similar slow light effect [37]. Among EO polymer infiltrated 1D SPCW, 2D SPCW, and conventional slotted waveguide, 1D SPCW has the best figure-of-merit $f = \sigma \cdot n_g \cdot L_{3dB}$ [38] where σ is the ratio of optical mode in the EO polymer region, n_g is the group index, and L_{3dB} is the length of the phase shifter in millimeters with 3 dB propagation loss. Therefore, EO polymer infiltrated 1D SPCW has the potential to perform better than 2D SPCW and slotted waveguide as an EO phase shifter.

In this chapter, we design and demonstrate a compact and highly sensitive on-chip photonic EM waver sensor operating at 14.1 GHz with a 3 dB bandwidth of 4.84 GHz. 14.1 GHz falls into K_u band and can be applied to satellite communications for both civilian and military networks [39]. The proposed sensor features a set of bowtie antenna

and a Mach-Zehnder interferometer (MZI) structure with one arm of slow-light enhanced EO polymer infiltrated 1D SPCW and the other arm of silicon strip waveguide with teeth of a subwavelength pitch, as shown in Figure 2.1(a). The device region is doped with two-step ion implantation. The doping profile is tailored so that the resistance at the implanted region is greatly reduced and Ohmic contact is formed. Therefore, the signal voltage drop is mostly across the slot while the absorption loss is still low. A bowtie antenna is designed to harvest and concentrate electrical field of the EM wave and applies it onto the slow light enhanced EO polymer infiltrated SPCW to modulate the phase of the guided optical wave. Inverse taper couplers [40] with polymer overlay layer are adapted to efficiently couple light in and out from the sensor. The proposed sensor structure takes advantages of low loss and strong slow light effect of the 1D SPCW, high electric field enhancement of the bowtie antenna, and large EO coefficient of the EO polymer, which enable the detection of an EM wave with an electric field intensity of 1.8 V/m. Compared to 2.5 V/m minimum detectable electric field at 8.4 GHz reported in EO polymer infiltrated 2D SPCW paper [22], this work shows improvement due to the lower propagation loss of 1D SPCW structure while maintaining the similar slow light effect. The device is only $4.6 \text{ mm} \times 4.8 \text{ mm}$ in size with the active region of $300 \text{ }\mu\text{m}$ offering a compact solution for a vast range of EM wave applications.

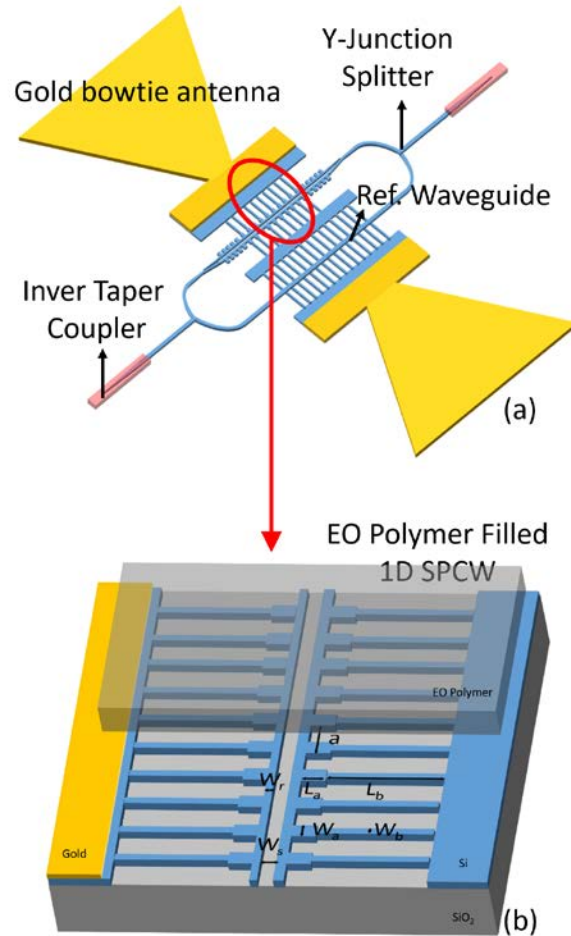


Figure 2.1: (a) Schematic of the proposed sensor based on bowtie antenna coupled MZI structure. Light coupled from inverse taper coupler is split into two arms: one is EO polymer infiltrated 1D SPCW, and the other is strip waveguide with teeth. The phase is modulated at the arm of 1D SPCW arm and subsequently causes the output optical intensity variation when the light of the two arms interfere, (b) Schematic plot of the slow light enhanced EO polymer infiltrated 1D SPCW, which consists of a slot and two sections of teeth connected to bulk silicon.

2.2 DEVICE DESIGN

2.2.1 EO polymer infiltrated 1D SPCW phase shifter

The active arm of the MZI is the slow light enhanced EO polymer infiltrated SPCW where light slows down and is modulated by interacting with EO polymer based on the enhanced Pockels effect. The 1D SPCW is comprised of center EO polymer slot, and two sections of the silicon teeth as shown in Figure 2.1(b). Compared to previously reported design [38], a set of narrow teeth is used to connect the 1D SPCW to the bulk silicon region so that the voltage drop of the modulation signal mostly occurs in the slot region. The narrow teeth have a subwavelength width and thus do not affect the propagation of the optical modes. The 1D SPCW is designed and optimized for 220 nm silicon-on-insulator (SOI) wafer with 3 μm buried oxide layer. An EO polymer, SEO125 ($n=1.63$), from Soluxra, LLC, which shows large bulk EO coefficient r_{33} of 135 pm/V, low optical loss, and good temporal stability is chosen to refill the silicon slot PCW as the top cladding layer [30]. This 1D SPCW is optimized using plane wave expansion (PWE) targeting at large group index, optical confinement in the slot, and slow light wavelength in the vicinity of 1550 nm. The optimized period (a), tooth width a (W_a), tooth width b (W_b), tooth length a (L_a), tooth length b (L_b), slot width (W_s), and rail width (W_r) are 370 nm, 148 nm, 74 nm, 250 nm, 1750 nm, 100, and 150 nm, respectively. The 1D SPCW length is 300 μm . The photonic band diagram and the group index simulation results are shown in Figure 2.2, which indicates that the group index can achieve 38.05 at 1564.8 nm and the optical confinement in the EO polymer slot σ is 0.24.

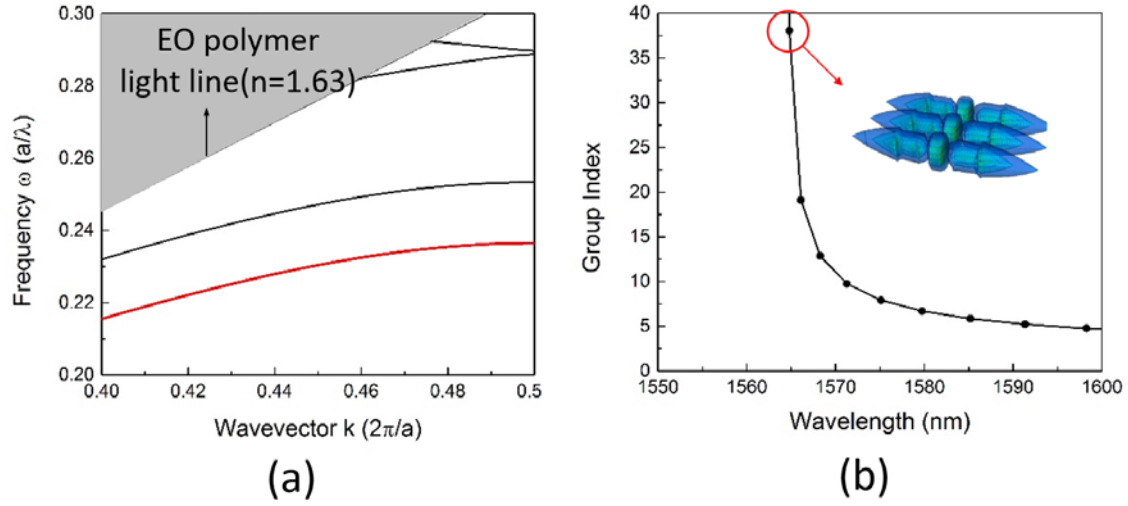


Figure 2.2: (a) Photonic band diagram and (b) group index versus wavelength of 1D SPCW using plane wave expansion method, inset is the optical modal profile.

To reduce the strong reflection at high group index interface of the 1D SPCW, we design a step taper between the 1D SPCW and regular slot waveguide using 3D FDTD simulation. The coupling efficiency increases from 37% to 62% at 1554 nm as shown in Figure 2.3. The step taper has five periods with pitch $a=350$ nm, tooth width (W_t)=140 nm, tooth length (L_t)=250 nm, and rail width (W_r)=200 nm.

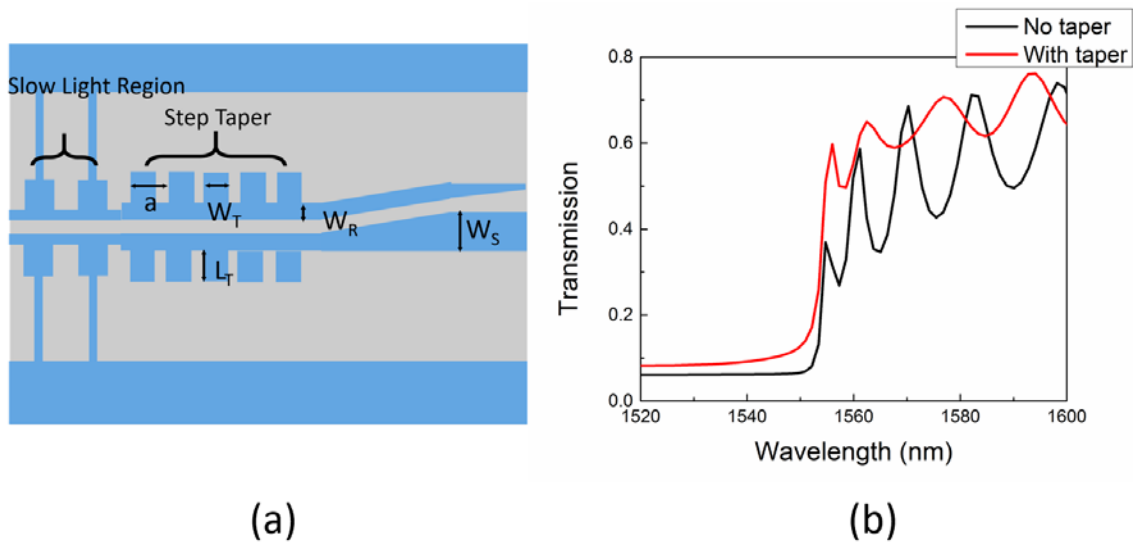


Figure 2.3: (a) Schematic of the step taper section connecting silicon strip waveguide to regular slot waveguide, (b) simulated transmission spectra with (show in red) and without the step taper (show in black).

The other arm of the MZI is a strip waveguide with teeth also designed for electrical connection purpose. The structure is optimized using plane wave expansion and three-dimensional (3D) finite difference time domain (FDTD) method. The optimized period, center silicon strip width, tooth width, and tooth length are 400 nm, 79.2 nm, and 1175 nm, respectively. The waveguide length is also chosen to be 300 μm . The simulated group index is 3.79 at 1550 nm.

2.2.2 Bowtie antenna and ion implantation design for 14.1GHz operation

A gold bowtie antenna with a pair of extension bars attached to the bowtie vertexes is designed to make full use of the entire length of the EO interaction range [41, 42]. This antenna provides uniform electrical field enhancement in the feed gap along the extension bar direction and therefore is suitable for integrating the MZI structure in the gap. To assure most of the enhanced RF electrical field falls across the EO polymer

infiltrated slot, two steps ion implantation are adopted to reduce RC time delay induced by bulk silicon and silicon teeth.

The schematic of the designed bowtie antenna and the implantation distribution is shown in Figure 2.4(a) and (b). The antenna stands on the buried oxide layer and has a thickness of $4\mu\text{m}$, the arm length of 2.3 mm , flare angle of 60 degree and extension bars of $8.4\mu\text{m} \times 300\mu\text{m}$. The gap between the extension bars is $8.4\mu\text{m}$. This antenna is designed to operate at 14.1 GHz . The center $7.35\mu\text{m}$ of the MZI structure is designed to be implanted to $1 \times 10^{17}\text{ cm}^{-3}$ so that the increased optical loss induced by free carrier absorption isn't significant, as shown in Figure 2.4(b) [43]. While the two bulk silicon regions adjacent to the center region are designed to be implanted to $1 \times 10^{20}\text{ cm}^{-3}$ to provide low enough resistance and ensure the Ohmic contact between the gold antenna and implanted silicon. Figure 2.4(c) and (d) show the electric field distribution simulation results between the antenna bars at 14.1 GHz with consideration of effective radio frequency(RF) dielectric constant and effective resistivity of silicon and EO polymer are calculated based on filling factor [44, 45]. The enhanced 14.1 GHz alternative voltage (AC) electric field is accumulated at the EO polymer slot region of the 1D SPCW and has 47.72% voltage drop in the EO polymer slot region calculated by integrating the electric field in the slot divided by the voltage applied on the antenna. The voltage drop percentage dedicates the resistance of the teeth and bulk silicon is low enough, and the device performance won't be limited by RC delay at 14.1 GHz .

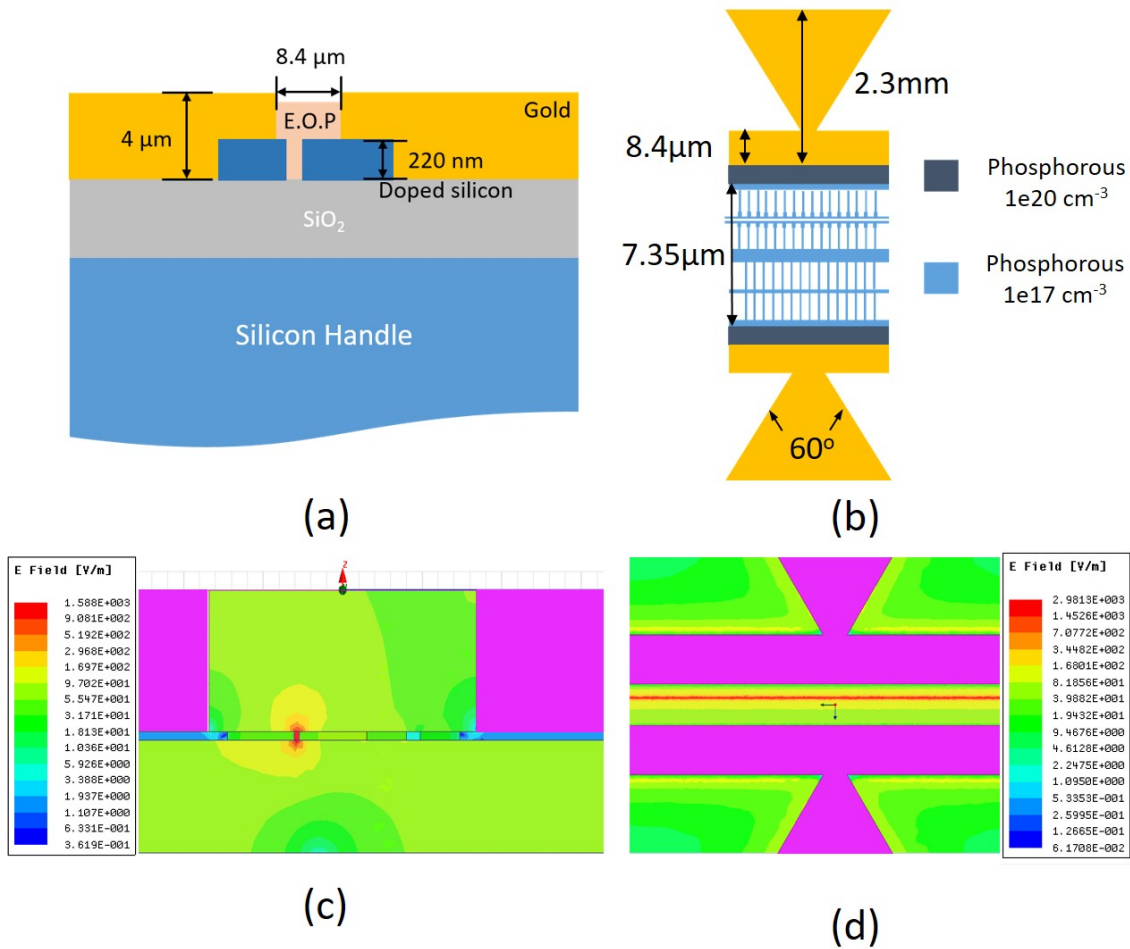


Figure 2.4: (a) Side view and (b) top view of the bowtie antenna with extension bars and ion implantation distribution (c) side view and (d) top view of simulated electric field distribution over the antenna gap region feeding with 14.1 GHz.

2.2.3 Inverse taper coupler design

Fiber to sub-micron silicon single mode waveguide coupling suffers large modal mismatch which results in a significant loss. Two main approaches to this problem are grating couplers [46] and taper couplers [47]. Our group has previously designed and demonstrated a single step, through-etched sub-wavelength grating (SWG) coupler, which can be patterned together with photonic components without any additional

patterning steps. The fiber coupling loss as low as 2.29 dB was demonstrated [46]. However, using an inverse taper coupler can further reduce the coupling loss down to <1 dB as reported [47]. In addition, grating couplers are an inherently bandwidth-limited device with 3 dB optical bandwidth of tens of nanometers. The inverse taper typically has hundreds of nanometers of 3 dB bandwidth [48]. Hence, inverse taper couplers are reported here for efficiently coupling light into the silicon waveguide through design, fabrication, and testing in this session.

The schematic drawing and the geometrical parameters of the inverse taper coupler are shown in Figure 2.5 which are optimized using commercially available software FIMMWAVE. The silicon waveguide is 220 nm in height and is adiabatically tapered from 450 nm to 160 nm (fiber end) in width. An SU-8 polymer pattern is designed and overlaid on the silicon waveguide so that the $3\ \mu\text{m} \times 3\ \mu\text{m}$ cross-section area matches the area of input lens fiber.

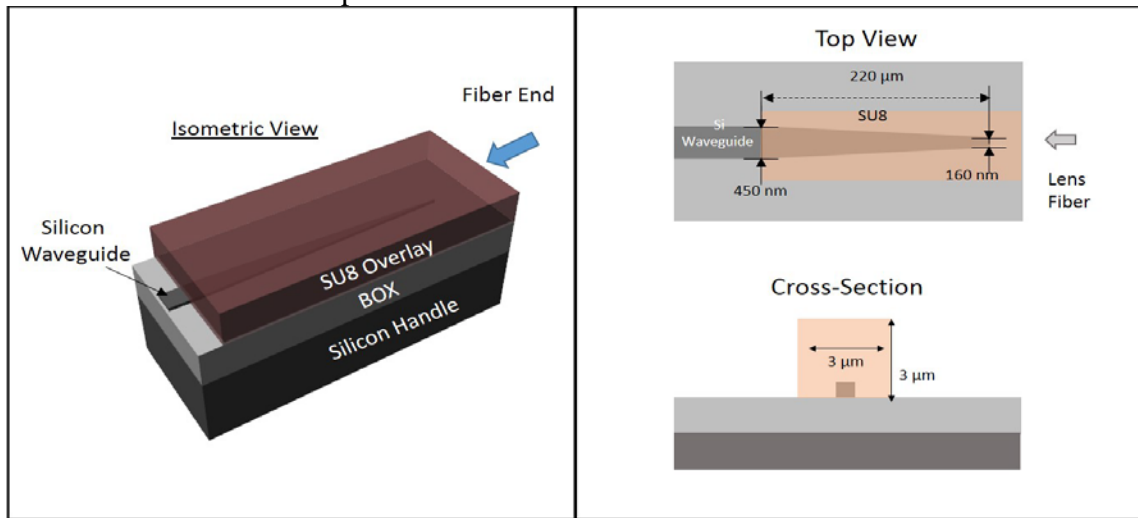


Figure 2.5: Schematic drawing and the designed parameters of the inverse taper coupler.

To characterize the coupling loss per inverse taper coupler, waveguides with different silicon waveguide length are fabricated on the same SOI chip. S-bends with a

radius of curvature 100 μm were added on each waveguide in order to suppress the stray light collected by the output fiber. The silicon waveguide is patterned using electron beam lithography (EBL) and reactive ion etching (RIE). The overlaid SU-8 structure is patterned using MA-6 photo aligner. The SU-8 used here is MicroChem SU-8 2002 and the photolithography conditions such as spin-speed, pre-bake condition, exposure dosage, post-bake condition, and develop time are firstly optimized on a silicon wafer and then inspected before we started to the pattern on the silicon waveguide samples. The scanning electron microscope (SEM) images and the surface profile inspection results of the optimized SU-8 structure are showed in Figure 2.6. The optimized SU-8 pattern is 3.048 μm in width and 3.06 μm in height with side wall angle larger than 85° which are very close to the designed parameters.

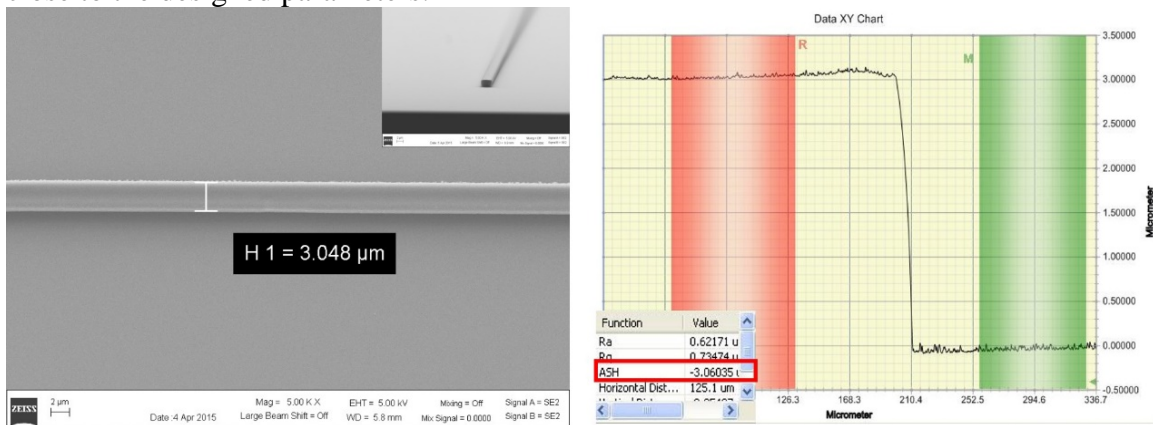


Figure 2.6: Optimized photolithography results of the SU-8 pattern.

After the SU-8 photolithography test, we started to pattern SU-8 layer on the silicon waveguide sample using the optimized condition. The alignment error for both X and Y direction are less than $0.5\mu\text{m}$ between the waveguide layer and the SU-8 layer which are shown in Figure 2.7.

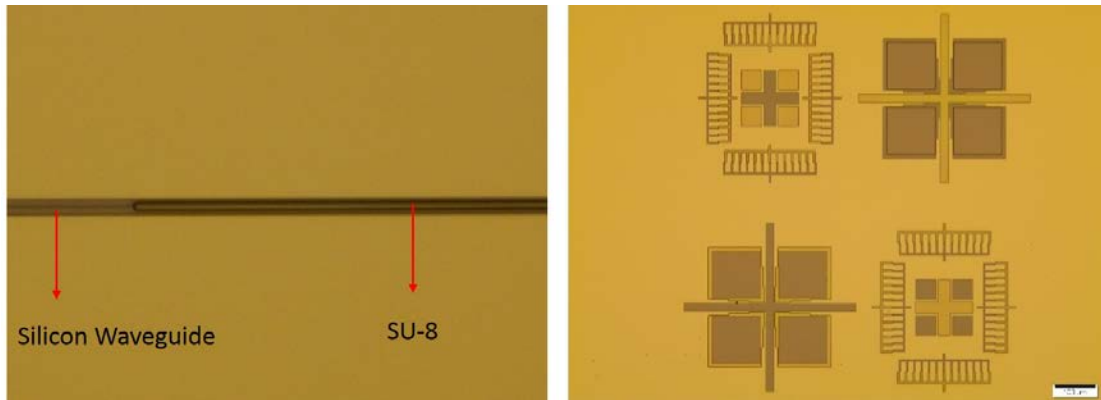


Figure 2.7: Alignment results of the SU-8 layer and the silicon layer.

After device fabrication, we firstly use a diamond scribe to score the chip at the edge of the chip, and then break the chip across the resulting fault. We then measure the length of the chip, so that we can calculate the length for the SU-8 waveguide by subtracting the length of inverse taper and silicon waveguide from the total length. Newport fiber alignment stage was used for the automated alignment of the input and output lensed fiber as shown in Figure 2.8.

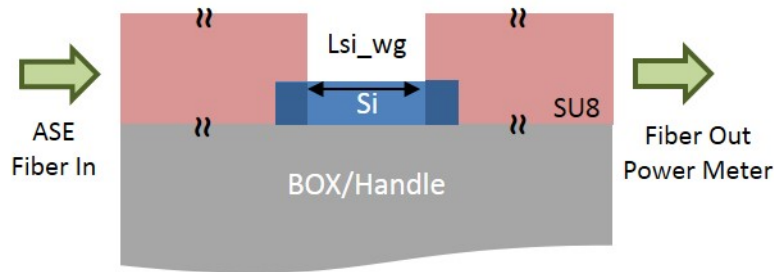


Figure 2.8: The measurement setup schematic for the inverse taper couplers.

Total three waveguides were measured. The fiber to fiber loss was also measured so that we can obtain the insertion loss of each waveguide. After testing all the waveguides, we also tested the solely SU-8 waveguide on buried oxide. The measurement results are shown in Table 1. The SU-8 propagation loss was 1.045 dB/cm which was measured from 2 mm long SU-8 waveguide. By subtracting the loss of SU-8

waveguide and silicon waveguide, we can get the loss of the inverse taper couplers. The minimum loss per taper coupler can be as low as 0.62 dB, and the average loss per inverse taper was 0.941dB.

Testing No.	SU8 WG Length (μm)	Si WG Length (μm)	Total IL (dB)	Loss/ Taper (dB)
1	2560	9628	-6.645	-1.263
2	3560	6628	-4.264	-0.62
3	4560	5128	-4.41	-0.941

Table 2.1: The end-fire coupling measurement results of the fabricated waveguides.

2.3 1D SPCW-BASED EM WAVE SENSOR DEVICE FABRICATION

The fabrication flow of the EM wave sensor is shown in Figure 2.9. The fabrication starts with an SOI chip with 220 nm device layer and 3 μm -thick buried oxide layer implanted with phosphorus of $1 \times 10^{17} \text{ cm}^{-3}$. The cross-shaped platinum alignment marks are patterned for electron-beam (e-beam) lithography alignment as illustrated in Figure 2.9(a). The sample is then implanted on designed opening regions with phosphorus to $1 \times 10^{20} \text{ cm}^{-3}$ and rapid thermal annealed at 1000°C for 10 seconds as shown in Figure 2.9(b). Next, the MZI structure, Y-junction splitter & combiner, and silicon taper for inverse taper couplers are patterned by Jeol 6000 FSE e-beam lithography system and etched by reactive ion etching (RIE) as shown in Figure 2.9(c). The silicon device layer in the antenna region is then etched away through photolithography and RIE so that the antenna can sit on the buried oxide layer to reduce the EM wave reflection as shown in Figure 2.9(d). The 3.8 μm thick antenna is electroplated using 5 nm/100 nm

chromium/gold seed layer with the MZI structure region protected to avoid the contamination in the slot and teeth region. After the seed layer removal with gold and chromium etchant as shown in Figure 2.9(e), the SU-8 inverse taper overlaid layer is patterned as shown in Figure 2.9(f). Finally, EO polymer is formulated, coated, and cured at 80°C in a vacuum oven for overnight. Scanning electron microscope (SEM) images of the sensor are shown in Figure 2.10, which indicate good fabrication accuracy and fine alignment between each fabrication steps. The EO polymer is poled to align the chromophores and initiate the EO effect before waveguide cleaving and the following testing. The poling process is conducted at the EO polymer glass transition temperature of 150°C, with an external electric field of 120 V/ μm . The sensor is then cleaved at the inverse taper coupler region for light coupling.

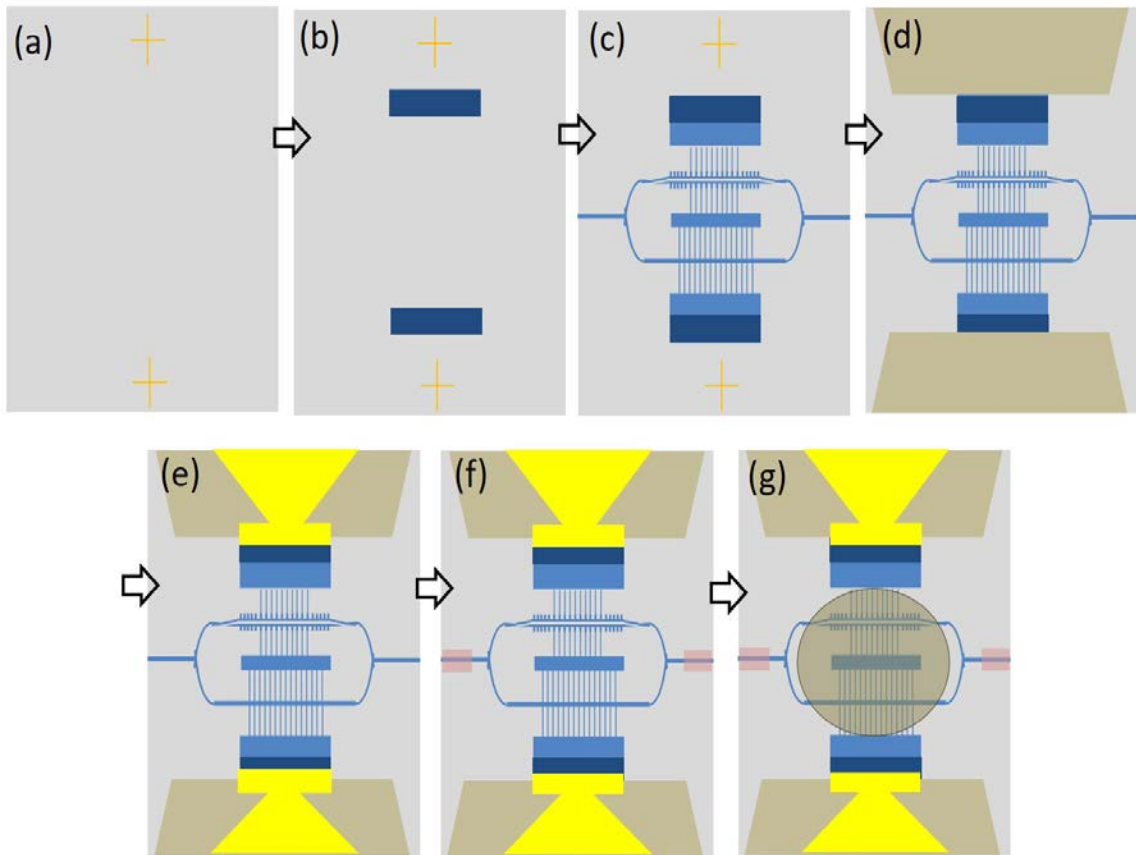


Figure 2.9: Complete fabrication process: (a) 1st implanted bare sample with Pt alignment marks, (b) 2nd implantation and anneal, (c) waveguide patterning and etching, (d) antenna region etching, (e) gold seed layer deposition, electroplating, and seed layer removal, (f) SU-8 inverse taper overlaid patterning, (g) EO polymer coating and curing.

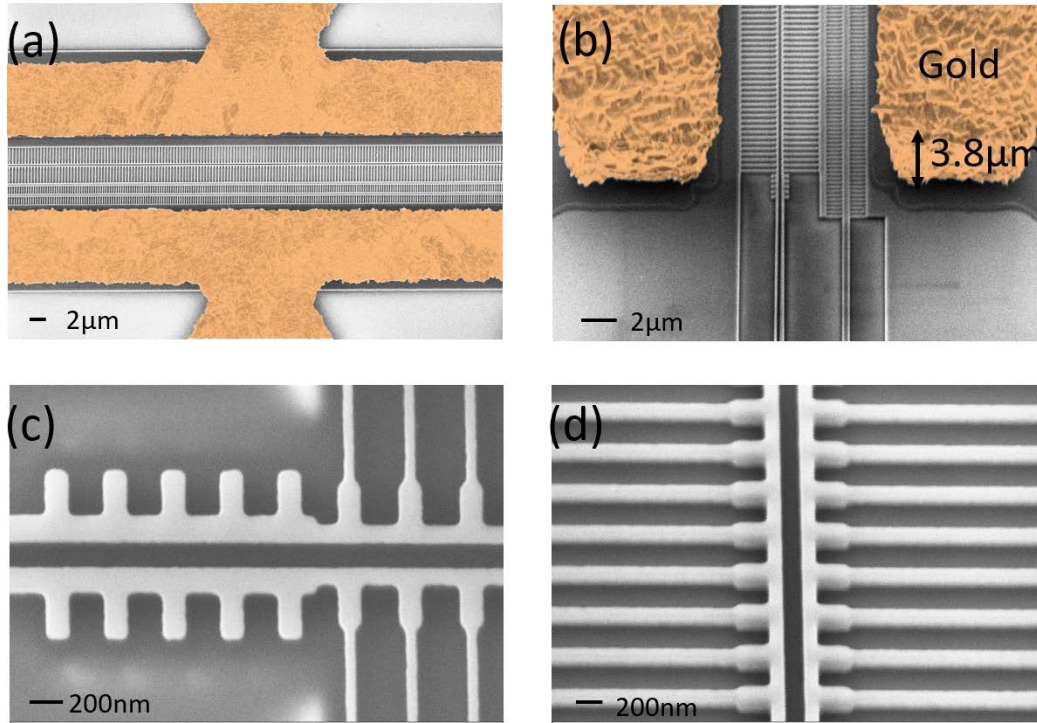


Figure 2.10: SEM images of fabricated device: (a) top view of MZI structure with antenna (colored with orange), (b) tilted cross-section view of the MZI with antenna (colored with orange), (c) top view of 1D SPCW region with 5 sets of step taper, (d) tilted cross-section view of 1D SPCW.

2.4 DEVICE CHARACTERIZATION

2.4.1 Transmission spectra measurement and group index calculation

Transmission spectra of the fabricated devices are obtained using a broadband TE-polarized amplified spontaneous emission (ASE) source with 3 dB bandwidth of 1530 nm to 1610 nm and optical spectrum analyzer (OSA). Two lensed fibers are used for light coupling and positioned on motorized 6-axis stage with precise position control by Newport XPS-Q8 motion controller. A testing 300 μm long 1D SPCW coated with EO polymer on the same chip is firstly tested for optical transmission spectrum. Figure

2.11 shows the normalized transmission spectrum of the EO polymer infiltrated 1D SPCW. A clear band gap at 1569 nm with more than 20 dB extinction ratio can be observed. The lowest optical loss had been measured is 4.39 dB at 1578.32 nm.

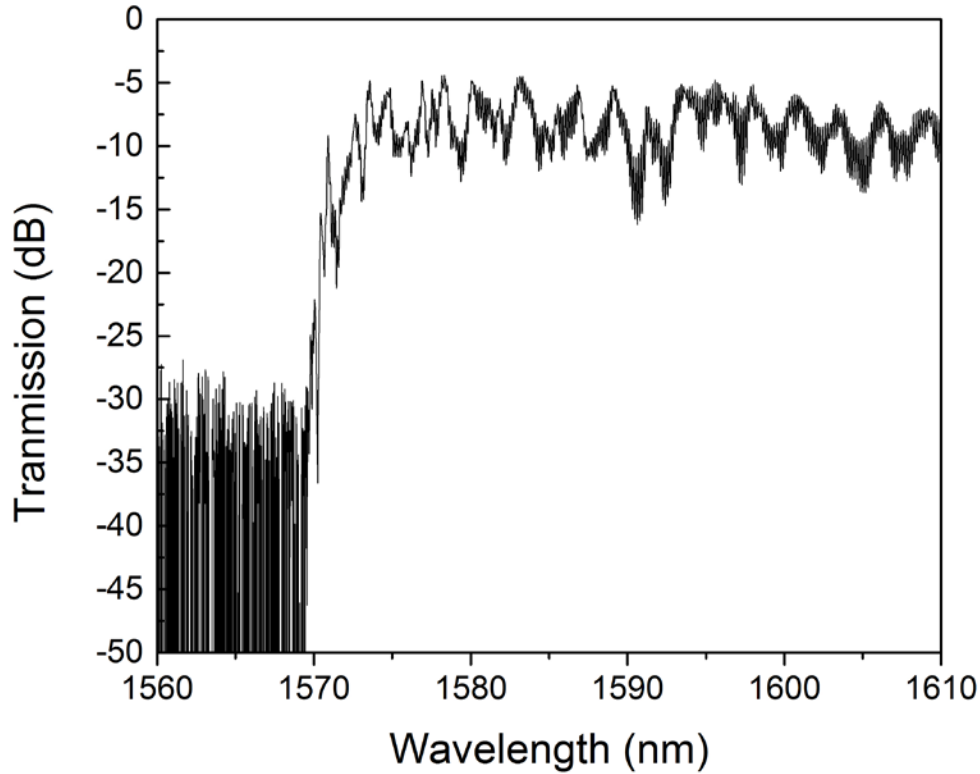


Figure 2.11: Measured transmission spectrum of 300 μm long EO polymer infiltrated 1D SPCW.

The transmission spectrum of the poled MZI structure without applying voltage on the electrodes was then measured as shown in Figure 2.12. Due to the group velocity difference between the two arms and the corresponding optical path difference, the interference pattern is observed and plotted in Figure 2.12. As the group velocity of the 1D SPCW increases at the bandgap, the period of the interference pattern becomes smaller. The group index of each arm has the relationship:

$$n_{g,PCW} = n_{g,ref} + \frac{\lambda_{min} \times \lambda_{max}}{2 \times L (\lambda_{min} - \lambda_{max})} \quad (2.1)$$

where the $n_{g,pcw}$ is the group index of the arm with 1D SPCW, and $n_{g,ref}=3.9$ is the group index of another arm of silicon strip waveguide with teeth. $L=300 \mu\text{m}$ which is the physical length of the phase shifter. The λ_{max} and λ_{min} are the wavelength at local power maxima and minima on the spectrum. As shown in Figure 2.12, the group index of the 1D SPCW can achieve 19.3 at 1545.75 nm. The optical bandwidth of the slow light region ($n_g > 10$) covers 5.13 nm, from 1545.75 nm to 1550.853 nm. The measured slow light wavelength region is blue-shifted 18 nm compared to simulation due to fabrication errors.

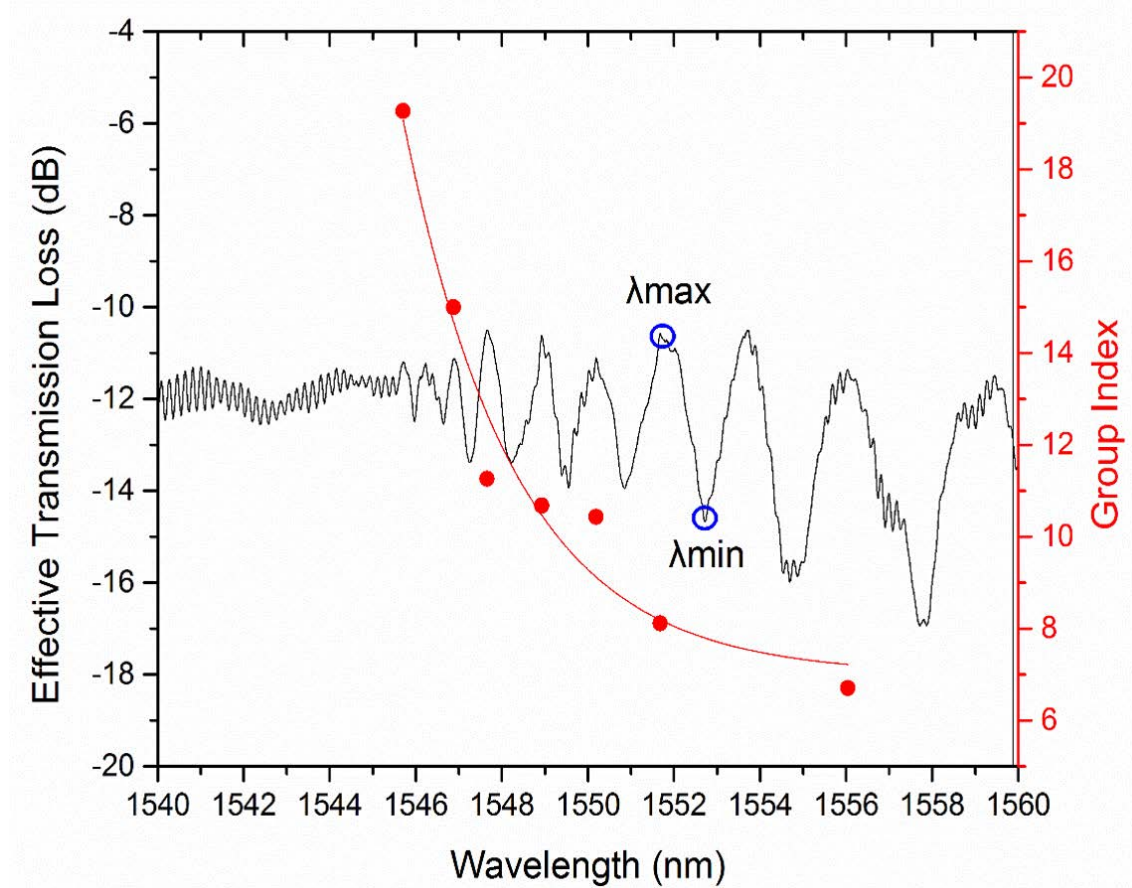


Figure 2.12: continued next page.

Figure 2.12: Measured transmission spectrum of EO polymer infiltrated MZI structure and the calculated group indices of the 1D SPCW as a function of wavelength.

2.4.2 Antenna frequency response measurement

The bowtie antenna is characterized using HP-8510C vector network analyzer (VNA) and GS high-speed probe for the S_{11} parameter to understand the frequency response of the bowtie antenna. As shown in Figure 2.13, the measured S_{11} parameter shows good accordance with simulation results which was performed using ANSYS HFSS with detailed setting reported in other papers [41, 49]. A dip at 14.086 GHz with 3 dB RF bandwidth of 4.84 GHz. The electrical bandwidth of the sensor device is primarily determined by the bowtie antenna since other factors such as EO polymer frequency response, and RC delay of the doped silicon won't limit the sensor bandwidth. Therefore, the bowtie antenna frequency response can be treated as the sensor frequency response.

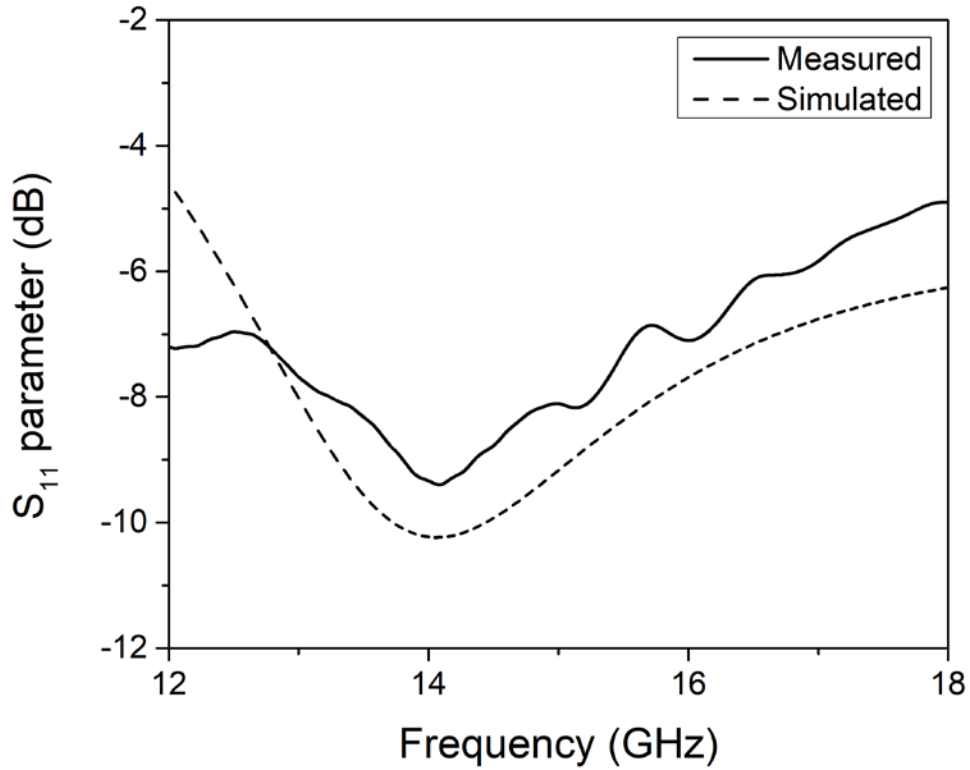


Figure 2.13: Measured and simulated S11 parameter from in Ku band.

2.4.3 EM wave sensing measurements

The EM wave sensing experiment is then conducted, and the setup is shown in Figure 2.14. Same VNA is used as a microwave source. The microwave signal is amplified and then fed into a standard gain horn antenna. The horn antenna emits a wireless microwave signal at normal incidence with respect to the surface of the sensor. The distance of the horn antenna and the device is greater than 40 cm to ensure the far field radiation distance calculated by $2D^2/\lambda$, where D is the largest dimension of the horn antenna aperture and λ is the wavelength of the microwave signal. A polarized tunable laser source at a center wavelength of 1546nm is fed into the device using the

same setup as the passive optical spectrum testing. The output light of the device is connected to New Focus 1014 high-speed photodiode (PD) and then connected to HP 8563E microwave spectrum analyzer (MSA) to analyze the signal. As shown in Figure 2.15, when 6.7 dBm 14.1 GHz signal inputs into the antenna, the MSA reads -82.8 dBm which indicates the optical signal is successfully modulated at the same frequency. The resolution bandwidth of the MSA is 100 kHz and the sweep time is 50 ms.

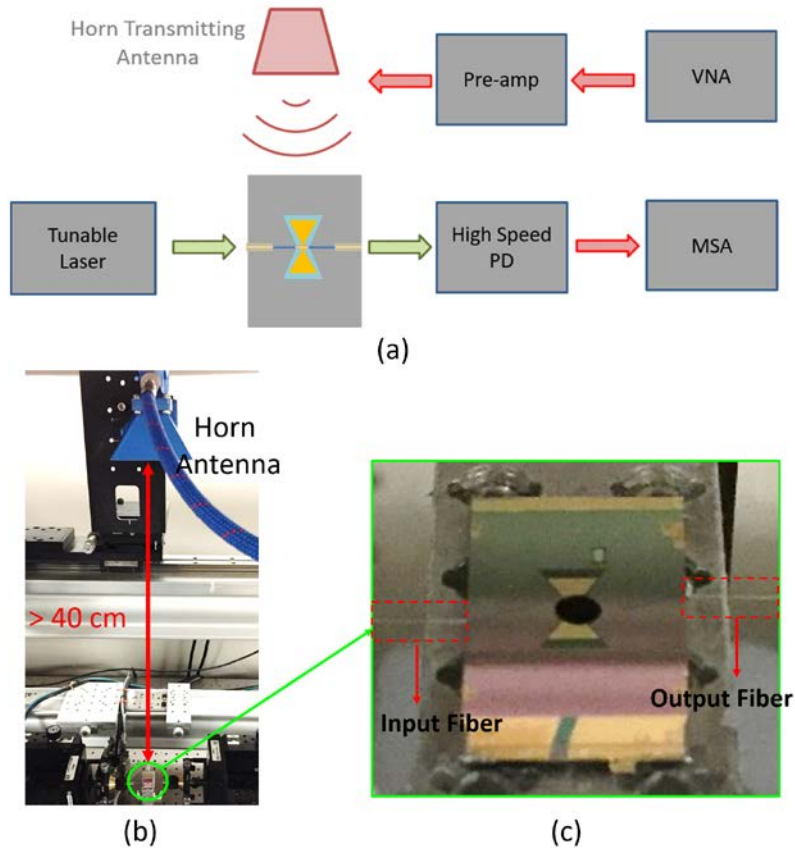


Figure 2.14: (a) Schematic of EM wave sensing testing setup. Green path: optical signal; Red path: electrical signal, (b) horn antenna as transmitting antenna at far field distance with respect to the device, (c) the zoom-in image of the device and two coupling lensed fiber.

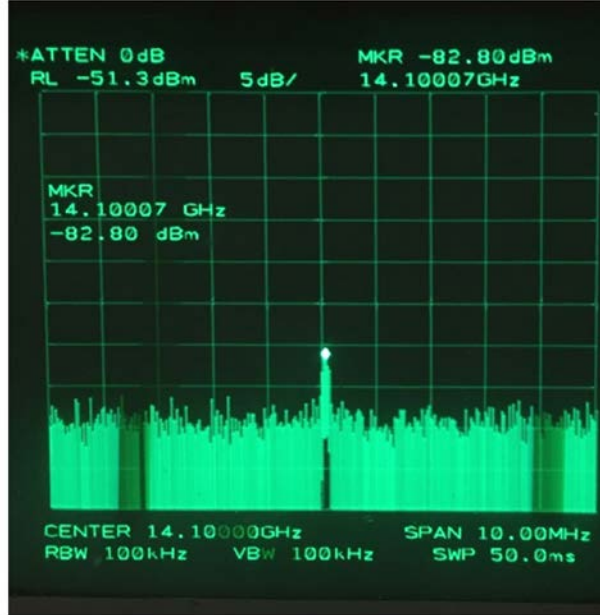


Figure 2.15: MSA reading at 14.1GHz from high-speed PD when the input signal of the horn antenna is 6.7dBm.

A normalized factor is considered to exclude to frequency response caused by horn antenna and obtain the real response of the sensor. Normalized factors (NF) at K_u band are derived from the equation [50]:

$$NF = \frac{P}{P_{max}} = (1 - |\Gamma|^2)G \quad (2.1)$$

where the NF is the power at the interested frequency divided by the power maxima within the frequency range. Γ is the reflection coefficient at the horn antenna port, and G is the antenna gain. The Γ values are obtained using measured S_{11} value with cable and antenna. G is simulated antenna gain in the normal incident direction. In order to determine the limit of detection of the EM wave sensor in terms of electromagnetic wave power density, the relationship between the power density at a certain distance away from the horn antenna and the input microwave power into horn antenna can be firstly derived [51]:

$$S = \frac{G \times P}{4\pi R^2} \quad (2.3)$$

where S is the averaged power density (Poynting vector) in the unit of mW/m², G=10 dB is the horn antenna realized gain with NF at the nominal direction, P is the microwave power input into the horn antenna, and R=42 cm is the distance between horn antenna phase center and sample. Limit of detection of the sensor can be measured by decreasing the input microwave power into the horn antenna when the MSA reading reaches the noise floor. As shown in Figure 2.16, the sensing signal from the reading of MSA versus the input microwave power into the horn antenna is plotted. When the input microwave power decrease to 4.31 mW/m², the MSA reading is -87.43 dBm which is less than 1dB higher than the noise floor. Therefore, the limit of detection of the device at 14.1 GHz is 4.31 mW/m², which is corresponding to the minimum detectable electric field of 1.8 V/m using the equation [52]:

$$|E| = \sqrt{\frac{2S}{\epsilon_0 \epsilon_r C}} \quad (2.4)$$

where ϵ_0 is the vacuum dielectric constant, ϵ_r is the dielectric constant of air, c is the speed of light, and S is the averaged power density from the horn antenna.

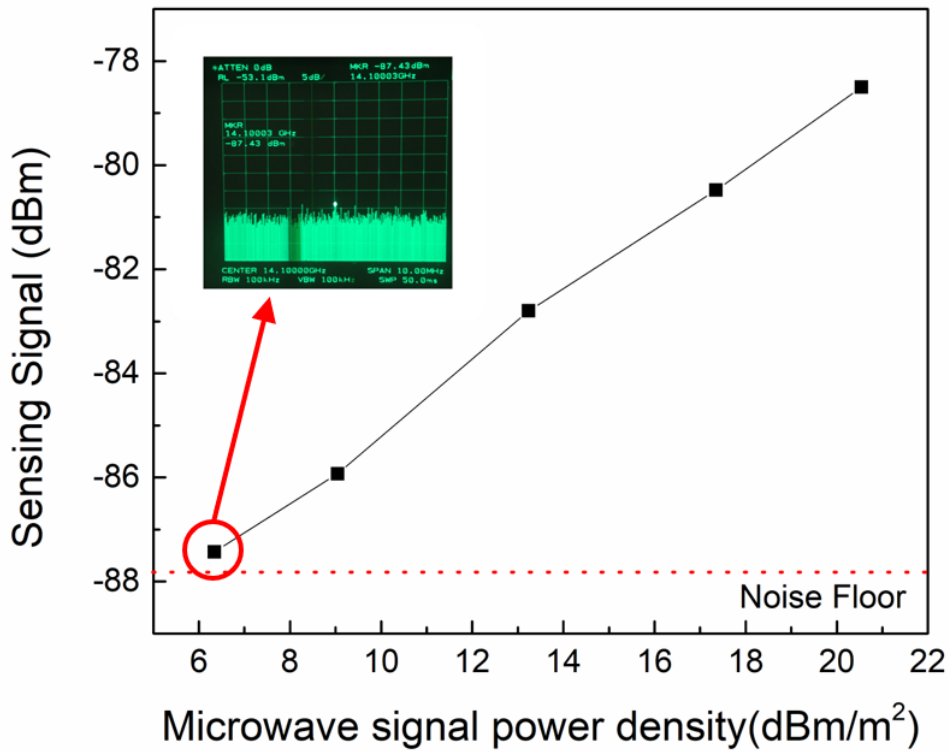


Figure 2.16. Measured sensing signal reading from MSA versus different microwave input signal power.

2.5 CONCLUSION

We proposed and experimentally demonstrated a compact and sensitive on-chip EM wave photonic sensor operating at 14.1 GHz with 4.84 GHz RF bandwidth. The sensor is based on bowtie antenna coupled MZI structure with one arm of low-loss slow-light enhanced EO polymer infiltrated 1D SPCW and the other arm of silicon strip waveguide with teeth. The silicon teeth design in both arms is for electrical connection purpose with careful implantation design so that voltage drop can occur in 150 nm slot region. The sensor device has advantages of compact size (4.6 mm × 4.8 mm), low

optical loss (~ 10 dB), and high sensitivity; therefore, has potential to be adopted in various communication and sensing applications. The limit of detection at 14.1 GHz is 4.31 mW/m^2 , which is corresponding to the minimum detectable electric field of 1.8 V/m .

Chapter 3: On-Chip Photonic Electromagnetic Wave Sensor Featuring Silicon-Polymer Hybrid Subwavelength Grating Waveguide and Bowtie Antenna

A photonic electromagnetic (EM) wave sensor based on electro-optic (EO) polymer infiltrated silicon sub-wavelength grating (SWG) waveguide and bowtie antenna is designed and experimentally demonstrated. The EM wave sensor receives wireless microwave signals via the bowtie antenna and concentrates the electrical field between the extension bars of the bowtie antenna to modulate the light guided in the SWG waveguide-based Mach–Zehnder interferometer (MZI). Thus, microwave signals can be detected by measuring the intensity variation of light from the MZI output. The EO polymer infiltrated SWG does not require ion implantation and has low propagation loss. Furthermore, compared to nanoscale slotted silicon waveguides, the EO polymer poling efficiency on SWG structure can be greatly increased due to wider poling separations and thus the increased breakdown voltage. In order to achieve strong microwave field enhancement, the impedance of the bowtie antennas is tailored. The optimized bowtie antenna operates at 15 GHz and occupies only an area of 7.6 mm X 0.3 mm. Leveraging the SWG waveguide, high EO coefficient polymer, and large field enhancement from the bowtie antenna, an ultra-sensitive and compact EM wave photonic sensor operating at 15 GHz has been demonstrated. Experimental results show the limit of detection at 15 GHz is 4.48 mW/m^2 , which is corresponding to a minimum detectable electric field of 1.83 V/m.

3.1 INTRODUCTION

Conventional electrical microwave sensing requires high-speed metallic probes, which not only block the EM wave to be tested but also introduce EM noise. Furthermore, discrete high-speed electronic components such as antennas, regulators,

electrical cables, and amplifiers are needed in the completed electrical sensing circuit. Antenna-coupled photonic microwave EM wave sensors [6, 23, 53] has been a popular research topic since they eliminate the need of lossy and bulky electronic components and have numerous advantages such as high-frequency operation with low loss, high sensitivity, and compact in size as reported in the previous chapter. The antenna coupled photonic microwave sensors have great potential for communication [54] and sensing applications [55-57].

In Chapter 2, we have reported a highly sensitive photonic EM wave sensor featuring EO polymer infiltrated one-dimensional (1D) slotted photonic crystal waveguide (SPCW). By taking advantage of slow light enhanced EO effect on the low loss 1D SPCW, the limit of detection at 14.1 GHz can be pushed down to 4.31 mW/m^2 , which is corresponding to the minimum detectable electric field of 1.8 V/m . Although a highly sensitive photonic EM wave sensor is achieved, there is still some room for improvements. Firstly, for 1D SPCW with 150 nm wide EO polymer infiltrated slot, the degraded poling efficiency and yield of the EO polymer in nanoscale slots so as to decrease the in-device EO coefficient been observed and studied in other literature [58]. There are several possible causes for this degradation when compared with bulk EO polymer: 1. There are imperfections of nanoscale EO polymer infiltrated slot (i.e., voids and rough side-wall surfaces of the slot) which cause poling and sensing electric field inhomogeneous in the slot. 2. There are imperfections between the interface of electroplated electrodes and silicon after multiple lithography and ion implantation process. 3. EO coefficient and resistivity decrease and depends on the geometry under nanoscale. Secondly, the proposed structure reported in Chapter 2 requires a complicated doping design on silicon. The two-step ion implantation process causes not only damage to the surface due to ion bombardment but also decrease in fabrication yield because of

the difficulty for removing partially carbonized masking photoresist after high energy implantation. Finally, the electroplated antenna has a large surface roughness around 500 nm which also cause the inhomogeneous electric field distribution between the antenna gap and therefore efficiency and yield reduction of poling and sensing.

Subwavelength grating (SWG) waveguides and photonic devices have gained great research interests recently [59-61]. The silicon SWG waveguide consists of spatially periodic silicon pillars with a pitch much smaller than the operating wavelength. If EO polymer is spin-coated on such an SWG waveguide and forms an EO phase shifter, effective interaction region between guided light wave and EO polymer includes not only the top and sides of the waveguide where evanescent wave exists but more importantly the space between silicon pillars on the light propagation path. The confinement factor of a TE mode SWG waveguide, which is defined as power confined in the EO polymer layer divided by power in all layers of the waveguide structure, can be as large as 40 % [62] while 1D SPCW reported in the previous chapter only has confinement factor of 24 %. Therefore, the in-device EO effect can be increased when adopting EO polymer infiltrated the SWG waveguide structure.

In this chapter, we proposed an EO polymer infiltrated SWG waveguide-based EM wave sensor as shown in Figure 3.1. The sensor consists of a high electric field enhancement bowtie antenna an MZI structure with one arm of EO polymer infiltrated SWG waveguide and the other arm of a reference silicon strip waveguide. A continuous wave (CW) laser light is coupled in and out through the grating couplers [63]. The bowtie antenna collects the impinging microwave EM waves and concentrates the field into the feed gap of the bowtie antenna. The EO polymer infiltrated SWG phase shifter converts the electromagnetic wave into phase modulation and transforms into the intensity variation by the MZI. By measuring the optical power variation from the output end of

the MZI, an incident electromagnetic field from free space can be detected through this optical mean. The bowtie antenna is re-designed and has a thickness of 720 nm which thinner than the one reported in Chapter 2. Therefore, it can be done with e-beam evaporator and avoids imperfections caused by electroplating. By adopting this EO polymer infiltrated SWG waveguide-based EM wave sensor, several advantages can be obtained over EO polymer infiltrated 1D SPCW based EM wave sensor: Firstly, the poling and sensing electric fields are applied across 9.12 μm wide EO polymer infiltrated antenna gap instead of 150 nm wide slot. Therefore, there is no degradation of EO polymer and geometry dependent effect as mentioned above and poling efficiency, as well as poling yield, can be improved. Secondly, the optical confinement in the EO polymer layer of the EO polymer infiltrated SWG waveguide is improved from 1D SPCW. Finally, this structure doesn't confine electric field via the electrical connection of silicon. Thus, it doesn't require multiple steps of ion implantations and the fabrication yield can be improved. There is no slow light effect at the vicinity of 1550 nm using this EO polymer infiltrated SWG waveguide. However, the EO polymer infiltrated SWG waveguide has lower propagation loss than 1D SPCW which helps to maintain high sensitivity.

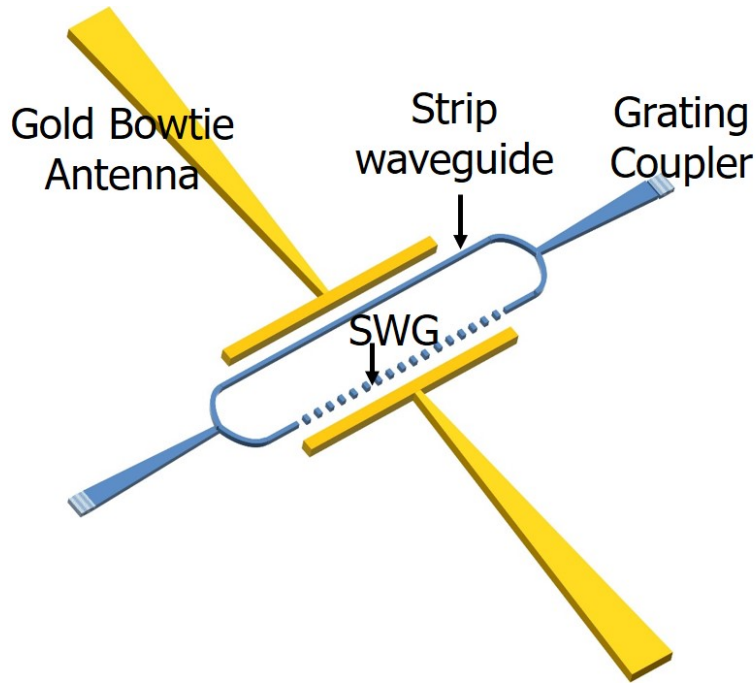


Figure 3.1: Schematic of the proposed EM wave sensor based on a bowtie antenna coupled MZI structure. MZI structure is composed of an EO polymer infiltrated SWG waveguide and a silicon strip waveguide. The wireless microwave signal is collected and concentrated in the antenna gap for EO modulation on the SWG arm. Grating couplers are adapted for efficient light coupling.

3.2 DEVICE DESIGN

3.2.1 EO polymer infiltrated SWG waveguide

The SWG waveguide is designed with SEO125 ($n=1.63$ at 1550nm) EO polymer as a top cladding layer. This EO polymer shows a large bulk EO coefficient r_{33} of 135 pm/V , low optical loss, and good temporal stability and therefore is chosen to fill the silicon SWG waveguide. The schematic diagram and geometrical parameters of the SWG waveguide are shown in Figure 3.2. The SWG is designed to build on SOI wafer with 220 nm silicon device layer. The period (a) of the EO polymer infiltrated SWG is chosen to be 350 nm so that the SWG is operating at subwavelength regime [60]. Silicon pillar

length (s) and width (w) are optimized to be 220 nm and 540nm respectively using 3D PWE method and 3D FDTD method to achieve large confinement factor while considering an acceptable optical loss.

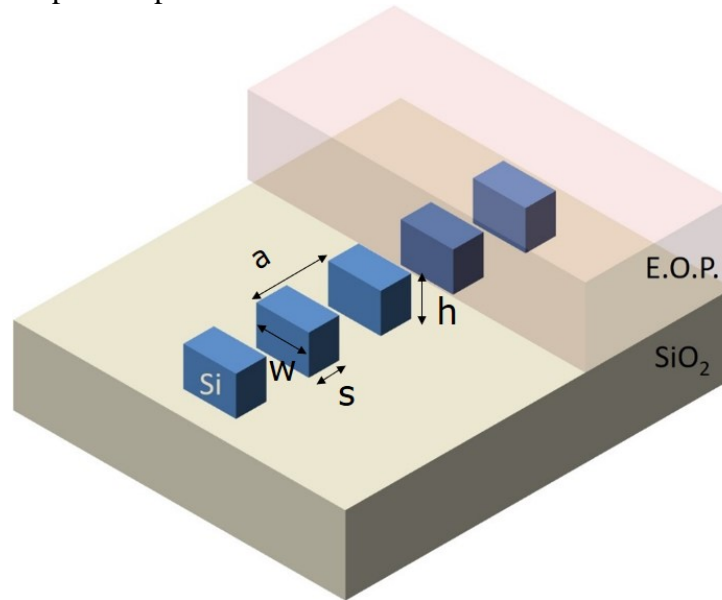


Figure 3.2: Schematic of the EO polymer infiltrated SWG waveguide. It consists of spatially periodical silicon pillars with a subwavelength period.

3.2.2 Thin bowtie antenna design with high field enhancement

Due to the potential electroplating problems when fabricating a bowtie antenna with $\sim 4 \mu\text{m}$ thick gold layer, a new bowtie antenna with a thinner gold layer of 720 nm is designed for the SWG waveguide-based MZI. The thin bowtie antenna can be fabricated using e-beam evaporation instead of electroplating. The schematic of the designed bowtie antenna and is shown in Figure 3.3. The gap between the extension bars is $9.12 \mu\text{m}$. This antenna is designed to operate at 14.1 GHz using ANSYS HFSS. The antenna stands on the buried oxide layer and has a thickness of 720 nm, the arm length of 3.802 mm, flare angle of 1 degree and extension bars of $2 \mu\text{m} \times 300 \mu\text{m}$. The thin gold layer and small

angle help to increase the field enhancement in the antenna gap as field enhancement is proportional to the square root of antenna impedance:

$$F.E. = \frac{E_{gap}}{E_{input}} = \frac{\sqrt{Z}}{w_{gap}} \sqrt{\frac{\lambda_{RF}^2 G}{4\pi Z_0}} \propto \sqrt{Z} \quad (3.1)$$

Where E_{gap} is the electric field in the antenna gap, E_{input} is the incoming electric field, Z is the antenna impedance, w_{gap} is the antenna gap width, λ_{RF} is the wavelength of the RF signal, G is the antenna gain, and Z_0 is the impedance of free space.

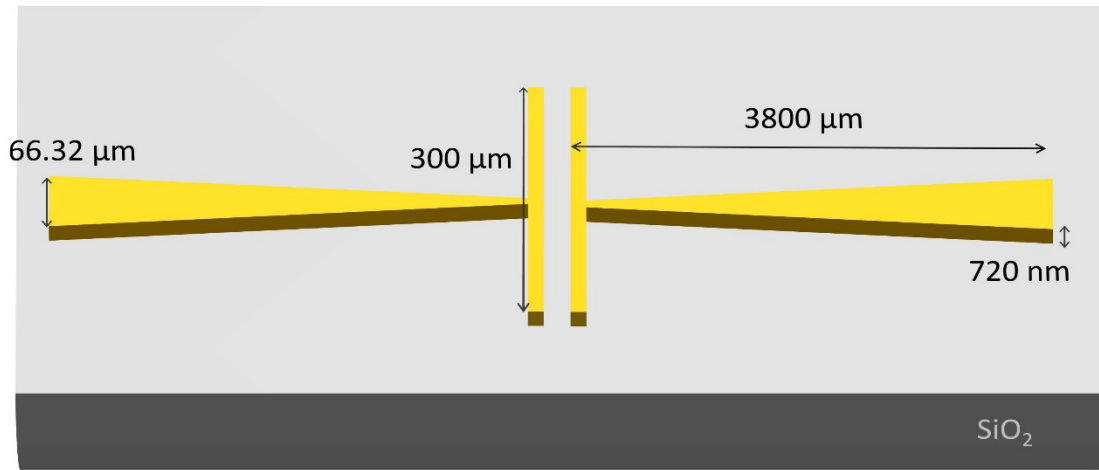


Figure 3.3: Schematic of the thin gold bowtie antenna with extension bars standing on the buried oxide layer of the SOI wafer.

3.3 SWG WAVEGUIDE-BASED EM WAVE SENSOR DEVICE FABRICATION

The fabrication flow of the SWG waveguide sensor device is illustrated in Figure 3.4. The fabrication starts with an SOI wafer with a 220 nm-thick top silicon and a 3 μm-thick buried oxide layer, as shown in Figure 3.4(a). The MZI structure, Y-junction splitter & combiner, grating couplers are patterned by electron-beam (e-beam) lithography and etched by reactive ion etching (RIE). In Figure 3.4(b), the silicon device layer of the antenna region is then etched away through photolithography and RIE so that the antenna can stand on the buried oxide layer as designed. The 720 nm gold antenna with 5 nm

chromium adhesion layer is patterned using e-beam evaporator and photoresist lift-off mask as shown in Figure 3.4(c). Finally, EO polymer is formulated, coated, and cured at 80°C in a vacuum oven for overnight. In Figure 3.5, the scanning electron microscope (SEM) images of the sensor show good fabrication accuracy and fine alignment between each fabrication steps. The EO polymer is poled at its glass transition temperature by applied external DC electric field of 90 V/μm on a 150°C hotplate to align the chromophores and initiate the EO effect. The sensor is then ready for the following optical and EM wave sensing testings.

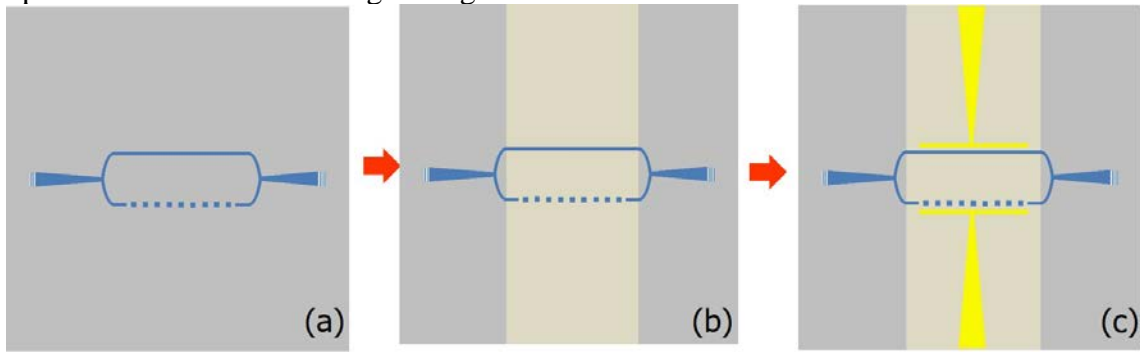


Figure 3.4: Fabrication steps of the SWG waveguide-based sensor device: (a) optical waveguides and grating couplers patterning and etching, (b) antenna region etching, (c) gold thin bowtie antenna patterning.

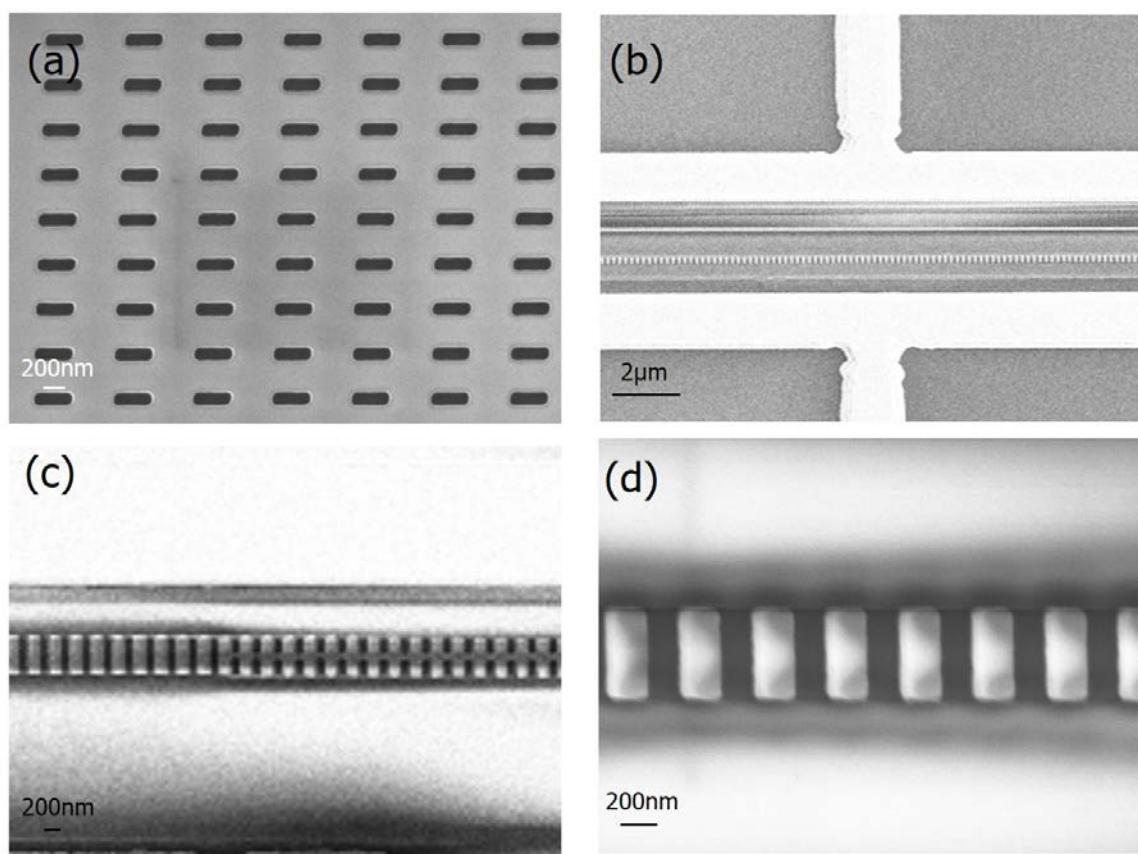


Figure 3.5: SEM images of the fabricated device: (a) grating couplers, (b) bowtie antenna and MZI structure in the antenna gap. One arm is a silicon SWG waveguide and another is a silicon strip waveguide, (c) SWG waveguide and taper region connecting to strip waveguide, (d) SWG waveguide.

3.4 DEVICE CHARACTERIZATION

The transmission spectrum of the device is obtained using a broadband TE-polarized amplified spontaneous emission (ASE) source with 3 dB bandwidth of 1530 nm to 1610 nm and optical spectrum analyzer (OSA). Polarization maintaining fiber is used for the input end and single mode fiber is used the output end. Fiber angle for lowest coupling loss occurs at 14 degrees. As shown in Figure 3.6, a minimum optical loss for 300 μm long EO polymer infiltrated SWG sensor device is 0.44 dB. The device has greater than 35 dB on-off ratio in the spectrum which indicates the SWG waveguide has a

comparable optical loss with respect to silicon strip waveguide and therefore strong interference pattern is formed.

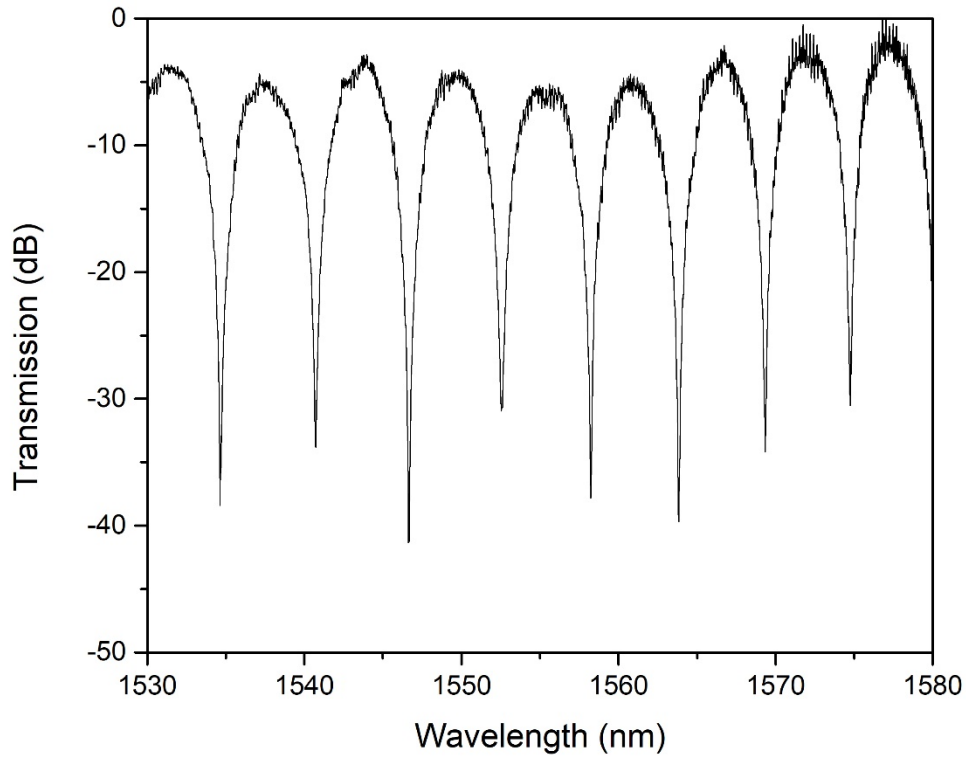


Figure 3.6: Measured transmission spectrum of the SWG waveguide-based EM wave sensor device.

For EM wave sensing test, the device is characterized using the experimental setup shown in Figure 3.7(a). A polarized tunable laser operating at a center wavelength of 1550.5nm as a light source is fed into the device using the same setup as the passive optical spectrum testing. The microwave signal with a single frequency from a vector network analyzer (VNA) is firstly amplified and then fed into a standard gain horn antenna. The horn antenna emits a wireless microwave signal at normal incidence with respect to the surface of the sensor. The 70-cm separation between the horn antenna and

the device is in the far-field region of the horn antenna which is calculated by $2D^2/\lambda$, where D is the largest dimension of the horn antenna aperture and λ is the wavelength of the microwave signal. Testing electric field is fixed at 8 V/m from 15-20 GHz. The modulated light coupled out of the chip is analyzed with an OSA for sidebands.

As shown in Figure 3.7(b) and 3.7(c), the optical carrier with sidebands at the different microwave frequencies are visible which indicates the output light from the device is successfully modulated. The side-band is ~ -45 dB lower than the main peak.

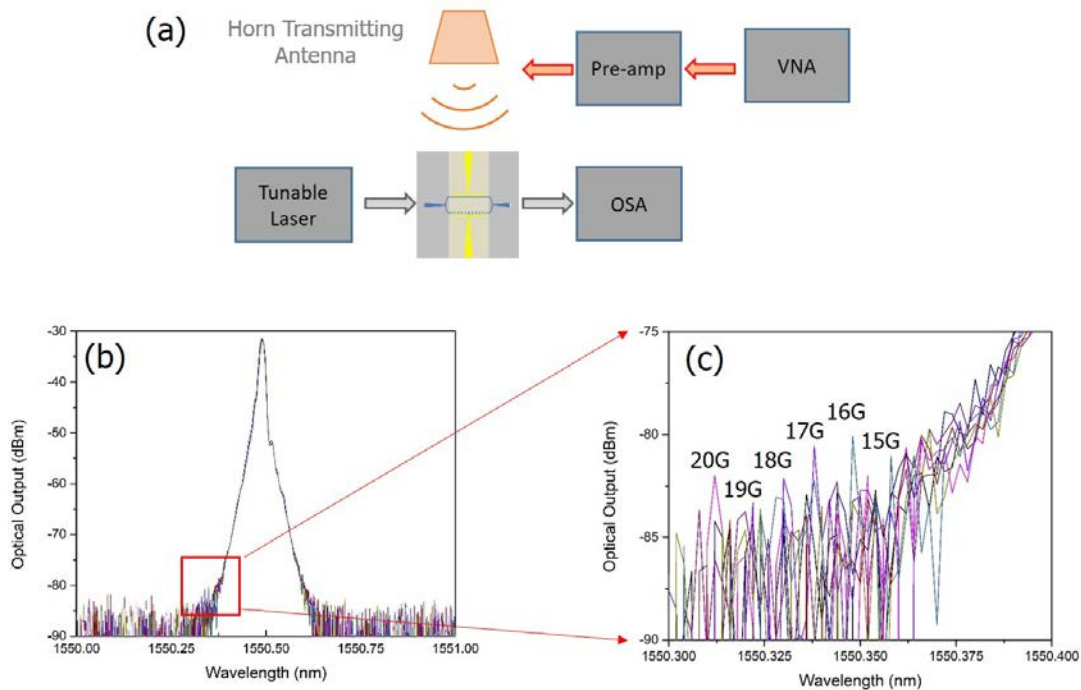


Figure 3.7: (a) Optical sideband testing setups for microwave detection, (b)(c) measured optical response of the device with sidebands at modulating frequencies from 15-20 GHz.

The limit of detection of EM wave sensing is tested with the setups shown in Figure 3.8(a). Same microwave source, horn antenna, and optical testing setups are used here. Instead of connecting the output of the device to OSA, the output light of the device is connected to New Focus 1014 high-speed photodiode (PD) and then connected to HP

8563E microwave spectrum analyzer (MSA) to analyze the signal. To determine the limit of detection of the EM wave sensor in terms of electromagnetic wave power density, the same equation in Chapter 2 is again used here. The relationship between the power density at a certain distance away from the horn antenna and the input microwave power into horn antenna can be derived:

$$S = \frac{G \times P}{4\pi R^2} \quad (3.2)$$

where S is the averaged power density (Poynting vector) in the unit of mW/m², G=17.5-20 dB at 14-17 GHz is the horn antenna realized gain, R is the 70 cm separation between horn antenna and the device, and P is the microwave power input into the horn antenna. Limit of detection of the sensor can be measured by decreasing the input microwave power into the horn antenna when the MSA reading reaches the noise floor. As shown in Figure 3.8(b), the limit of detection of the device at different frequencies are plotted. As the result shows, the lowest limit of detection occurs at 15 GHz and is 4.48 mW/m², which is corresponding to the minimum detectable electric field of 1.83 V/m using the same equation in Chapter 2:

$$|E| = \sqrt{\frac{2S}{\varepsilon_0 \varepsilon_r C}} \quad (3.3)$$

where ε_0 is the vacuum dielectric constant, ε_r is the dielectric constant of air, c is the speed of light, and S is the averaged power density from the horn antenna.

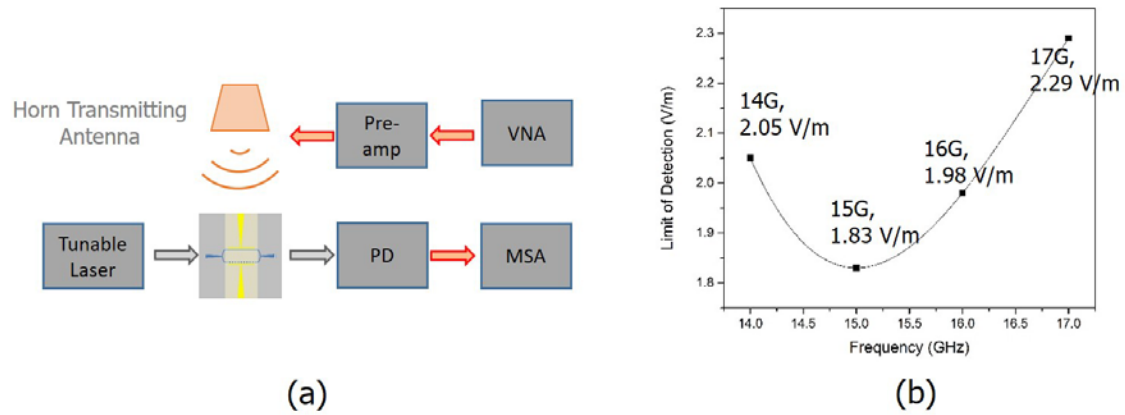


Figure 3.8: (a) Limit of detection testing setups for EM wave sensing, (b) measured limit of detection of the SWG sensor device at 14-17 GHz.

3.5 CONCLUSION

In summary, we experimentally demonstrate a photonic EM wave sensor based on EO polymer infiltrated silicon SWG waveguide and bowtie antenna. The proposed structure detects wireless microwave signal by measuring the modulated optical signal from the antenna-coupled MZI featuring SWG. The EO polymer infiltrated SWG has low optical loss, excellent optical confinement in the EO polymer layer, and great poling efficiency. The bowtie antenna operates at 15 GHz occupy only an area of 7.6mmX 0.3mm. Limit of detection at 15 GHz can be achieved as low as 4.48 mW/m², which is corresponding to a minimum detectable electric field of 1.83 V/m.

Chapter 4: Fishbone-Structured One-Dimensional Photonic Crystal Waveguide Integrated Photonic Chip for Ultra-Compact Optical True-Time Delays

An ultra-compact on-chip optical true-time-delay line features the slow light effect enabled by fishbone-structured (FS) one-dimensional (1D) photonic crystal waveguide (PCW) is demonstrated. The structural slow light is generated by modulating the index guided optical mode with periodic sidewalls along the propagation direction. Due to the reduced mode volume overlap with the high roughness etched surface, the propagation loss of the FS 1D PCW is significantly reduced compared to 2D PCW. A delay time of 65 ps/mm which corresponds to the group index of 19.47 is observed experimentally.²

4.1 INTRODUCTION

Microwave signal processing and transmission demand large bandwidth time delays, but electrical phase shifters intrinsically have a narrow bandwidth, which significantly deteriorates the performance of microwave systems. For example, phased array antenna (PAA) has advantages of high directivity and fast steering [64], making it an intriguing technology for high-performance communication and radar systems for both civilian [65] and military applications [66]. The array is composed of multiple sets of antenna units with their own phase shifters. The signal from the transmitter is fed into each phase shifter. By tuning the phase shift and therefore the interference relationship between each antenna unit, beams of the radio frequency (RF) wave at desired frequency range are formed to point into the desired direction. Due to the narrow bandwidth of

² Portions of this chapter have been published in C.-J. Chung, X. Xu, G. Wang, Z. Pan, and R. T. Chen, "On-chip optical true time delay lines featuring one-dimensional fishbone photonic crystal waveguide," *Applied Physics Letters*, vol. 112, p. 071104, 2018.

C.-J. Chung designed and fabricated the device, performed the experiments, analyzed the data, and wrote the manuscript.

electrical phase shifters and thus induced beam squint effect, the bandwidth of the PAA system is extremely narrow.

Optical true time delay line (OTTDL) is a promising alternative as its bandwidth is intrinsically large. Numerous OTTDL designs have been studied so far, including bulk optics [67], dispersive fiber [68], and acoustic-optic integrated circuit [69]. These photonic solutions consist of discrete or low dispersion optical components and therefore are bulky in size to provide satisfied steering range and/or have stringent alignment condition. Recently, various on-chip OTTDL structures have been demonstrated to realize ultra-compact and robust TTD lines such as photonic crystal waveguides (PCW) [70], polymer waveguides [71], and graphene-based waveguide [72]. Among these structures, due to the strong optical confinement [37], enhanced the slow-light effect and high dispersion [2], silicon PCW TTD lines can contribute to the reduction in footprint and power consumption when operating in the high group index region. Besides, the cost of silicon PCW photonic chips can be greatly reduced by utilizing matured CMOS fabrication facilities. Slow light enhanced silicon fishbone-structured (FS) one-dimensional (1D) PCW has been reported with lower optical propagation loss due to less etched surface area overlapped with optical mode compared to two-dimensional (2D) PCW while keeping similar slow light effect [38]. Furthermore, FS 1D PCW is less susceptible to fabrication variations comparing with 2D PCW [38], making it a good candidate for on-chip OTTDL. In this chapter, we experimentally demonstrated an on-chip wavelength tunable OTTDL featuring FS 1D PCWs, which can be used in microwave applications such as multi-frequency PAAs. The proposed TTD module based on FS 1D PCW provides compact footprint, low loss, high dispersion, and slow light enhancement and has potential as a high-performance on-chip wavelength tunable optical TTD.

4.2 FS 1D PCW DEVICE DESIGN

Figure 4.1(a) illustrates the schematic of the FS 1D PCW. The structural slow light is generated by periodically modulated sidewalls along the propagation direction, and the light is confined in the vertical directions through index guiding. Since laterally odd modes are difficult to excite with a monomode strip waveguide, we will focus on laterally even modes, which are also referred as quasi-transverse electrical (quasi-TE) modes. The band diagram of even modes in the FS 1D PCW is shown in Figure 4.1(b). The light cone regions represent modes that extend into the top or bottom claddings. Incomplete band gaps exist between band 1 and 2, as well as band 2 and 3, as illustrated by the green regions in Figure 4.1(b). The mode profiles ($|E_z|^2$) of the modes are shown in Figure 4.1(c~h). The corresponding group index is plotted in Figure 4.1(i). Eminent slow light phenomena are observed close to the edge of the Brillouin zone. In band 0, as $a/\lambda \ll 1$, the periodic corrugation can be considered as a uniform material according to effective medium theory except for the region near the band edge, where $a/\lambda \sim 0.216$. The slow light bandwidth is very narrow and thus not suitable for TTDs due to the power penalty induced by large group velocity dispersion (GVD). Band 1 and 2 have larger slow light bandwidth due to the anti-crossing effect. Slow light occurs not only near the band edge but also near the anti-crossing point. However, there are two modes exist, as shown in Figure 4.1(i), making it difficult to selectively couple into one of the modes. Thus, we concentrate on band 2.

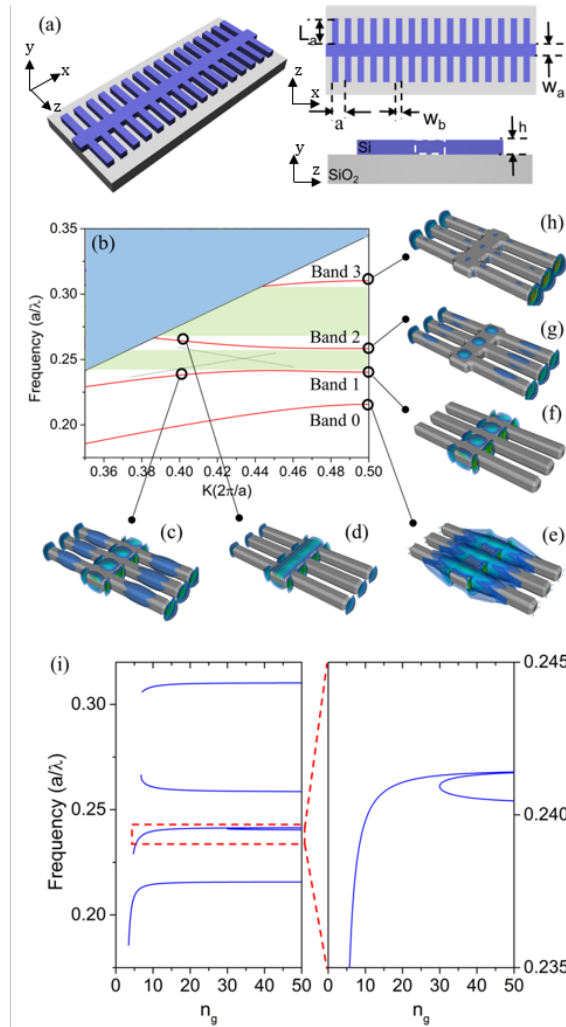


Figure 4.1: (a) Schematic of the proposed FS 1D PCW structure, (b) band diagram of the FS 1D PCW. (c-h) E_z distributions of the modes in band 0-3. (i) group indices of the bands.

The PCW structure is optimized with 3D plane wave expansion method targeting at generating large time delay with a compact footprint. As shown in Figure 4.2, the period (a), tooth width (W_b), tooth length (L_a), and center strip width (W_a) are optimized to be 400 nm, 188 nm, 1000 nm, and 400nm respectively, and the structure is designed to be built on silicon-on-insulator (SOI) wafer with 220 nm thick device silicon layer and 3 μm

thick buried oxide (BOX) layer. This proposed structure also benefits from lateral index guiding instead of bandgap guiding in 2D PCW. Therefore, the waveguide width is only 2.4 μm which is $> 70\%$ size reduction of the one in 2D PCW. The simulation results prove the slow light effect with a minimum group index of 6.3 and strong GVD which is around -1.5×10^7 ps/(nm \cdot km) as shown in Figure 4.2(a). 50 ps delay time can be easily achieved with 1 mm FS 1D PCW through tuning the wavelength between 1530 nm to 1565 nm where group index is greater than 15. In order to reduce the strong reflection at the interface between a strip waveguide and FS 1D PCW, step tapers comprising four periods are designed between FS 1D PCW and silicon strip waveguide so that the coupling efficiency is greatly increased up to 71.96% as shown in Figure 4.2(b).

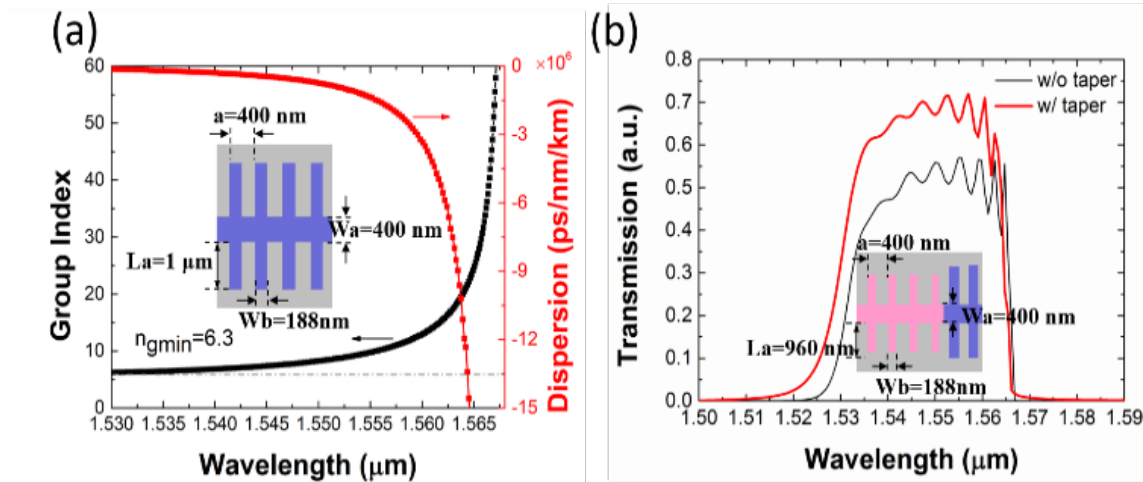


Figure 4.2: (a) Group index and dispersion of band 2 when $a=400$ nm, $W_b=188$ nm, $L_a=1000$ nm, and $W_a=400$ nm. Black: Group index. Red: Dispersion, (b) simulated transmission curve Black: without step taper. Red: with step taper.

4.3 DEVICE FABRICATION AND CHARACTERIZATION

4.3.1 FS 1D PCW fabrication and characterization

The device fabrication started with SOI wafer with a 250 nm silicon device layer (SOITEC). The silicon device layer was thinned down to 230 nm through multiple cycles of thermal oxidation and wet etching. Silicon dioxide hard mask was formed by further oxidizing 10nm silicon, leaving 220 nm silicon device layer. The waveguides were patterned with Jeol 6000 FSE e-beam lithography and reactive ion etching (RIE). The scanning electron microscope (SEM) images of the fabricated FS 1D PCW is shown in Figure 4.3(a). Subwavelength grating couplers are utilized to couple light in and out of the on-chip circuit, the SEM image of which is shown in Figure 4.3(b) [46, 63].

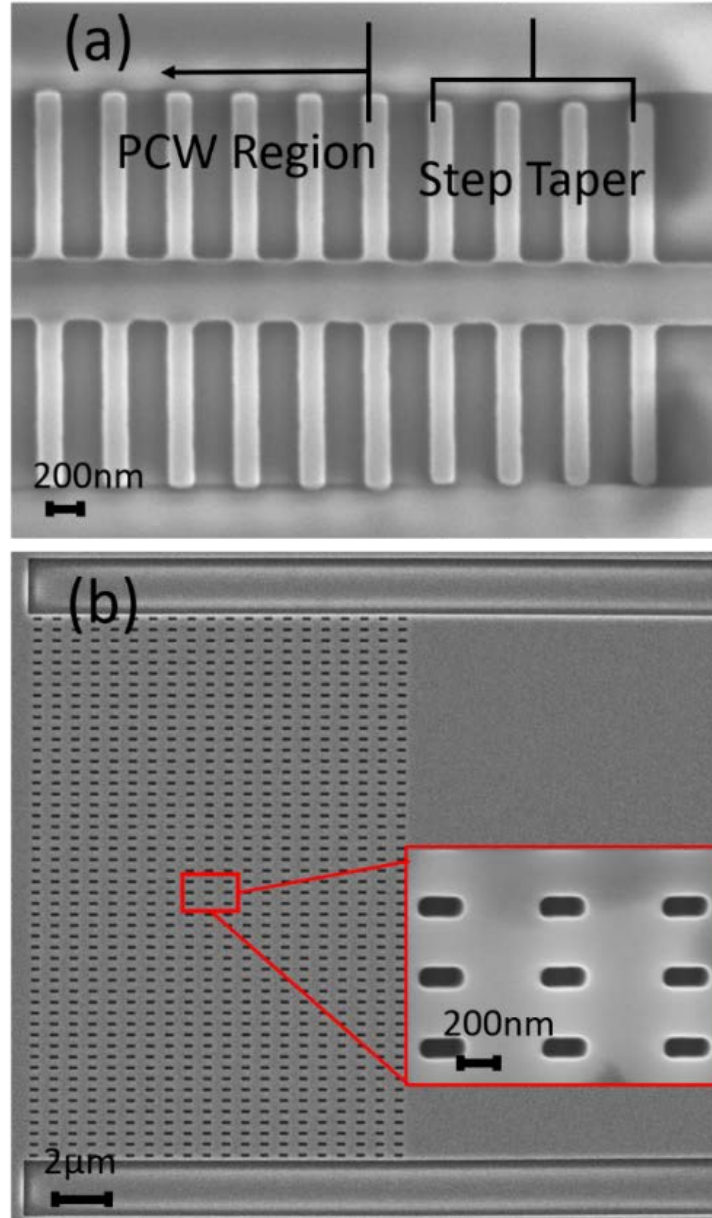


Figure 4.3: (a) SEM image of FS 1D PCW with step taper, (b) subwavelength grating coupler.

The transmission spectrum of testing 500 μm long FS 1D PCW with tapers is shown in Figure 4.4(a). It was obtained using a TE polarized broadband amplified spontaneous emission (ASE) source covering 1530–1610 nm and an optical spectrum

analyzer (OSA). The transmission spectrum shows the lowest loss of 3.729 dB at 1565.14 nm. Group index of the FS 1D PCW was derived using the interference pattern on the spectrum of an unbalanced testing Mach-Zehnder interferometer (MZI) fabricated on the same chip with one arm of 500 μm long FS 1D PCW and the other arm of 500 μm long and 500 nm wide silicon single mode strip waveguide as the same method reported previously [73]. As shown in Figure 4.4(b), the highest group index observed is 31.6, and the lowest is 6.55. Although there is a ~ 25 nm red shift of the transmission spectrum and slow light wavelength region compared to simulation results due to the fabrication error, the trend closely matches the simulation.

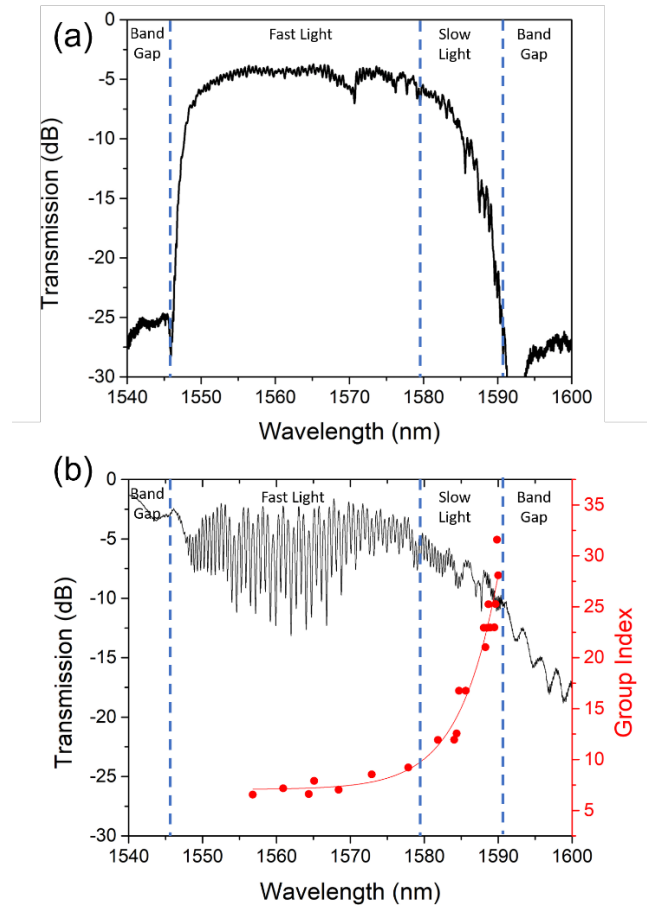


Figure 4.4: continued next page.

Figure 4.4: (a) Transmission spectrum testing 500 μm long FS 1D PCW, (b) measured MZI transmission spectrum and derived group index of a 500 μm long FS 1D PCW.

4.3.2 Delay lines propagation loss and delay measurement

To measure the propagation loss and time delay of the proposed FS 1D PCW, four TTD lines are fabricated. As shown in Figure 4.5(a), the device is with grating couplers for efficient coupling and using two cascaded 1X2 Y-junction splitters to fan out into four waveguides with different FS 1D PCW length. From top to bottom, the waveguides channel-1 to channel-4 contain 3 mm, 2 mm, 1 mm, and 0 mm silicon single mode strip waveguide and 0 mm, 1 mm, 2 mm, 3 mm FS 1D PCW respectively. The transmission spectra of channel-2, 3, and 4 are measured and normalized to channel-1 (strip waveguide), and the propagation loss of the FS 1D PCWs is measured using cut-back method with the same four-channel TTD module. The photonic band edge shifts from the testing waveguides of 1591.6 nm to 1579.55nm, due to the fabrication error and wafer thickness variations. By comparing the transmission spectra of the four channels with different FS 1D PCW length and fitting the length dependence, the propagation loss of FS 1D PCW versus wavelength plot can be achieved as shown in Figure 4.5(b). The lowest propagation loss is 0.79 dB/mm at 1563.87 nm, and the propagation loss at the edge of bandgap at 1579 nm is 2.84 dB/mm.

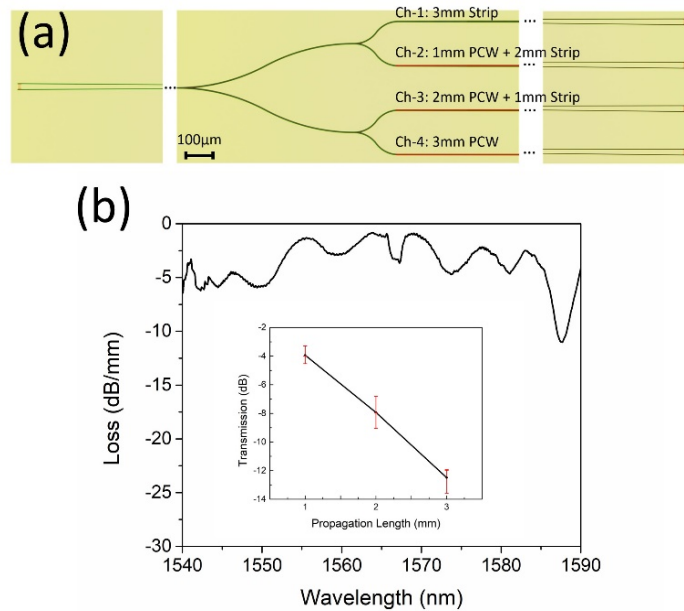


Figure 4.5: (a) Optical microscope images of the four-channel device, (b) FS 1D PCW loss spectrum derived from the cut-back method from waveguides with different FS 1D PCW length. Inset is the measured transmission versus propagation length plot.

For time delay measurements, the channel-1 (with 3 mm silicon strip waveguide) was chosen as a reference waveguide which is first normalized to have a zero-time delay. And time delay was generated for the channel-2 to channel-1 to 4 with respect to that reference waveguide under a certain wavelength. After the measurement, the delay of the 3 mm strip waveguide was calculated and added to the bottom three waveguide respectively to understand the real-time delay of each waveguide.

The delay time measurement schematic is shown in Figure 4.6(a). A 10 dBm 10-12 GHz RF signal was provided from the port 1 of the HP 8510C vector network analyzer (VNA) and was fed into CODEON Mach-40 lithium niobate electro-optic (EO) modulator. A tunable laser provides continuous wave light as a modulated signal carrier. The modulated light was then coupled into the four-channel module using same grating

coupler setup for measuring the transmission spectrum. JDS Uniphase L-band erbium-doped fiber amplifier (EDFA) was added to increase the signal to noise ratio before the New Focus 1014 high-speed photodiode (PD). The optical signal was converted back to RF electrical signal, amplified, and then fed back to VNA port 2. The delay time of the TTD module was determined from the phase of S21 parameters versus frequency data using VNA. The time delay of the top 3 mm silicon strip waveguide was firstly subtracted from the 1 mm, 2 mm, and 3 mm long FS 1D PCW and later added back so that the actual time delay of the bottom three waveguides can be obtained.

Due to the coverage of the L-band EDFA, the four channel TTD module was tested from 1567 nm to 1579 nm with 3 nm step because 1567 nm is the shortest wavelength that L-band EDFA can cover. The phase-frequency curves are shown in Figure 4.6(b-d). The time delay (τ) caused by slow light PCW is derived from a linear regression fit of the data points using the equation:

$$\tau = \frac{\Delta\phi}{\Delta\omega} \quad (4.1)$$

where $\Delta\phi$ is the phase change over the measured frequency range $\Delta\omega$. It is a confirmation of true time delay without beam squint effect when we swing the RF frequencies. Since the group index increases with wavelength, the time delay rises. The slope of the phase curves is negatively increasing with wavelength. High linearity of phase-frequency relation can be seen in the three channels which shows the beam-squint free property of OTTDL.

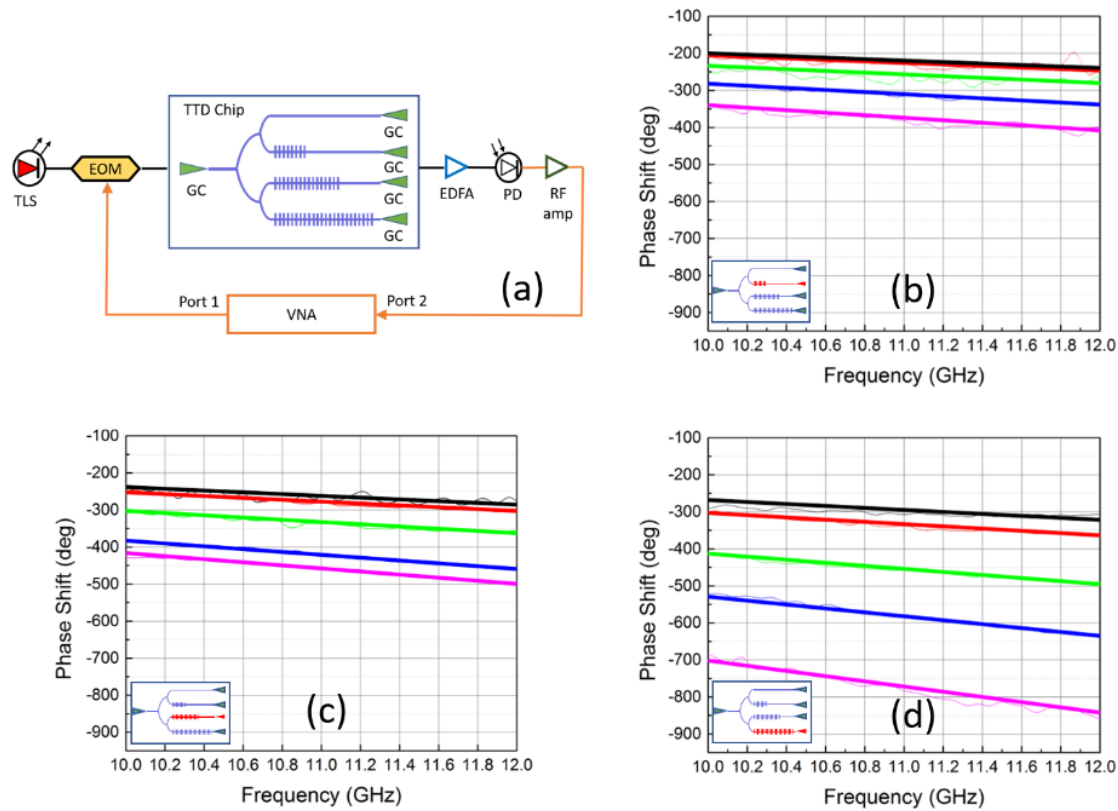


Figure 4.6: (a) Wavelength continuously tunable time delay measurement setup for FS 1D PCW TTD lines. TLS: Tunable laser source; GC: Grating couplers, and Phase-frequency curves for (b) channel-2 (1 mm FS 1D PCW with 2 mm silicon strip waveguide) (c) channel-3 (2 mm FS 1D PCW with 1 mm silicon strip waveguide) (d) channel-4 (3 mm FS 1D PCW). From top to bottom, each color line represents the measurements at $\lambda=1567$ nm (black), 1570 nm (red), 1573 nm (green), 1576 nm (blue), and 1579 nm (magenta) respectively.

From Figure 4.6(b-d), the largest delay occurs at 1579nm. Due to the waveguide defects, the Channel-2 (2 mm FS 1D PCW with 1mm strip waveguide) has a higher loss at 1579 nm the time delay result was not perfectly linear. The time delay for Channel-2 (2mm silicon strip waveguide with 1mm FS 1D PCW), Channel-3(1mm silicon strip waveguide with 2mm FS 1D PCW), and Channel-4(3mm FS 1D PCW) are 94.43 ps,

115.63 ps, 194.9 ps. The maximum time delay we measured for 3 mm FS 1D PCW is 194.9 ps which correspond to the group index of 19.47.

4.4 CONCLUSION

In conclusion, we have proposed, fabricated, and demonstrated an on-chip four-channel optical TTD module based on FS 1D PCWs. The FS 1D PCW shows low loss, strong slow light effect, and high dispersion and therefore is ideal for ultra-compact and low power consumption applications. The on-chip TTD module offers continuous tunability to up to 194.9 ps and the lowest optical propagation loss of 0.79 dB/mm. Further delay can be achieved by increasing the length of FS 1D PCW region.

Chapter 5: Indium Phosphide-Based Polarization Rotator-Splitter and Fully Suspended Holey Photonic Crystal Waveguide for Mid-Infrared Photonic Trace Gas Sensing

In this chapter, the optical losses of waveguides are characterized, and a single-step etched polarization rotator-splitter (PRS) is experimentally demonstrated in low index contrast indium gallium arsenide (InGaAs)-indium phosphide (InP) material system operating at $\lambda=6.15 \mu\text{m}$. The propagation loss of InGaAs-InP waveguide is 4.19 dB/cm for TM mode and 3.25 dB/cm for TE mode. The PRS has a length of 3.04mm and can convert TM input into TE output with 31.2% conversion efficiency. Moreover, a slow light enhanced fully suspended holey photonic crystal waveguide (PCW) is preliminarily demonstrated for ammonia sensing. This study enables the possibility of monolithic integration of quantum cascade lasers (QCL) and quantum cascade detectors (QCD) with slow light enhanced PCW gas sensors.

5.1 INTRODUCTION

Mid-infrared (Mid-IR) absorption spectroscopy based on integrated photonic circuits have shown great promise on trace-gas sensing [18]. It eliminates the needs of bulky gas cells and free-space optical components; therefore, has substantial advantages such as lightweight, alignment-free, and high sensitivity sensing over conventional off-chip methods [15, 19]. In addition, slow light enhanced PCW has been demonstrated for increasing effective light-matter interaction length, and therefore higher detection sensitivity for the targeted gas analyte can be realized [74, 75]. The experimental detection of the chemical warfare simulant triethylphosphate (TEP) has been previously reported down to 10 parts per million (ppm) at $\lambda=3.4 \mu\text{m}$ in a silicon-on-sapphire (SoS) platform using slow light enhanced integrated absorption spectroscopy [75]. For

greenhouse gas carbon monoxide (CO), the detection of 3 ppm at $\lambda=4.55 \mu\text{m}$ with feasibility to detect down to sub-100 parts per billion (ppb) by nominal device modifications also in a SoS platform is demonstrated [76]. While the absorbance of CO peaks around $\lambda=4.55 \mu\text{m}$ where SoS still can be used as a low-loss waveguiding platform ($\sim 2\text{dB/cm}$) [77], SoS is not suitable for sensing TEP at the absorbance maxima of $\lambda=9.5 \mu\text{m}$ due to high intrinsic material loss.

InP as a photonic integration platform has significant potential integrating various passive photonic components such as waveguides [78], switches [79], and modulators [80], with active components such as lasers [81], detectors [82], and electronics [83]. Furthermore, InP based quantum cascade lasers (QCLs) provide narrowband tunable continuous-wave room-temperature emission dramatically affected the field of trace-gas sensing in the entire mid-IR spectral range from 3-11 μm . Therefore, the choice of InP enables the possibility of a monolithically integrated trace gas sensing system which is robust to vibrations and physical stress.

Due to the smaller refractive contrast in the vertical direction of a typical photonic waveguide with an upper air cladding and a lower dielectric cladding, the transverse magnetic (TM) polarized guided mode, with lower effective index, has higher bending loss than the transverse electric (TE) polarized guided mode. Therefore, a TM waveguide requires larger bending radius of curvature than a TE waveguide. It becomes cost inefficient for adopting TM bends especially for III-V integrated circuits where the wafer cost scales with epitaxial growth thickness. Moreover, some photonic components such as slow enhanced PCW with air holes in a dielectric slab material in the most common configuration can only support TE modes while QCLs only emit TM polarized light. In consequence, a polarization rotator-splitter (PRS) is needed so that the polarization state

of the TM polarized optical mode from QCLs can be partially converted for connecting with TE photonic components.

In the following sections, we first characterize the optical losses in fabricated waveguides and bends in low-index contrast InGaAs-InP platform using cut-back method, and then we experimentally demonstrate a single-step etched PRS with the same material platform. The waveguides and PRS design are targeting at the ammonia absorbance peak when $\lambda=6.15 \mu\text{m}$.

5.2 OPTICAL LOSSES IN INGAAS-INP WAVEGUIDES

To characterize the loss of waveguides and bends, a set of 16 propagating waveguides is defined with varying lengths from 25.47 mm to 40.47 mm with 1 mm step were defined. The waveguide width is 12 μm , and waveguides are built on an InP ($n=3.07$) substrate with a 1.15 μm thick core layer of the InGaAs ($n=3.36$), and a thin 0.55 μm upper cladding of InP. The fabrication of the waveguides is done with photolithography, and InP inductively coupled plasma (ICP) etching with plasma-enhanced chemical vapor deposition (PECVD) silicon oxide as etching hard mask. The waveguide layout is illustrated schematically in the inset of Figure 5.1(a), and scanning electron microscope (SEM) images of the fabricated waveguide are shown in Figure 5.1(b). After fabrication, the waveguides are then cleaved at the two edges and characterizing with end-fire coupling setup as shown in Figure 5.4. A half wave plate is inserted in the testing setup for switching the desired testing polarization of the input light.

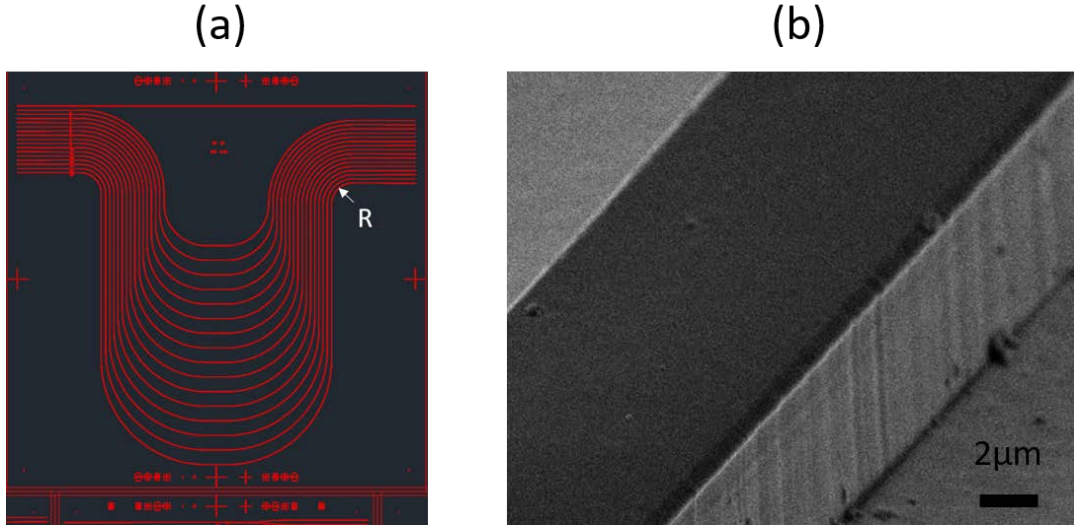


Figure 5.1: (a) The layout of the propagation loss testing waveguides with bending radii of R , (b) tilted SEM image of the fabricated InGaAs-InP waveguide.

By comparing the output transmission output of the waveguides with different lengths and fitting the length dependence, Figure 5.2(a) and Figure 5.2(b) show the loss versus propagation length difference plot for TM and TE polarized light respectively. It can be specially noted that the last three data points colored in red have a significantly higher loss than the rest of the waveguides. Those three data points correspond to the bottom three waveguides which have sharp bends with a radius of 1400, 1200, and 1000 μm (from top to bottom) in Figure 5.1(a) and therefore result in extra bending losses. If a linear fitting for propagation loss excluding those three data points. The propagation loss of the waveguide is 4.19 dB/cm for TM mode and 3.25 dB/cm for TE mode propagation as shown in Figure 5.2(c-d). In addition, the bending loss for curvature with radii of 1000 μm per bend is 8.26 dB for TM and 1.5 dB for TE mode propagation. Therefore, waveguide propagating in TM mode will have higher loss than TE mode in terms of propagation loss and bending loss.

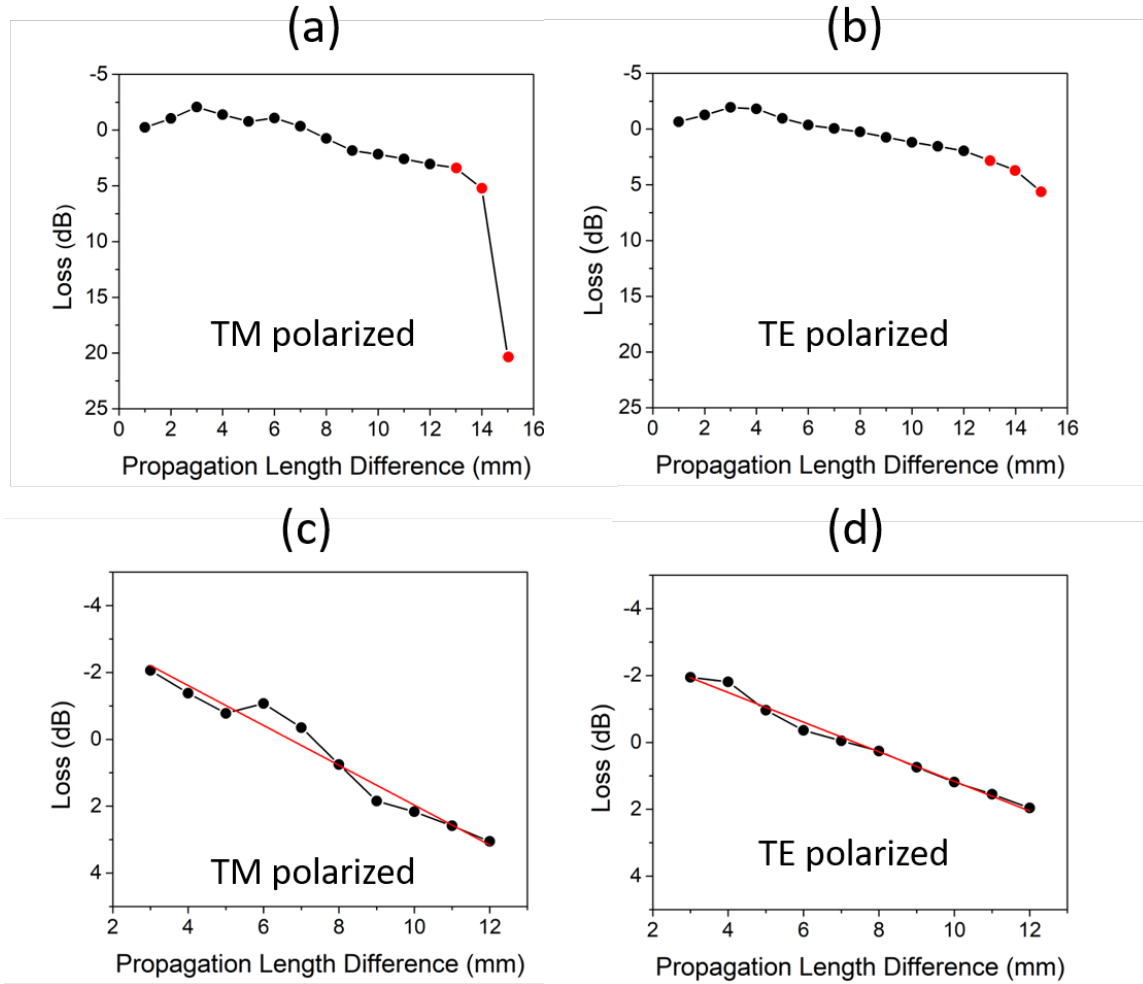


Figure 5.2: Loss versus propagation length difference plot for (a) TM polarized input, and (b) TE polarized input. Loss data exclude waveguides with sharp bends and the linear fitting (shown in red) for TM polarized input, and (b) TE polarized input.

5.3 SINGLE-STEP ETCHED INGAAS-INP PRS DESIGN

A single-step etched PRS working at $6.15 \mu\text{m}$ in InGaAs-InP platform is illustrated in Figure 5.3(a). The PRS operates around the waveguide width where an effective index (N_{eff}) cross point of TM_{00} and TE_{10} occurs as shown in Figure 5.3(b-c). By gradually increasing the waveguide width, the input TM_{00} mode will convert into

TE₁₀ mode. Once converted into TE₁₀, the light is split by a Y-junction splitter into two single mode TE₀₀ waveguides at 180 degrees phase difference. Before connecting with a 2x2 multi-mode interferometer (MMI), an additional 90 degrees phase difference is introduced so that two arms have a total phase difference of -90 degrees at the MMI input ends. As a result, the majority of TE₀₀ will output from arm 1 as the finite difference time domain (FDTD) simulation results show in the in Figure 5.3(d-g). The conversion taper region has three regions and is optimized using eigenmode expansion solver: firstly, the waveguide width changes from 9.8 μm to 10.7 μm over 1 mm, and then to 11.3 μm over 1.2 mm, and finally to 11.75 μm over 0.1 mm. The MMI size is 435 μm in length and 22.7 μm in width. The phase shifter is generated with waveguides of Bezier curves that give the required 90 degrees phase difference between the two arms. 37 % conversion efficiency from TM₀₀ to TE₀₀ can be expected over the total PRS length of 3.04 mm according to simulation results. The smallest waveguide feature size is 4.37 μm which can easily be done with typical photolithography equipment.

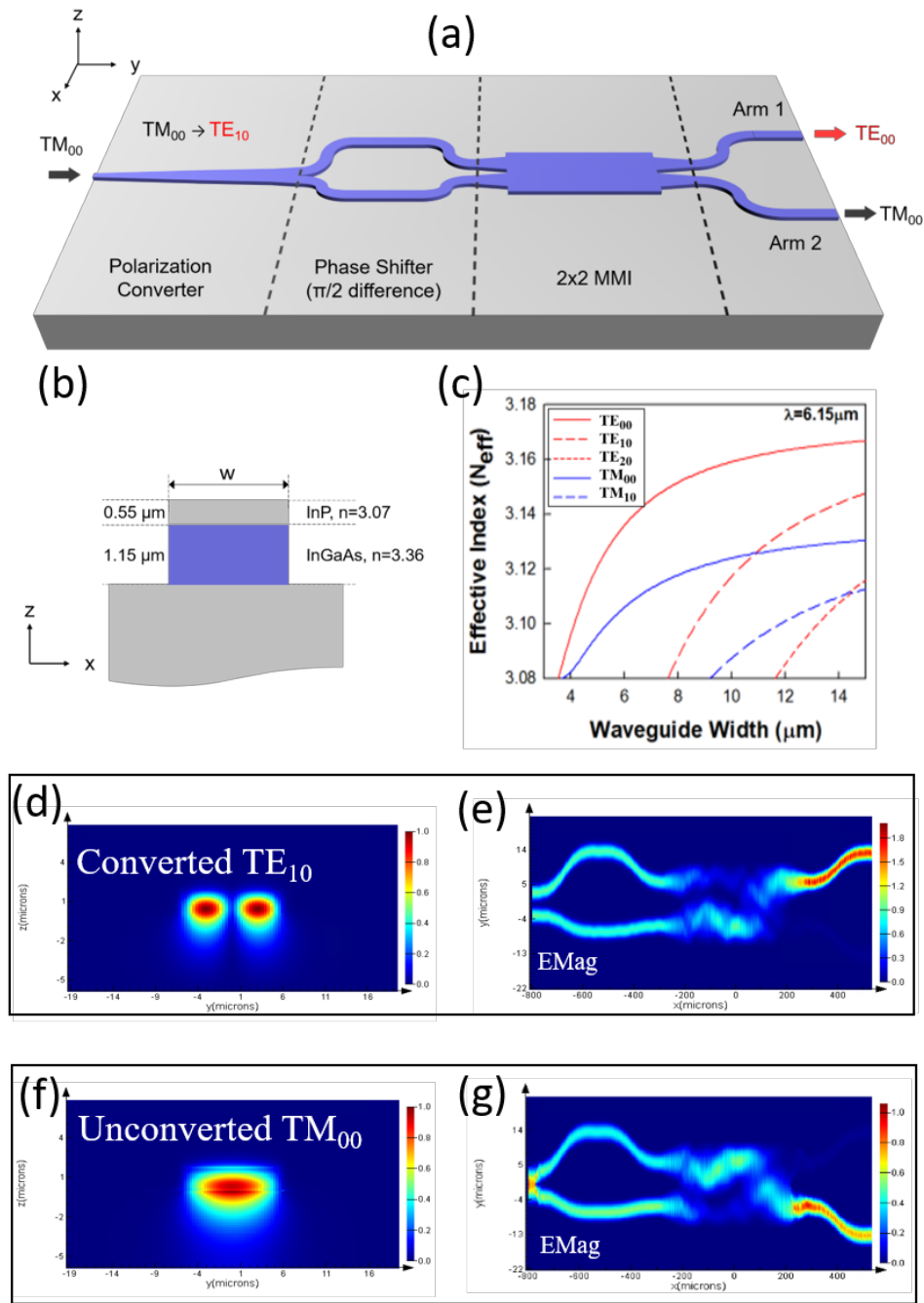
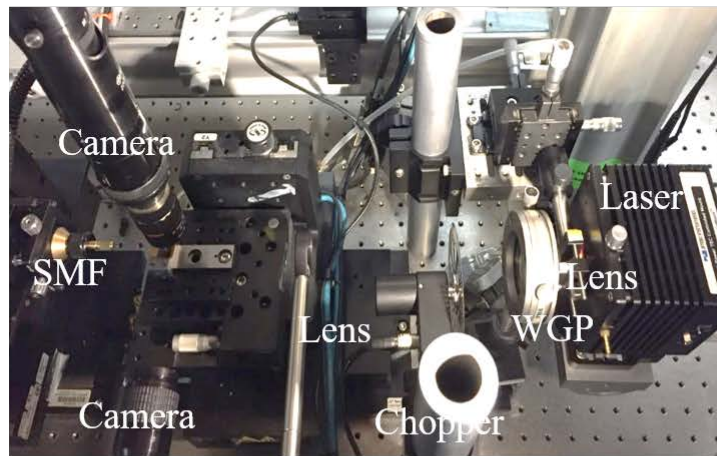
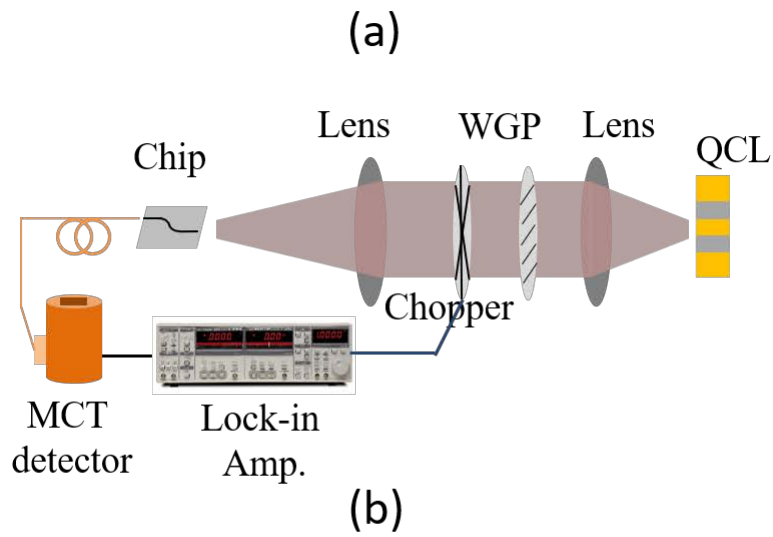


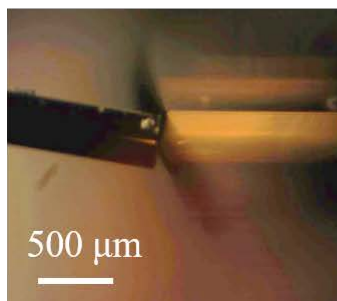
Figure 5.3: (a) Schematic diagram of the single-step etched PRS working at $6.15 \mu\text{m}$ in InGaAs-InP platform, (b) cross-section schematic and the epitaxy layer structures of the PRS, (c) the effective index versus InGaAs-InP waveguide width plot, (d)(e) modal distribution of converted TE_{10} , and (f)(g) modal distribution of unconverted TM_{00} .

5.4 InGaAs-InP PRS FABRICATION AND CHARACTERIZATION

The fabrication of the PRS is also done with photolithography and InP ICP etching. The PRS is cleaved and characterizing with end-fire coupling setup as shown in Figure 5.4. The laser light from 6.15 μm QCL is free-space coupled into the PRS through lens set. A wire grid polarizer (WGP) and an optical chopper are placed between the lens. After routing from PRS chip, light is coupled into a mercury cadmium telluride (MCT) detector via a chalcogenide single mode fiber with a core size of 12 μm . A lock-in amplifier which is synchronized with the optical chopper and connected with the MCT detector for the output optical power reading. The fiber and the PRS chip are placed on motorized 6-axis stages separately to achieve best coupling condition. By measuring the output power from the two arms of the PRS respectively and calculating the converted TE_{00} power percentage, the polarization conversion efficiency can be known.



(c)



(d)

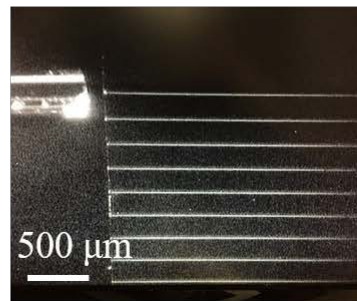


Figure 5.4: (a) Schematic plot for testing setup, (b) real testing setup, and (c)(d) the images indicates the relative position between fiber and the testing photonic chip from side view and top view cameras respectively

In Figure 5.5, it shows the stitched optical microscope image of the fabricated PRS device and the measured results. Four devices with identical geometrical parameters are fabricated and tested. The four PRSs demonstrate an averaged conversion efficiency of 31.2% at the upper arms and the averages loss for the PRS is 4.8 dB.

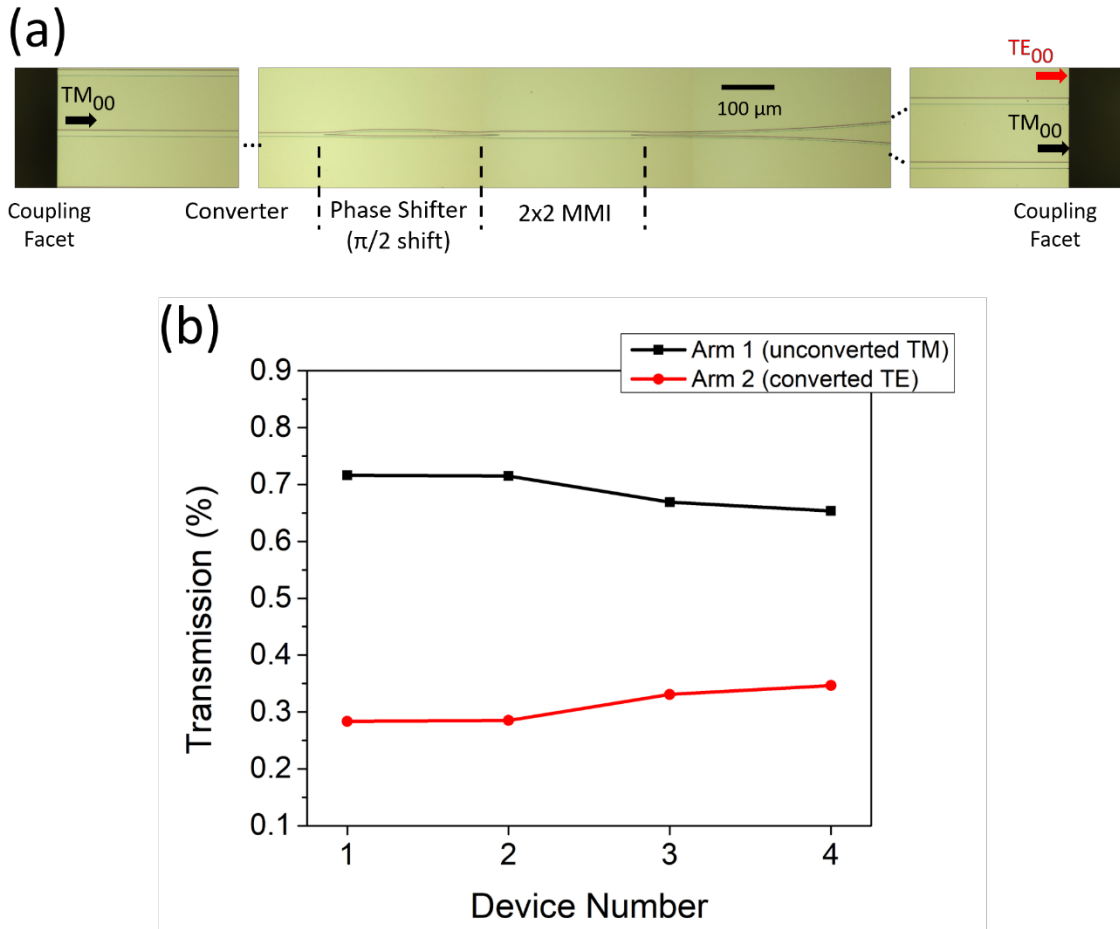


Figure 5.5: (a) Optical microscope images of the fabricated PRS and (b) transmission of the two output arms for four devices with identical parameters.

5.5 FULLY SUSPENDED HOLEY PCW IN INGAAS-INP SYSTEM FOR AMMONIA GAS SENSING

In this section, we demonstrate an absorptive ammonia sensing device based on InGaAs-InP slow light enhanced fully suspended holey PCW operating at $\lambda=6.15 \mu\text{m}$.

The slow light enhanced on-chip absorption spectroscopy principle is based on Beer-Lambert absorption method. According to the Beer-Lambert law [84], transmitted intensity I is given by

$$I = I_0 \exp(-\gamma \alpha L) \quad (5.1)$$

where I_0 is the incident intensity, α is the absorption coefficient of the medium, L is the interaction length, and γ is the medium-specific absorption factor determined by dispersion enhanced light-matter interaction. In conventional systems, L must be large to achieve a desirable sensitivity from the measured I/I_0 . For integrated lab-on-chip systems, L must be small, hence γ must be large. Using perturbation theory, γ can be expressed:

$$\gamma = f \times \frac{c/n}{v_g} \quad (5.2)$$

where c is the velocity of light in free space, v_g is the group velocity in the medium of effective index n , and f is the filling factor denoting the relative fraction of the optical field residing in the analyte medium. Equation 5.2 shows that slow light propagation (small v_g) significantly enhances absorption. Furthermore, greater the electric field overlap (large f) with the analyte, greater the effective absorption by the medium. By combining both effects exist in a holey PCW, a high sensitivity photonic gas sensing device in a compact footprint can be expected [75]. In addition, the fully suspended waveguide design has high refractive index contrast between waveguide core and cladding which makes the guided wave more confined and results in more modal overlap with the gas analyte.

The suspended membrane holey PCW is designed with three-dimensional (3D) plane wave expansion (PWE) method. The holey PCW is designed to be built in the 1.15 μm thick InGaAs core targeting large group index around 6.15 μm operating wavelength, the layers above are removed. In addition, the underneath InP handle layer is etched to create a fully suspended membrane holey PCW. The design schematic is shown

in Figure 5.6(a) with radius $r=0.315a$ and small hole radius $r_h=0.5r$. Figure 5.6(b) shows simulated dispersion characteristics of the propagating holey PCW mode in suspended InGaAs membrane.

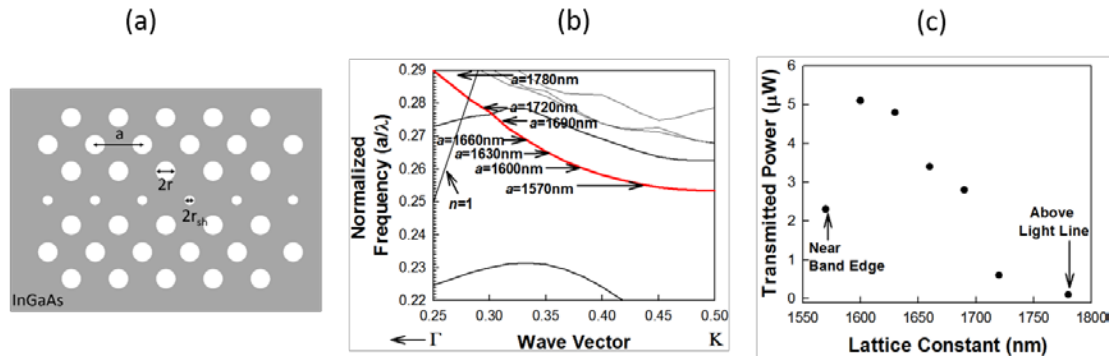


Figure 5.6: (a) Schematic diagram of InGaAs fully suspended holey PCW, (b) simulated photonic band diagram of InGaAs fully suspended holey PCW by 3D PWE. Different devices are made with various lattice constants “a” to probe the guided mode (shown in red) using a single wavelength external source at $\lambda=6.15 \mu\text{m}$ for optical characterization, and (c) measured optical transmission versus different lattice constant.

Since devices are characterized using a single wavelength external source at $\lambda=6.15 \mu\text{m}$, similar as our previously reported measurements [75], several 1mm long devices are made with increasing lattice constants to probe the guided mode dispersion diagram from the forbidden band edge to above the air light line. Optical transmission measurements in Figure 5.6(c) show the variation in transmitted power as a function of lattice constant using same testing setup shown in Figure 5.4(a) and (b) with an additional half-wave plate to rotate the TM polarized light from QCL to TE. Group index of the guided mode reaches a maximum at the band edge and reduces with increasing lattice constant farther from the band edge. Near the light line, the transmitted power drops due to increasing radiation loss. The loss of 1 mm long the fully suspended membrane InGaAs holey PCW

device with lattice constant $a=1600\text{nm}$ which is used for real ammonia sensing testing is 2.32 dB/mm .

The fabrication process flow of the fully suspended membrane InGaAs holey PCW device is shown in Figure 5.7(a) to (d). The holey PCWs are patterned with e-beam lithography and InGaAs-InP ICP etching with 250 nm silicon dioxide etching hard mask grown by PECVD. After residual silicon dioxide is removed, the devices are treated with hydrogen chloride (HCl): deionized (DI) water=3:1 dip which results in a free-standing membrane. Figure 5.8(a) to (d) show SEM images of the fabricated holey PCW structures, including cross-section views showing their suspended cross-sections. We did not observe any sagging effects in 1mm long sections of suspended membranes holey PCWs. Those top and cross-section SEM images indicate the robustness of fully suspended InGaAs structures.

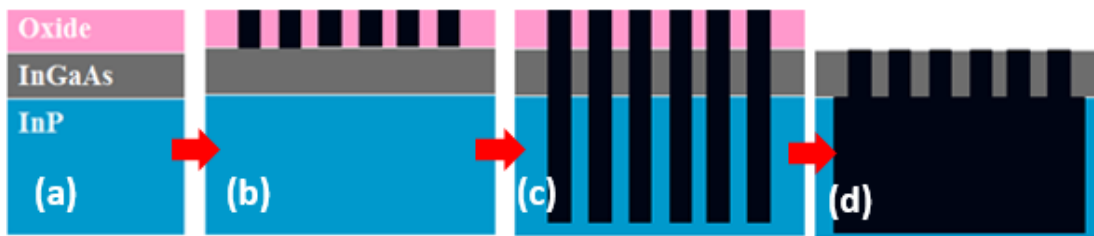


Figure 5.7: Schematic of fabrication steps of InGaAs holey PCW including ICP RIE (a) oxide etching mask growth, (b) transfer of e-beam lithography pattern to oxide mask by RIE, (c) to InGaAs/InP layers, and (d) HCl: DI water= (3:1) dip for a free-standing membrane structure.

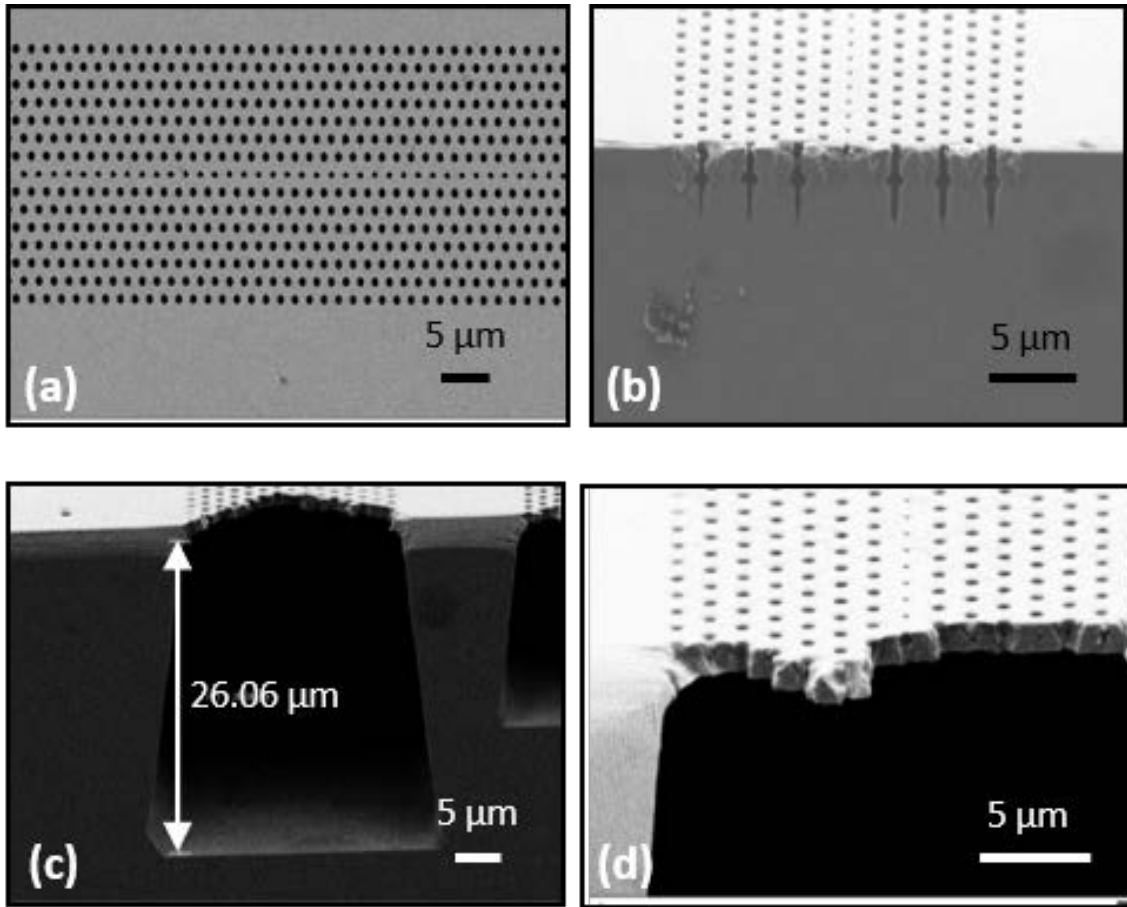


Figure 5.8: (a) Top view and (b) cross-section SEM images of holey PCW in after InGaAs-InP dry etching. Features are etched $\sim 3.1 \mu\text{m}$ deep. Broadening of holes upon reaching InP is not of concern since the InP is wet etched away during undercut sacrificial removal, (c) cross-section SEM image after sacrificial undercut wet etch showing suspended membrane SPCW in InGaAs with $\sim 26 \mu\text{m}$ deep undercut, (d) magnified cross-section showing no sagging or bending even after cleaving.

The real ammonia sensing setup is shown in Figure 5.9(a). The optical transmission of a 1 mm long holey PCW with a lattice constant $a=1600 \text{ nm}$ is measured in the presence and absence of ammonia. A calibrated quantity of ammonia is provided by controlling the gas flow-rate in a commercial Kin-Tek vapor generator with nitrogen as a carrier gas. The ammonia vapor is released from $40 \text{ }^\circ\text{C}$ heated tubing and is delivered

to ~1-2 mm above the surface of the sensing holey PCW area to simulate a real surrounding with ammonia. Figure 5.9(b) shows the transmission drop of the fully suspended holey PCW with the presence of ammonia. The transmission drops to 91.4 % of its original intensity when the ammonia concentration is at 5 ppm. The intensity variation shown on the measurements is less than 2 % when it reaches steady state and can be attributed to the electrical noise of the MCT detector and the vibrations of the optical fiber.

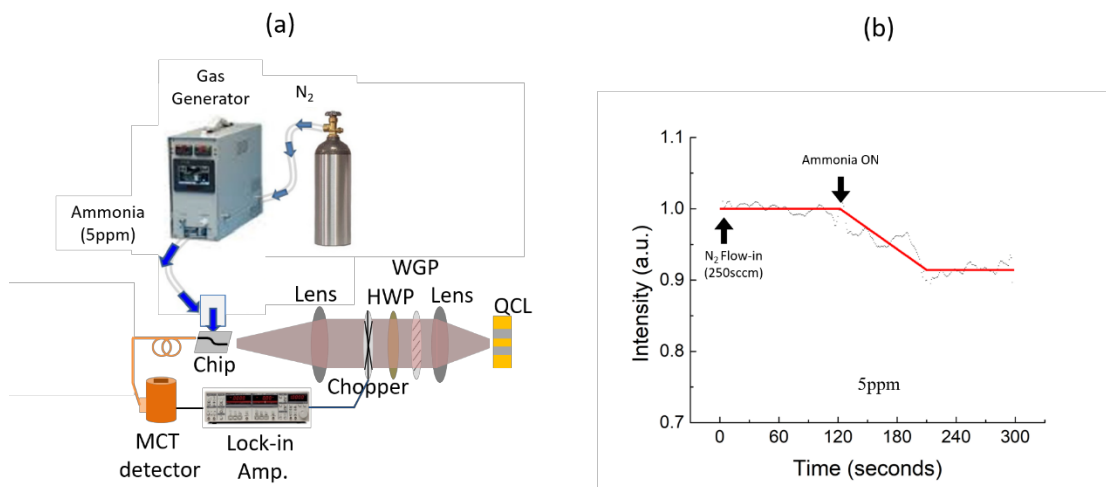


Figure 5.9: (a) Schematic diagram of the ammonia sensing setup, (b) transmitted optical intensity of a 1 mm long holey PCW with $a=1600\text{nm}$ in the presence and absence of 5ppm ammonia.

5.6 CONCLUSION

In this chapter, the InGaAs-InP waveguides operating at $6.15\ \mu\text{m}$ wavelength are firstly fabricated and characterized. The TM waveguides have a higher optical loss, and therefore it necessitates a PRS to convert the incoming TM polarized laser light from QCL. And then we demonstrated a single-step etched PRS design also in InGaAs-InP at $6.15\ \mu\text{m}$ operating wavelength. The measurement results show an averaged 31.2% conversion efficiency is achieved. We also experimentally demonstrate the detection of 5

ppm ammonia gas at $\lambda=6.15 \mu\text{m}$ with an InGaAs fully suspended membrane holey PCW on InP substrate. The results show the feasibility of a compact and highly sensitive photonic trace gas sensor.

Chapter 6: Conclusions and Recommendations for Future Work

6.1 CONCLUSIONS

This dissertation focuses on several intriguing integrated photonic devices, and we demonstrate some promising results for microwave photonics and trace gas sensing applications.

In Chapter 2, an ultra-compact electromagnetic (EM) wave sensor working at 14.1GHz is proposed and demonstrated experimentally. The sensor is based on EO modulation and therefore has several important advantages over conventional electrical radio frequency (RF) sensors including compact size and immunity to electromagnetic interference (EMI). The proposed sensor contains a set of bowtie antenna and a Mach-Zehnder interferometer (MZI) structure with one arm of slow-light enhanced EO polymer infiltrated on one-dimensional (1D) slotted photonic crystal waveguide (SPCW) and the other arm of silicon strip waveguide with the teeth. To minimize the RC delay as well as the electrical connection between the two bowtie antenna poles, the innovative silicon teeth designs are applied for both arms of the MZI respectively so that the device can be operated at 14.1Ghz. The bowtie antenna concentrates electrical field of the impinging wireless EM wave at its designed frequency of 14.1Ghz and applies it onto the EO polymer filled slot for modulating the phase of the guided optical wave. By combining the effect of strong slow light effect of the SPCW, high field enhancement of the bowtie antenna, and large EO coefficient of the EO polymer ($r_{33}=135$ pm/V), the device is only 4.6mm x 4.8mm in size with active region of 300 μm and has minimum detectable electromagnetic power density as low as 4.31 mW/m².

In Chapter 3, a modified photonic microwave sensor based on electro-optic (EO) polymer infiltrated silicon sub-wavelength grating (SWG) waveguide and the bowtie

antenna is designed and experimentally demonstrated. The proposed sensor structure is designed to address several fabrication and EO polymer related issues encountered in chapter 2. The microwave sensor receives wireless microwave signals via the bowtie antenna. The electrical field between the extension bars of the bowtie antenna modulates the light guided in the SWG waveguide-based MZI structure. Thus, microwave signals can be detected by measuring the intensity variation of light from the MZI output. The EO polymer infiltrated SWG does not require ion implantation and has low optical propagation loss. Furthermore, compared to slotted silicon waveguides, the EO polymer poling efficiency on SWG structure can be greatly increased due to wider poling separations and thus the increased breakdown voltage. In order to achieve strong microwave field enhancement, the impedance of the bowtie antennas is tailored. The optimized bowtie antennas operate at 15 GHz and provide >1000X field enhancement while only occupy an area of 7.6 mm X 0.3 mm. Leveraging the folded SWG waveguide, high EO coefficient polymer, and large field enhancement from the bowtie antenna, an ultra-sensitive and compact microwave photonic sensor has been demonstrated.

In Chapter 4, we present the experimental demonstration of a 1D photonic crystal waveguide (PCW) based true time delay line. The 1D PCW is comprised of a silicon strip and periodically arranged teeth along the propagation direction. The 1D PCW is optimized using the plane wave expansion method and 3D finite-difference time-domain (FDTD) method to achieve a large tunable time delay within a reasonable wavelength tuning range. The 1D PCWs are fabricated on silicon-on-insulator (SOI) wafers with 220 nm silicon and 3 μm buried oxide layer through electron beam lithography and reactive ion etching. The measured propagation loss of the 1D PCW is 0.79 dB/mm, which is significantly lower than 2D PCW fabricated under the same condition. A group index of 31.6 is observed experimentally with an unbalanced Mach-Zehnder interferometer

structure. With the frequency sweeping measurement approach, a time delay as large as 194.9 ps has been demonstrated with 3 mm long 1D PCW. Thus, due to its small footprint, low optical loss, and large group index, 1D PCW demonstrates great potential to be a fundamental structure for a vast range of silicon photonic components.

Finally, in Chapter 5, we present a single-step etched polarization rotator-splitter (PRS) in InGaAs-InP material platform for mid-infrared (mid-IR) trace gas sensing application. PRS is an essential photonic component which converts the incoming TM polarized laser light of the quantum cascade lasers (QCL) for connecting TE-polarized-supported slow light enhanced PCW. In addition, PRS helps with high-density integration due to a lower loss in bending and propagation. The measurement results show that the propagation loss of 12 μm wide InGaAs-InP waveguide is 4.19 dB/cm for TM mode and 3.25 dB/cm for TE mode for the operating wavelength of 6.15 μm . The fabricated PRS device has a length of 3.04 mm and can convert TM input into TE output with 31.2% conversion efficiency. We also demonstrated the successful detection of 5 ppm ammonia gas sensing results at $\lambda=6.15$ μm with an InGaAs suspended membrane holey PCW on InP substrate.

6.2 RECOMMENDATIONS FOR FUTURE WORK

For future works, research efforts can be made toward delivering more reliable and robust integrated photonic devices. Current bare photonic chips in SOI and InGaAs-InP wafers which are discussed in previous chapters require stringent fiber alignment for best coupling conditions during all measurements. Therefore, if we can deliver pigtailed, fully packaged photonic devices [85], the device will no longer require further fiber coupling alignments and will be immune to environment-related perturbations such as vibrations and thermal effects which cause larger coupling loss due to misalignment of

fibers and couplers. In addition, a packaged photonic device is important especially for the EO polymer/silicon hybrid structures for EM wave sensing as we proposed in Chapter 2 and 3 since EO polymer is sensitive to heat, UV exposure, and oxygen exposure in the air [86]. In Figure 6.1, a prototype of fiber-pigtailed fully-packaged photonic EM wave sensor is shown. The packaged device contains a non-metallic lid which won't block the sensing wireless microwave signal. Inside the package housing, the chip is also fixed on a non-metallic base and fibers are placed in the horizontal direction. After precise alignment between the fibers and the couplers and best coupling condition achieved, the fibers are then glued and fixed. The material dielectric constant and loss tangent data at 10 GHz operating frequency are shown in Table 6.1. The Teflon lid with a low dielectric constant is used to reduce RF reflection while MACOR is used for sufficient mechanical support as the base housing material. The exploded view of the complete photonic package is shown in Figure 6.2. For photonic devices with grating couplers, angled fibers are required to provide refracted light for maximum input and output coupling efficiency. By Snell's law, to provide 14 degrees coupling angles, the polishing fiber angle θ should be 37.79 degrees as shown in Figure 6.3. There are still issues need to be further studied such as glue selections, the mechanical durability of the couplers after the glue is applied, and device performance characterization after the packaging process.

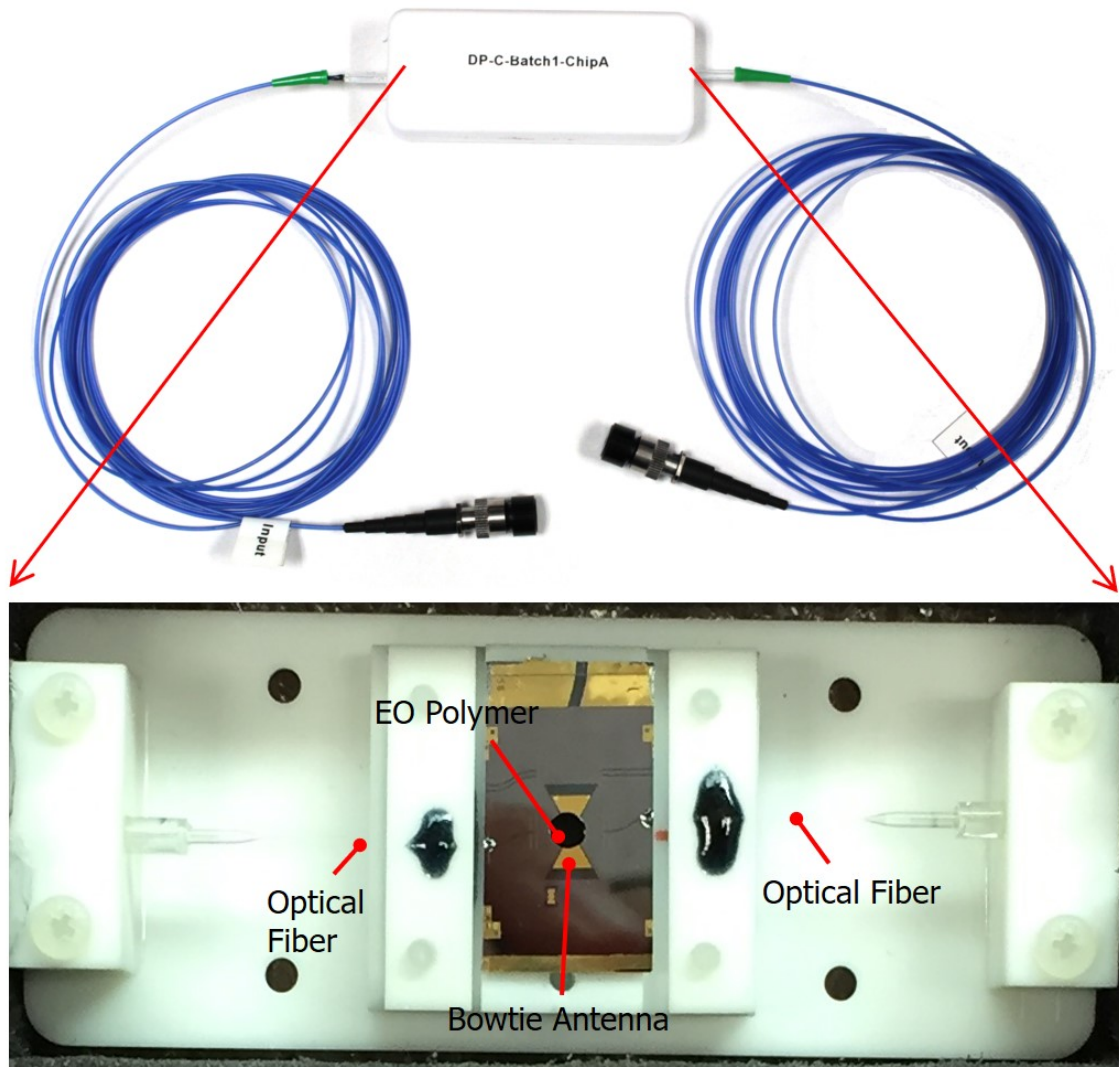


Figure 6.1: Prototype of package EM wave sensor. After best coupling condition achieved on a testing stage, the optical fibers are glued. The relative position between fibers and chip is then fixed.

Material	ϵ_r	δ
MACOR (base)	5.64	0.0025
Teflon (lid)	2.1	0.00028

Table 6.1: The RF properties of the packaging housing materials.

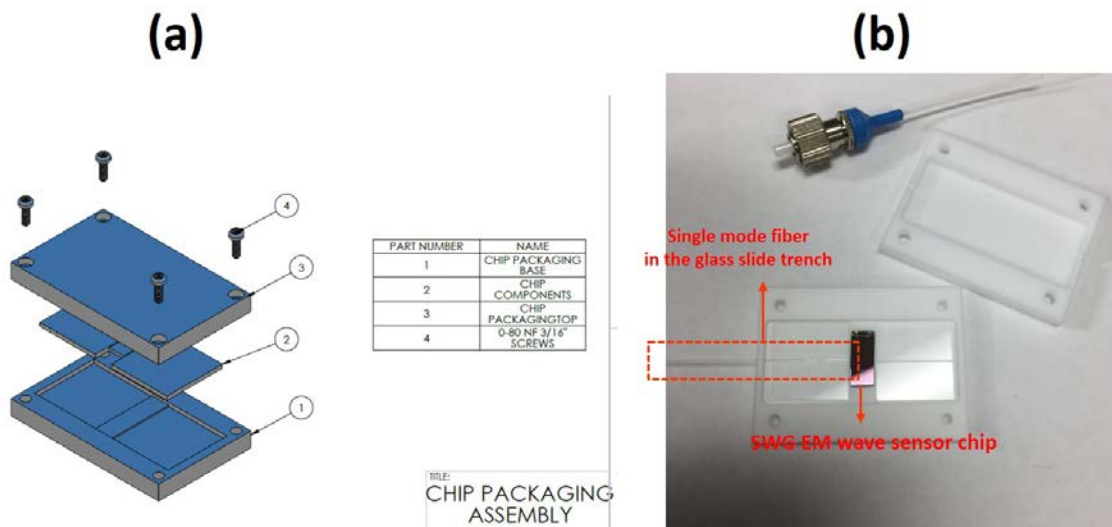


Figure 6.2: (a) The exploded view of the complete package, (b) the machined MACOR base and Teflon lid with real EM wave sensor chip; The polished angled fiber is in the glass slide trench.

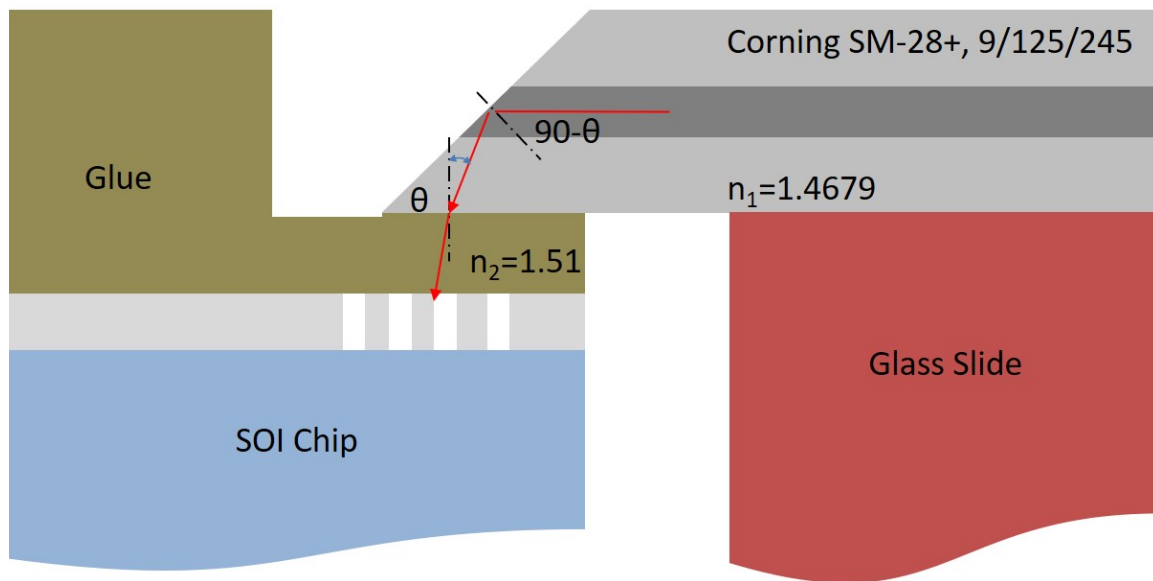


Figure 6.3: Schematic of coupling light with grating couplers and polished angled fiber.

For FS 1D PCW optical true time delay module, the device is now operated based on the wavelength-dependent slow light effect. However, it can also be operated based on thermal-optics (TO) effects. Due to the TO effect of the silicon 1D PCW, under different

temperatures, the delay time of each FS 1D PCW should be different. This provides another type of tunability of the device. Further measurements can be conducted.

For the InGaAs-InP trace gas sensor devices, as discussed in Chapter 5, the goal is to achieve monolithically integrated gas sensor with QCL, QCD, and photonic crystal sensing waveguides on a single chip. Further efforts can be made toward InGaAs-InP photonic device design (both active and passive components) and fabrication process development/optimization for the monolithically integrated devices. In addition, further gas sensing on waveguides can be conducted such as different gas concentration, the different lattice constant, and different waveguide structures.

Appendix

List of Referred Journal Articles:

- [1] **C.-J. Chung**, S. Chakravarty, J. Midkiff, K. Yoo, A. Rostamian, J. Guo, R. T. Chen, "Polarization Rotator-Splitter for Mid-infrared InP-based Photonic Integration Circuits," *Optics letters*, submitted
- [2] F. Mokhtari-Koushyar, E. Heidari, H. Dalir, **C.-J. Chung**, X. Xu, V. J. Sorger, *et al.*, "Wideband Multi-Arm Bowtie Antenna for Millimeter Wave Electro-Optic Sensors and Receivers," *Journal of Lightwave Technology*, pp. 1-1, 2018.
- [3] Z. Ying, S. Dhar, Z. Zhao, C. Feng, R. Mital, **C.-J. Chung**, *et al.*, "Electro-Optic Ripple-Carry Adder in Integrated Silicon Photonics for Optical Computing," *IEEE Journal of Selected Topics in Quantum Electronics*, vol. 24, pp. 1-10, 2018.
- [4] Z. Pan, X. Xu, **C.-J. Chung**, H. Dalir, H. Yan, K. Chen, *et al.*, "High-Speed Modulator Based on Electro-Optic Polymer Infiltrated Subwavelength Grating Waveguide Ring Resonator," *Laser & Photonics Reviews*, vol. 12, p. 1700300, 2018.
- [5] Y. Zou, S. Chakravarty, **C.-J. Chung**, X. Xu, and R. T. Chen, "Mid-infrared silicon photonic waveguides and devices [Invited]," *Photonics Research*, vol. 6, pp. 254-276, 2018.
- [6] **C.-J. Chung**, X. Xu, Z. Pan, F. Mokhtari-Koushyar, R. Wang, H. Yan, *et al.*, "Silicon-Based Hybrid Integrated Photonic Chip for Ku band Electromagnetic Wave Sensing," *Journal of Lightwave Technology*, vol. 36, pp. 1568-1575, 2018

- [7] **C.-J. Chung**, X. Xu, G. Wang, Z. Pan, and R. T. Chen, "On-chip optical true time delay lines featuring one-dimensional fishbone photonic crystal waveguide," *Applied Physics Letters*, vol. 112, p. 071104, 2018.
- [8] H. Yan*, X. Xu*, **C.-J. Chung***, H. Subbaraman, Z. Pan, S. Chakravarty, and R. T. Chen, "One-dimensional photonic crystal slot waveguide for silicon-organic hybrid electro-optic modulators," *Opt. Lett.*, vol. 41, no. 23, pp. 5466-5469, 2016, ***equal contribution first author**
- [9] C. Zhang, H. Subbaraman, Q. Li, Z. Pan, J. G. Ok, T. Ling, **C.-J. Chung**, X. Zhang, X. Lin, R. T. Chen, and L. J. Guo, "Printed photonic elements: Nanoimprinting and beyond," *Journal of Materials Chemistry C*, vol. 4, no.23, pp. 5133-5153, 2016.
- [10] X. Zhang, **C.-J. Chung**, Amir Hosseini, Harish Subbaraman, Jingdong Luo, Alex K Y Jen, Robert L Nelson, Charles Y C Lee, and Ray Chen, "High performance optical modulator based on electro-optic polymer filled silicon slot photonic crystal waveguide," *Journal of Lightwave Technology*, vol. 34, pp. 2941-2951, 2016.
- [11] X. Zhang, **C.-J. Chung**, S. Wang, H. Subbaraman, Z. Pan, Q. Zhan, and R. T. Chen, "Integrated Broadband Bowtie Antenna on Transparent Silica Substrate," *IEEE Antennas and Wireless Propagation Letters*, vol.15, pp. 1377-1381, 2016.
- [12] X. Zhang, S. Chakravarty, **C.-J. Chung**, Z. Pan, H. Yan and R. T. Chen, "Ultra-compact and wide-spectrum-range thermo-optic switch based on silicon coupled photonic crystal microcavities," *Appl. Phys. Lett*, vol. 107, p. 21104, 2015.

List of Referred Conference Articles:

- [1] Z. Pan, X. Xu, **C.-J. Chung**, H. Dalir, H. Yan, K. Chen, *et al.*, "High-speed silicon-organic hybrid modulator enabled by sub-wavelength grating waveguide ring resonator," in *Conference on Lasers and Electro-Optics*, San Jose, California, 2018, p. SM1I.2
- [2] S. Chakravarty, J. Midkiff, **C.-J. Chung**, A. Rostamian, J. Guo, and R. Chen, "Polarization Rotator in Low Index Contrast Substrates for Mid-Infrared Photonic Integration," in *Conference on Lasers and Electro-Optics*, San Jose, California, 2018, p. JW2A.40
- [3] A. Rostamian, J. Guo, S. Chakravarty, **C.-J. Chung**, D. Nguyen, and R. T. Chen, "Parts-Per-Billion Carbon Monoxide Sensing in Silicon-on-Sapphire Mid-Infrared Photonic Crystal Waveguides," in *Conference on Lasers and Electro-Optics*, San Jose, California, 2018, p. ATh1O.4
- [4] **C.-J. Chung**, X. Xu, G. Wang, Z. Pan, and R. T. Chen, "Ultra-Compact Optical True Time Delay Lines Featuring Fishbone-Like One-Dimensional Photonic Crystal Waveguide," in *Conference on Lasers and Electro-Optics*, San Jose, California, 2018, p. JTh4D.4
- [5] J. Guo, A. Rostamian, S. Chakravarty, H. Yan, **C.-J. Chung**, E. Heidari, *et al.*, "Mid-Infrared Silicon-on-Sapphire Polarization Rotator," in *Conference on Lasers and Electro-Optics*, San Jose, California, 2018, p. SF3J.6.
- [6] Z. Pan, X. Xu, **C.-J. Chung**, H. Dalir, H. Yan, K. Chen, *et al.*, "High Speed Modulator Based on Electro-optic Polymer Infiltrated Subwavelength Grating

Waveguide Ring Resonator," in *Optical Fiber Communication Conference*, San Diego, California, 2018, p. M2I.2.

- [7] **C.-J. Chung**, X. Xu, F. Mokhtari-Koushyar, and R. T. Chen, "On-chip microwave photonic sensor featuring silicon-polymer hybrid subwavelength grating waveguide and bowtie antenna", to appear in *Photonics West*, (SPIE, 2018)
- [8] Z. Pan, X. Xu, **C.-J. Chung**, H. Dalir, H. Yan, K. Chen, Y. Wang, B. Jia, Ray T. Chen, "High-speed modulator based on electro-optic polymer infiltrated subwavelength grating waveguide ring resonator", in *Photonics West*, (SPIE, 2018)
- [9] **C.-J. Chung**, X. Xu, Z. Pan, R. Wang, H. Subbaraman, and Ray T. Chen, "Ultra-compact electromagnetic wave sensor featuring electro-optics polymer infiltrated one-dimensional photonic-crystal-slotted waveguide." in *Photonics West*, (SPIE, 2017),
- [10] H. Yan, X. Xu, **C.-J. Chung**, H. Subbaraman, Z. Pan, S. Chakravarty, *et al.*, "One-dimensional photonic crystal slot waveguide for silicon-organic hybrid electro-optic modulators," in *Photonics West*, (SPIE, 2017)
- [11] **C.-J. Chung**, H. Subbaraman, J. Luo, A. K. Y. Jen, R. L. Nelson, C. Y. C. Lee, R. T. Chen, "Fully packaged high-performance RF sensor featuring slotted photonic crystal waveguides in silicon-on-sapphire, " in *Photonics West*, (SPIE, 2016), vol.9747.
- [12] Y. Zou, S. Chakravarty, **C.-J. Chung**, and R. T. Chen, "Miniature mid-infrared thermo-optic switch with photonic crystal waveguide-based silicon-on-sapphire Mach-Zehnder interferometers, " in *Photonics West*, (SPIE, 2016)
- [13] X. Zhang, **C.-J. Chung**, H. Subbaraman, Z. Pan, C.-T. Chen, R. T. Chen, "Design of a plasmonic-organic hybrid slot waveguide integrated with a bowtie-antenna for

- terahertz wave detection," in *SPIE Photonics West 2016*, Photonic and Phononic Properties of Engineered Nanostructures VI, Francisco, CA, Paper No. 9756-39 2016.
- [14] X. Zhang, S. Chakravarty, **C.-J. Chung**, Z. Pan, R. T. Chen, "Microheater-integrated silicon coupled photonic crystal microcavities for low-power thermo-optic switching over a wide spectrum," in *SPIE Photonics West 2016*, Silicon Photonics XI, San Francisco, CA, Paper No. 9752-40 2016.
- [15] Z. Pan, C. Zhang, H. Subbaraman, **C.-J. Chung**, Q. Li, A. Panday, X. Xu, X. Zhang, Y. Zou, L. J. Guo, R. T. Chen, "RF beam transmission/reception of X-band PAA system utilizing large-area, light-weight, and conformal polymer based true-time-delay module developed using imprinting and inkjet printing," in *Terahertz, RF, Millimeter, and Submillimeter-Wave Technology and Applications IX (Photonics West)*, San Francisco, CA, 2016.
- [16] X. Zhang, H. Subbaraman, Z. Pan, **C.-J. Chung**, A. Hosseini, and R. T. Chen, "Low-loss Mode Converter for Silicon-Polymer Hybrid Slot Photonic Crystal Waveguide," in *CLEO: 2015*, OSA Technical Digest (online) (Optical Society of America, 2015), paper SF2H.6.
- [17] X. Zhang, S. Chakravarty, **C.-J. Chung**, Z. Pan, and R. T. Chen, "Wide-spectrum-range Power-efficient Compact Thermo-optic Switch Based on Coupled Photonic Crystal Microcavities," in *CLEO: 2015*, OSA Technical Digest (online) (Optical Society of America, 2015), paper JTh2A.45.
- [18] X. Zhang, A. Hosseini, H. Subbaraman, J. Luo, A. K. Jen, **C.-J. Chung**, R. Nelson, and R. T. Chen, "High-speed Energy-efficient Silicon-polymer Hybrid Integrated

Slot Photonic Crystal Waveguide Modulator," in *CLEO: 2015*, OSA Technical Digest (online) (Optical Society of America, 2015), paper SW3N.1.

- [19] X. Zhang, S. Chakravarty, **C.-J. Chung**, Z. Pan, H. Yan, and R. T. Chen, "Coupled Photonic Crystal Microcavities for Optical Switching over Wide Spectral Range," *IEEE Optical Interconnects Conference*, WC6 (2015)
- [20] X. Zhang, A. Hosseini, H. Subbaraman, J. Luo, A. Jen, **C.-J. Chung**, H. Yan, Z. Pan, R. Nelson, and R. T. Chen, "Backside-gate-assisted Broadband Modulation on Silicon-polymer Hybrid Photonic Crystal Waveguide," *IEEE Optical Interconnects Conference*, WC7 (2015)
- [21] X. Zhang, A. Hosseini, H. Subbaraman, S. Wang, Q. Zhan, J. Luo, A. Jen, **C.-J. Chung**, H. Yan, Z. Pan, R. Nelson, C. Lee, Ray T. Chen, "Antenna-coupled silicon-organic hybrid integrated photonic crystal modulator for broadband electromagnetic wave detection", *Proc. SPIE 9362*, Terahertz, RF, Millimeter, and Submillimeter-Wave Technology and Applications VIII, 93620O (March 14, 2015) (Best Student Paper Award).
- [22] X. Zhang, S. Wang, H. Subbaraman, Q. Zhan, Z. Pan, **C.-J. Chung**, H. Yan, R. T. Chen, "Integrated broadband bowtie antenna on transparent substrate," *Proc. SPIE. 9362*, Terahertz, RF, Millimeter, and Submillimeter-Wave Technology and Applications VIII, 93620P. (March 14, 2015).
- [23] X. Zhang, H. Subbaraman, A. Hosseini, Z. Pan, H. Yan, **C. Chung**, R. T. Chen, "Low-loss mode converter for coupling light into slotted photonic crystal waveguide," *Proc. SPIE. 9368*, Optical Interconnects XV, 936807. (March 13, 2015).

[24] X. Zhang, A. Hosseini, H. Subbaraman, J. Luo, A. Jen, **C.-J. Chung**, H. Yan, Z. Pan, R. Nelson, R. T. Chen, “Broadband energy-efficient optical modulation by hybrid integration of silicon nanophotonics and organic electro-optic polymer,” in *Photonics West*, Photonic integration: Optical Interconnects XV, CA 2015, Paper No. 9368-20.

Bibliography

- [1] C. H. Lee, *Microwave photonics*: CRC press, 2013.
- [2] C.-Y. Lin, H. Subbaraman, A. Hosseini, A. X. Wang, L. Zhu, and R. T. Chen, "Silicon nanomembrane based photonic crystal waveguide array for wavelength-tunable true-time-delay lines," *Applied Physics Letters*, vol. 101, p. 051101, 2012.
- [3] M. Y. Chen, H. Subbaraman, and R. T. Chen, "Photonic crystal fiber beamformer for multiple X-band phased-array antenna transmissions," *IEEE photonics Technology letters*, vol. 20, pp. 375-377, 2008.
- [4] A. Loayssa, J. Capmany, M. Sagues, and J. Mora, "Demonstration of incoherent microwave photonic filters with all-optical complex coefficients," *IEEE Photonics Technology Letters*, vol. 18, pp. 1744-1746, 2006.
- [5] X. Chen, Y.-S. Chen, Y. Zhao, W. Jiang, and R. T. Chen, "Capacitor-embedded 0.54 pJ/bit silicon-slot photonic crystal waveguide modulator," *Optics letters*, vol. 34, pp. 602-604, 2009.
- [6] C.-Y. Lin, A. X. Wang, B. S. Lee, X. Zhang, and R. T. Chen, "High dynamic range electric field sensor for electromagnetic pulse detection," *Optics Express*, vol. 19, pp. 17372-17377, 2011/08/29 2011.
- [7] B. Jalali and S. Fathpour, "Silicon photonics," *Journal of lightwave technology*, vol. 24, pp. 4600-4615, 2006.
- [8] J. D. Joannopoulos, S. G. Johnson, J. N. Winn, and R. D. Meade, *Photonic crystals: molding the flow of light*: Princeton university press, 2011.

- [9] A. Liu, R. Jones, L. Liao, D. Samara-Rubio, D. Rubin, O. Cohen, *et al.*, "A high-speed silicon optical modulator based on a metal–oxide–semiconductor capacitor," *Nature*, vol. 427, pp. 615-618, 2004.
- [10] Y. A. Vlasov and S. J. McNab, "Losses in single-mode silicon-on-insulator strip waveguides and bends," *Optics express*, vol. 12, pp. 1622-1631, 2004.
- [11] C. T. DeRose, D. C. Trotter, W. A. Zortman, A. L. Starbuck, M. Fisher, M. R. Watts, *et al.*, "Ultra compact 45 GHz CMOS compatible Germanium waveguide photodiode with low dark current," *Optics express*, vol. 19, pp. 24897-24904, 2011.
- [12] D. Kwong, A. Hosseini, J. Covey, Y. Zhang, X. Xu, H. Subbaraman, *et al.*, "On-chip silicon optical phased array for two-dimensional beam steering," *Optics Letters*, vol. 39, pp. 941-944, 2014/02/15 2014.
- [13] W.-C. Lai, S. Chakravarty, Y. Zou, Y. Guo, and R. T. Chen, "Slow light enhanced sensitivity of resonance modes in photonic crystal biosensors," *Applied physics letters*, vol. 102, p. 041111, 2013.
- [14] M. J. Thorpe, K. D. Moll, R. J. Jones, B. Safdi, and J. Ye, "Broadband cavity ringdown spectroscopy for sensitive and rapid molecular detection," *Science*, vol. 311, pp. 1595-1599, 2006.
- [15] M. Lackner, "Tunable diode laser absorption spectroscopy (TDLAS) in the process industries—a review," *Reviews in Chemical Engineering*, vol. 23, pp. 65-147, 2007.

- [16] S. H. Zaidi, G. Stojakovic, A. Gutmann, C. Bozdog, U. Mantz, S. B. Charpenay, *et al.*, "FTIR based nondestructive method for metrology of depths in poly silicon-filled trenches," in *Metrology, Inspection, and Process Control for Microlithography XVII*, 2003, pp. 185-191.
- [17] Y. Ma, G. Yu, J. Zhang, X. Yu, R. Sun, and F. K. Tittel, "Quartz enhanced photoacoustic spectroscopy based trace gas sensors using different quartz tuning forks," *Sensors*, vol. 15, pp. 7596-7604, 2015.
- [18] Y. Zou, S. Chakravarty, C.-J. Chung, X. Xu, and R. T. Chen, "Mid-infrared silicon photonic waveguides and devices [Invited]," *Photonics Research*, vol. 6, pp. 254-276, 2018/04/01 2018.
- [19] A. Gurlo and R. Riedel, "In situ and operando spectroscopy for assessing mechanisms of gas sensing," *Angewandte Chemie International Edition*, vol. 46, pp. 3826-3848, 2007.
- [20] E. D. Palik, *Handbook of Optical Constants of Solids, Five-Volume Set: Handbook of Thermo-Optic Coefficients of Optical Materials with Applications*: Elsevier, 1997.
- [21] O. D. Herrera, K.-J. Kim, R. Voorakaranam, R. Himmelhuber, S. Wang, V. Demir, *et al.*, "Silica/electro-optic polymer optical modulator with integrated antenna for microwave receiving," *Journal of Lightwave Technology*, vol. 32, pp. 3861-3867, 2014.
- [22] Z. Xingyu, A. Hosseini, H. Subbaraman, W. Shiyi, Z. Qiwen, L. Jingdong, *et al.*, "Integrated Photonic Electromagnetic Field Sensor Based on Broadband Bowtie

- Antenna Coupled Silicon Organic Hybrid Modulator," *Lightwave Technology, Journal of*, vol. 32, pp. 3774-3784, 2014.
- [23] Y. Salamin, W. Heni, C. Haffner, Y. Fedoryshyn, C. Hoessbacher, R. Bonjour, *et al.*, "Direct Conversion of Free Space Millimeter Waves to Optical Domain by Plasmonic Modulator Antenna," *Nano Letters*, vol. 15, pp. 8342-8346, 2015/12/09 2015.
- [24] G. Gustafsson, R. Boström, B. Holback, G. Holmgren, A. Lundgren, K. Stasiewicz, *et al.*, "The Electric Field and Wave Experiment for the Cluster Mission," in *The Cluster and Phoenix Missions*, C. P. Escoubet, C. T. Russell, and R. Schmidt, Eds., ed Dordrecht: Springer Netherlands, 1997, pp. 137-156.
- [25] H. Liu, J. Yu, P. Huggard, and B. Alderman, "A Multichannel THz Detector Using Integrated Bow-Tie Antennas," *International Journal of Antennas and Propagation*, vol. 2013, p. 8, 2013.
- [26] V. M. N. Passaro, F. Dell'Olio, and F. De Leonardis, "Electromagnetic field photonic sensors," *Progress in Quantum Electronics*, vol. 30, pp. 45-73, // 2006.
- [27] H. Murata, R. Miyanaka, and Y. Okamura, "Wireless space-division-multiplexed signal discrimination device using electro-optic modulator with antenna-coupled electrodes and polarization-reversed structures," *International Journal of Microwave and Wireless Technologies*, vol. 4, pp. 399-405, 2012.
- [28] A. J. Seeds, H. Shams, M. J. Fice, and C. C. Renaud, "Terahertz photonics for wireless communications," *Journal of Lightwave Technology*, vol. 33, pp. 579-587, 2015.

- [29] V. S. Ilchenko, A. A. Savchenkov, A. B. Matsko, and L. Maleki, "Whispering-gallery-mode electro-optic modulator and photonic microwave receiver," *Journal of the Optical Society of America B*, vol. 20, pp. 333-342, 2003/02/01 2003.
- [30] X. Zhang, C.-J. Chung, A. Hosseini, H. Subbaraman, J. Luo, A. K. Jen, *et al.*, "High performance optical modulator based on electro-optic polymer filled silicon slot photonic crystal waveguide," *Journal of Lightwave Technology*, vol. 34, pp. 2941-2951, 2016.
- [31] S. Koeber, R. Palmer, M. Lauermann, W. Heni, D. L. Elder, D. Korn, *et al.*, "Femtojoule electro-optic modulation using a silicon-organic hybrid device," *Light Sci Appl*, vol. 4, p. e255, 02/27/online 2015.
- [32] J. Tian, S. Yu, W. Yan, and M. Qiu, "Broadband high-efficiency surface-plasmon-polariton coupler with silicon-metal interface," *Applied Physics Letters*, vol. 95, p. 013504, 2009.
- [33] EnamiY, C. T. Derose, MathineD, LoychikC, GreenleeC, R. A. Norwood, *et al.*, "Hybrid polymer//sol-gel waveguide modulators with exceptionally large electro-optic coefficients," *Nat Photon*, vol. 1, pp. 180-185, 03//print 2007.
- [34] X. Zhang, A. Hosseini, S. Chakravarty, J. Luo, A. K. Y. Jen, and R. T. Chen, "Wide optical spectrum range, subvolt, compact modulator based on an electro-optic polymer refilled silicon slot photonic crystal waveguide," *Optics Letters*, vol. 38, pp. 4931-4934, 2013/11/15 2013.
- [35] C.-Y. Lin, A. X. Wang, W.-C. Lai, J. L. Covey, S. Chakravarty, and R. T. Chen, "Coupling loss minimization of slow light slotted photonic crystal waveguides

- using mode matching with continuous group index perturbation," *Optics Letters*, vol. 37, pp. 232-234, 2012/01/15 2012.
- [36] A. D. Falco, M. Massari, M. G. Scullion, S. A. Schulz, F. Romanato, and T. F. Krauss, "Propagation Losses of Slotted Photonic Crystal Waveguides," *IEEE Photonics Journal*, vol. 4, pp. 1536-1541, 2012.
- [37] S.-i. Inoue and A. Otomo, "Electro-optic polymer/silicon hybrid slow light modulator based on one-dimensional photonic crystal waveguides," *Applied Physics Letters*, vol. 103, p. 171101, 2013.
- [38] H. Yan, X. Xu, C.-J. Chung, H. Subbaraman, Z. Pan, S. Chakravarty, *et al.*, "One-dimensional photonic crystal slot waveguide for silicon-organic hybrid electro-optic modulators," *Optics Letters*, vol. 41, pp. 5466-5469, 2016/12/01 2016.
- [39] A. D. Panagopoulos, P.-D. M. Arapoglou, and P. G. Cottis, "Satellite communications at Ku, Ka, and V bands: Propagation impairments and mitigation techniques," *IEEE Communications Surveys & Tutorials*, vol. 6, 2004.
- [40] C.-J. Chung, H. Subbaraman, X. Zhang, H. Yan, J. Luo, A. K. Y. Jen, *et al.*, "Towards a fully packaged high-performance RF sensor featuring slotted photonic crystal waveguides," 2016, pp. 97471V-97471V-12.
- [41] X. Zhang, C. J. Chung, S. Wang, H. Subbaraman, Z. Pan, Q. Zhan, *et al.*, "Integrated Broadband Bowtie Antenna on Transparent Silica Substrate," *IEEE Antennas and Wireless Propagation Letters*, vol. 15, pp. 1377-1381, 2016.
- [42] S. Wang and Q. Zhan, "Modified bow-tie antenna with strong broadband field enhancement for RF photonic applications," 2013, pp. 88061V-88061V-6.

- [43] J. K. Doylend, P. E. Jessop, and A. P. Knights, "Optical attenuation in ion-implanted silicon waveguide racetrack resonators," *Optics Express*, vol. 19, pp. 14913-14918, 2011/08/01 2011.
- [44] D. Gao and Z. Zhou, "Nonlinear equation method for band structure calculations of photonic crystal slabs," *Applied Physics Letters*, vol. 88, p. 163105, 2006.
- [45] W. Perrins, D. McKenzie, and R. McPhedran, "Transport properties of regular arrays of cylinders," in *Proceedings of the Royal Society of London A: Mathematical, Physical and Engineering Sciences*, 1979, pp. 207-225.
- [46] X. Xu, H. Subbaraman, J. Covey, D. Kwong, A. Hosseini, and R. T. Chen, "Complementary metal–oxide–semiconductor compatible high efficiency subwavelength grating couplers for silicon integrated photonics," *Applied Physics Letters*, vol. 101, p. 031109, 2012.
- [47] J. Cardenas, C. B. Poitras, K. Luke, L.-W. Luo, P. A. Morton, and M. Lipson, "High coupling efficiency etched facet tapers in silicon waveguides," *IEEE Photonics Technol. Lett*, vol. 26, pp. 2380-2382, 2014.
- [48] T. Shoji, T. Tsuchizawa, T. Watanabe, K. Yamada, and H. Morita, "Low loss mode size converter from 0.3 μm square Si wire waveguides to singlemode fibres," *Electronics Letters*, vol. 38, pp. 1669-1670, 2002.
- [49] X. Zhang, "Silicon-polymer hybrid integrated microwave photonic devices for optical interconnects and electromagnetic wave detection," 2015.
- [50] C. A. Balanis, *Antenna theory: analysis and design*: John Wiley & Sons, 2016.
- [51] D. M. Pozar, *Microwave Engineering*: Wiley, 2012.

- [52] A. Chen and E. Murphy, *Broadband optical modulators: science, technology, and applications*: CRC press, 2011.
- [53] W. B. Bridges, F. T. Sheehy, and J. H. Schaffner, "Antenna-coupled millimeter-wave LiNbO₃ electro-optic modulator," in *Spaceborne Photonics: Aerospace Applications of Lasers and Electro-Optics/Optical Millimeter-Wave Interactions: Measurements, Generation, Transmission and Control. LEOS 1991 Summer Topical Meetings on*, 1991, pp. 16-17.
- [54] S. Koenig, D. Lopez-Diaz, J. Antes, F. Boes, R. Henneberger, A. Leuther, *et al.*, "Wireless sub-THz communication system with high data rate," *nature photonics*, vol. 7, p. 977, 2013.
- [55] N. Kuwabara, K. Tajima, R. Kobayashi, and A. Fujio, "Development and analysis of electric field sensor using LiNbO₃ optical modulator," *Electromagnetic Compatibility, IEEE Transactions on*, vol. 34, pp. 391-396, 1992.
- [56] N. Williams and J. Spain, "Radio frequency monitor for semiconductor process control," ed: Google Patents, 1995.
- [57] P. Mohan, "Method and apparatus for remotely deriving the velocity vector of an in-flight ballistic projectile," ed: Google Patents, 2005.
- [58] W. Heni, C. Haffner, D. L. Elder, A. F. Tillack, Y. Fedoryshyn, R. Cottier, *et al.*, "Nonlinearities of organic electro-optic materials in nanoscale slots and implications for the optimum modulator design," *Optics Express*, vol. 25, pp. 2627-2653, 2017.

- [59] P. J. Bock, P. Cheben, J. H. Schmid, J. Lapointe, A. Delâge, S. Janz, *et al.*, "Subwavelength grating periodic structures in silicon-on-insulator: a new type of microphotonic waveguide," *Optics express*, vol. 18, pp. 20251-20262, 2010.
- [60] J. G. Wangüemert-Pérez, P. Cheben, A. Ortega-Moñux, C. Alonso-Ramos, D. Pérez-Galacho, R. Halir, *et al.*, "Evanescent field waveguide sensing with subwavelength grating structures in silicon-on-insulator," *Optics letters*, vol. 39, pp. 4442-4445, 2014.
- [61] V. Donzella, A. Sherwali, J. Flueckiger, S. M. Grist, S. T. Fard, and L. Chrostowski, "Design and fabrication of SOI micro-ring resonators based on sub-wavelength grating waveguides," *Optics express*, vol. 23, pp. 4791-4803, 2015.
- [62] H. Yan, L. Huang, X. Xu, S. Chakravarty, N. Tang, H. Tian, *et al.*, "Unique surface sensing property and enhanced sensitivity in microring resonator biosensors based on subwavelength grating waveguides," *Optics express*, vol. 24, pp. 29724-29733, 2016.
- [63] X. Xu, H. Subbaraman, J. Covey, D. Kwong, A. Hosseini, and R. T. Chen, "Colorless grating couplers realized by interleaving dispersion engineered subwavelength structures," *Optics letters*, vol. 38, pp. 3588-3591, 2013.
- [64] R. C. Hansen, *Phased array antennas* vol. 213: John Wiley & Sons, 2009.
- [65] L. C. Godara, "Application of antenna arrays to mobile communications. II. Beam-forming and direction-of-arrival considerations," *Proceedings of the IEEE*, vol. 85, pp. 1195-1245, 1997.

- [66] R. DeSalvo, C. Middleton, E. Grafer, A. Cramer, K. Anzalone, E. Soto, *et al.*, "The convergence of microwave photonic and optical wireless systems with military communication and sensor systems," in *2016 IEEE Avionics and Vehicle Fiber-Optics and Photonics Conference (AVFOP)*, 2016, pp. 191-192.
- [67] X. S. Yao and L. Maleki, "A novel 2-D programmable photonic time-delay device for millimeter-wave signal processing applications," *IEEE Photonics Technology Letters*, vol. 6, pp. 1463-1465, 1994.
- [68] H. Subbaraman, M. Y. Chen, and R. T. Chen, "Photonic dual RF beam reception of an X band phased array antenna using a photonic crystal fiber-based true-time-delay beamformer," *Applied optics*, vol. 47, pp. 6448-6452, 2008.
- [69] L. H. Gesell, R. E. Feinleib, J. L. Lafuse, and T. M. Turpin, "Acousto-optic control of time delays for array beam steering," 1994, pp. 194-204.
- [70] A. Melloni, A. Canciamilla, C. Ferrari, F. Morichetti, L. O. Faolain, T. F. Krauss, *et al.*, "Tunable Delay Lines in Silicon Photonics: Coupled Resonators and Photonic Crystals, a Comparison," *IEEE Photonics Journal*, vol. 2, pp. 181-194, 2010.
- [71] X. Wang, B. Howley, M. Y. Chen, and R. T. Chen, "Phase error corrected 4-bit true time delay module using a cascaded 2×2 polymer waveguide switch array," *Applied Optics*, vol. 46, pp. 379-383, 2007/01/20 2007.
- [72] T. Tatoli, D. Conteduca, F. Dell'Olio, C. Ciminelli, and M. N. Armenise, "Graphene-based fine-tunable optical delay line for optical beamforming in phased-array antennas," *Applied Optics*, vol. 55, pp. 4342-4349, 2016/06/01 2016.

- [73] Y. A. Vlasov, M. O'Boyle, H. F. Hamann, and S. J. McNab, "Active control of slow light on a chip with photonic crystal waveguides," *Nature*, vol. 438, pp. 65-69, 11/03/print 2005.
- [74] W.-C. Lai, S. Chakravarty, Y. Zou, and R. T. Chen, "Multiplexed detection of xylene and trichloroethylene in water by photonic crystal absorption spectroscopy," *Optics Letters*, vol. 38, pp. 3799-3802, 2013/10/01 2013.
- [75] Y. Zou, S. Chakravarty, P. Wray, and R. T. Chen, "Mid-infrared holey and slotted photonic crystal waveguides in silicon-on-sapphire for chemical warfare simulant detection," *Sensors and Actuators B: Chemical*, vol. 221, pp. 1094-1103, 2015/12/31/ 2015.
- [76] A. Rostamian, J. Guo, S. Chakravarty, C.-J. Chung, D. Nguyen, and R. T. Chen, "Parts-Per-Billion Carbon Monoxide Sensing in Silicon-on-Sapphire Mid-Infrared Photonic Crystal Waveguides," in *Conference on Lasers and Electro-Optics*, San Jose, California, 2018, p. ATh1O.4.
- [77] F. Li, S. D. Jackson, C. Grillet, E. Magi, D. Hudson, S. J. Madden, *et al.*, "Low propagation loss silicon-on-sapphire waveguides for the mid-infrared," *Optics express*, vol. 19, pp. 15212-15220, 2011.
- [78] X. Letartre, C. Seassal, C. Grillet, P. Rojo-Romeo, P. Viktorovitch, M. Le Vassor d'Yerville, *et al.*, "Group velocity and propagation losses measurement in a single-line photonic-crystal waveguide on InP membranes," *Applied physics letters*, vol. 79, pp. 2312-2314, 2001.

- [79] T. Tanemura, I. M. Soganci, T. Oyama, T. Ohyama, S. Mino, K. A. Williams, *et al.*, "Large-capacity compact optical buffer based on InP integrated phased-array switch and coiled fiber delay lines," *Journal of Lightwave Technology*, vol. 29, pp. 396-402, 2011.
- [80] Y. Ogiso, J. Ozaki, Y. Ueda, N. Kashio, N. Kikuchi, E. Yamada, *et al.*, "Over 67 GHz Bandwidth and 1.5 V $V\pi$ InP-Based Optical IQ Modulator With nipi Heterostructure," *Journal of Lightwave Technology*, vol. 35, pp. 1450-1455, 2017.
- [81] S. Lange, S. Wolf, J. Lutz, L. Altenhain, R. Schmid, R. Kaiser, *et al.*, "100 Gbd Intensity Modulation and Direct Detection With an InP-Based Monolithic DFB Laser Mach-Zehnder Modulator," *Journal of Lightwave Technology*, vol. 36, pp. 97-102, 2018.
- [82] C. Yu, M. Shangguan, H. Xia, J. Zhang, X. Dou, and J.-W. Pan, "Fully integrated free-running InGaAs/InP single-photon detector for accurate lidar applications," *Optics Express*, vol. 25, pp. 14611-14620, 2017.
- [83] M. Urteaga, Z. Griffith, M. Seo, J. Hacker, and M. J. Rodwell, "InP HBT technologies for THz integrated circuits," *Proceedings of the IEEE*, vol. 105, pp. 1051-1067, 2017.
- [84] N. A. Mortensen and S. Xiao, "Slow-light enhancement of Beer-Lambert-Bouguer absorption," *Applied Physics Letters*, vol. 90, p. 141108, 2007.
- [85] C. Kopp, S. Bernabe, B. B. Bakir, J.-M. Fedeli, R. Orobtcouk, F. Schrank, *et al.*, "Silicon photonic circuits: on-CMOS integration, fiber optical coupling, and

- packaging," *IEEE Journal of Selected Topics in Quantum Electronics*, vol. 17, pp. 498-509, 2011.
- [86] D. Jin, H. Chen, A. Barklund, J. Mallari, G. Yu, E. Miller, *et al.*, "EO polymer modulators reliability study," in *Organic Photonic Materials and Devices XII*, 2010, p. 75990H.

Vita

Chi-Jui Chung received his B.S. degree in Mechanical Engineering from National Chiao Tung University, Hsinchu, Taiwan, in 2009 and M.S. degree in Power Mechanical Engineering from National Tsing Hua University, Hsinchu, Taiwan, in 2011. After three years of substitute military service as an engineer at Electronics and Optoelectronics Research Laboratories at Industrial Technology Research Institute, Hsinchu, Taiwan. From 2014, he worked towards his Ph.D. degree in the Nanophotonics and Optical Interconnects Research Lab at the University of Texas at Austin, TX, USA. His research interests include integrated silicon photonic devices for electromagnetic wave sensing, optical true time delay, and indium phosphide photonic devices for trace gas sensing application.

Email: cjchung@utexas.edu

This dissertation was typed by the author.